Fram Strait recirculation and the East Greenland Current: Spatial structure north of 79°N

-Master's Thesis in Marine Geosciences-
Fachbereich Geowissenschaften
Universität Bremen

by

Maren Elisabeth Richter

Bremen, 2017

Supervisors: Prof. Angelika Humbert
Dr. Torsten Bickert
Dr. Wilken-Jon von Appen

Abstract

Fram Strait, located between Greenland and Svalbard, is a gateway for heat and nutrient transport to the Arctic Ocean and sea-ice export from the Arctic. Two of the Greenland ice-sheet's largest outlet glaciers interact with the regional ocean circulation with ramifications for mass loss to the ocean. Relatively warm Atlantic Water (AW) is transported northward in the eastern Fram Strait via the West Spitsbergen Current (WSC); in the western Fram Strait the East Greenland Current (EGC) transports colder, fresher water of Arctic origin southward. Part of the AW entering Fram Strait from the south is not transported to the Arctic Ocean, but instead 'recirculates' in Fram Strait, i.e. it flows westward to join the EGC. Although crucial for understanding AW pathways to large outlet glaciers through two troughs (Westwind Trough and Norske Trough) on the East Greenland shelf, it is not known at what latitudes AW joins the EGC and how that changes the structure of the EGC. Here we present synoptic observations that contribute to answering these questions. Hydrographical and velocity data were collected by *RV Polarstern* in summer 2016. Four sections cross the EGC between 77.8°N and 80.8°N; two are located at the mouths of the troughs, while one also crosses the central Fram Strait and the WSC. A meridional section at 0°EW spans the recirculation in the central Fram Strait. These data allowed the first estimate of absolute geostrophic transports of different watermasses, their propagation and transformation in the recirculation and the EGC north of 79°N at an appropriate spatial resolution. Below Polar Surface Water (PSW), AW and colder Arctic Atlantic Water (AAW) advected from further north are located horizontally next to each other and then intermittently mix as they flow southward in the EGC. No AW was found directly in front of Westwind Trough, it is however found inside the more southern Norske Trough. The northernmost extent of the recirculation in the synoptic sections in Fram Strait is at 80.8°N, however, further investigations are needed to test whether this is representative. The velocity field along 79°N is highly variable with evidence of surface intensified eddies travelling westward. The observations of the EGC south of 79.6°N display a typical boundary current structure with absolute geostrophic transports reaching over 4 Sv. Conversely, at 80.2°N the isopycnals near the shelfbreak are only weakly sloped. Southward transport of AW at 76.6°N reaches 1.5 Sv in the shelfbreak EGC and transport of dense Denmark Strait Overflow Water (DSOW) reaches a maximum of 2.5 Sv. Sections from a high-resolution numerical ocean model of Fram Strait corroborate our findings.

Contents

1   Introduction

Fram Strait recirculation has important connections to a variety of fields. The following places the topic in its wider context in oceanography, climate sciences and glaciology and gives an overview of the current knowledge of Fram Strait recirculation.

1.1   Motivation

1.1.1   Climate and Deep Water Formation

Climate   Ocean circulation strongly influences the Earth's climate. Areas in the oceans in which deep water is formed and areas in which deep water descends to depth are especially important. Here CO_2 (an important greenhouse gas) is removed from contact with the atmosphere for periods of 10s to 1000s of years thus buffering the climate system and slowing the anthropogenic climate change (*Sabine et al.*, 2004). The ocean is also capable of taking up large amounts of heat. Approximately 93 % of the global increase in heat content between 1971 and 2010 took place in the oceans, with the upper 700 m accounting for 2/3 of this (*Rhein et al.*, 2013). The most direct way for this is warming of the upper ocean. Warming in areas of deep water formation and export allows the heat to be stored for 1000s of years in the deep ocean as well. According to the Intergovernmental Panel on Climate Change (IPCC)the upper ocean and likely also the deep ocean have warmed in recent decades (*Rhein et al.*, 2013). This warming is already contributing to global sea-level rise due to thermal expansion (*Rhein et al.*, 2013).

Deep Water Formation   In the northern hemisphere deep water is formed primarily in the central gyres of the Labrador, Irminger, Iceland and Greenland Seas and on the continental shelves in the Arctic Ocean (Figure 1). This is the northern source of dense waters to the vertical component of the Atlantic Meridional Overturning Circulation (AMOC). Since the mid 1990s the interplay between deep and intermediate watermasses in the Greenland Sea has undergone a change. Deep waters imported from the Arctic have warmed during the past two decades (*von Appen et al.*, 2015). At the same time the deep convection in the Greenland Sea and thus the deep water formation there weakened making the Arctic the dominant source of deep water in the Arctic Ocean and Nordic Seas (*Rudels et al.*, 2012). Deep waters formed north of the Greenland-Scotland ridge (i.e. in the Arctic Ocean and Nordic Seas) are too dense to pass over this ridge. Instead intermediate water flows across the ridge, for example as Denmark

Strait Overflow Water (DSOW) across Denmark Strait or Iceland Scotland Overflow Water (ISOW) across the Faroe Bank Channel (see Figure 1). These waters are denser than the ambient water south of the ridge and thus descend the slope thereby forming a major contribution to North Atlantic Deep Water. This means that the water from the overflow which is referred to as intermediate water north of the ridge is referred to as deep water south of the ridge. South of Denmark Strait three of the four components of North Atlantic Deep Water flow together allowing mixing between them as well as entrainment of ambient watermasses (*Dickson and Brown*, 1994; *Dickson et al.*, 2008, see also for more information on the Denmark Strait Overflow). The origin of the DSOW is subject of ongoing debate. *Mauritzen* (1996) suggested a circulation scheme where deep and intermediate watermasses forming the DSOW are not formed in isolated areas but through continuous modification of water from the North Atlantic flowing cyclonically in boundary currents around the Nordic Seas and Arctic Ocean. *Rudels et al.* (2002) and *Våge et al.* (2013) suggest that DSOW is formed not only in the boundary current but also in the Iceland Sea. Further, dense water forms jets from the Greenland shelf down the continental slope south of Denmark Strait forming a further pathway for intermediate water to contribute to the AMOC (*von Appen et al.*, 2014).

1.1.2   Ice-Ocean Interaction

Ice-ocean interactions are connected to deep water formation via changes in water density through increased freshwater input from land and/or sea-ice. There is evidence that deep water formation in the Labrador Sea has declined as freshwater input to the region has increased (*Yang et al.*, 2016). The freshwater may have come from mass loss of the Greenland ice-sheet to the ocean. Ice-ocean interactions also influence the global sea-level. Warm ocean water that comes into contact with glaciers can cause basal and frontal melt. This can alter the dynamics (e.g. accelerate) of these glaciers. Since some glaciers are outflows from large ice-sheets this influences the mass balance of the ice-sheets. This applies to both the Antarctic ice-shelves and glaciers with floating ice-tongues and marine terminating glaciers in Greenland and Antarctica. If ice-sheets lose mass to the ocean, global sea-level rises.

Greenland Ice-Ocean Interaction   The Greenland ice-sheet is Earth's second largest and it alone contains enough water to raise global sea-level by about 7 m (*Rignot and Mouginot*, 2012; *Bamber et al.*, 2013). Most of Greenland's large outlet glaciers are marine terminating (*Moon and Joughin*, 2008; *Rignot and Mouginot*, 2012). A widespread, synchronous retreat and acceleration of Greenland's marine terminating glaciers (*Rignot*
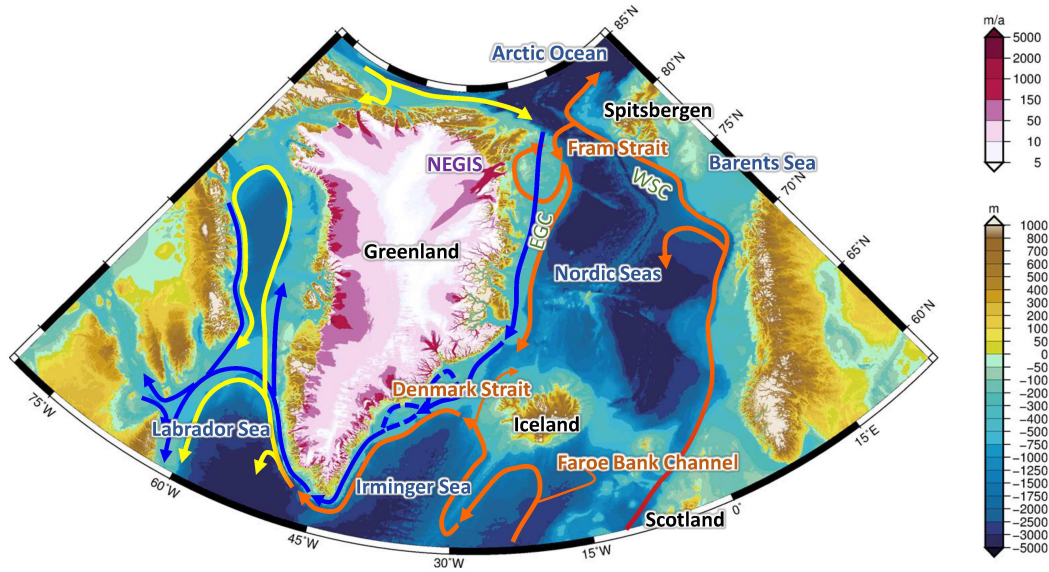
Figure 1: Locations of the Labrador and Irminger Sea, Nordic Seas (the Greenland, Iceland and Norwegian Sea), Arctic Ocean, Denmark Strait, Fram Strait, the Greenland-Scotland-Ridge (Denmark Strait and the Faroe-Bank-Channel are the deep pathways across the ridge), the NEGIS, the West Spitsbergen Current (WSC) and he East Greenland Current (EGC). Bathymetry from (GEBCO), ice velocities from (MEaSURE), map modified from *A. Humbert*, pers.comm., 2017

and Kanagaratnam, 2006; *Howat et al.*, 2007, 2008; *Moon and Joughin*, 2008) coinciding with warmer ocean temperatures (*Holland et al.*, 2008; *Murray et al.*, 2010; *Straneo and Heimbach*, 2013) has lead to the hypothesis that the two occurrences are connected. This is supported by model experiments (*Nick et al.*, 2009).

The North-East Greenland Ice Stream (NEGIS) drains 15% of the Greenland ice-sheet (*Rignot and Kanagaratnam*, 2006). Its two largest outlet glaciers are Zacharias Isstrømen (ZI) and Nioghalvfjerdsfjorden, also known as '79N Glacier' (see Figure 2 for location).

Troughs on the NE-Greenland Shelf The shelf in front of the ZI and 79N Glaciers is wide and features two troughs, Westwind Trough in the north and Norske Trough in the south (Figure 2). These troughs may provide a pathway for warm, saline water to the 79N Glacier and ZI (*Schaffer et al.*, 2017; *Wilson and Straneo*, 2015; *Mayer et al.*, 2000). The south-eastern part of Norske Trough is often called Belgica Trough in older literature (*Bourke et al.*, 1987). 79N Glacier has a second front in Dijmphna Sund (Figure 2) which is separated from Westwind Trough by a 170 m deep sill (*Wilson and Straneo*, 2015). Warmest AW was found to enter the cavity underneath the glacier's floating ice-tongue mainly via Norske Trough and the pinned front (*Wilson and Straneo*, 2015; *Schaffer*

et al., 2017). Waters in Dijmphna Sund were found to be distinct both from waters underneath the ice-tongue as well as waters in Westwind and Norske Trough, leading to the conclusion that transport of deep and warm watermasses through Dijmphna Sund is restricted (*Wilson and Straneo*, 2015). AW in Westwind Trough was reported to be colder than in Norske Trough (*Schaffer et al.*, 2017). The entrance to Westwind Trough is narrower than the entrance to Norske Trough and flow through Westwind Trough may be restricted by a 240 m deep sill half way between the glacier and the trough's entrance (*Schaffer et al.*, 2017).

Sea-Ice and Glaciers The region where the glacier loses contact to the underlying bedrock and starts to float is called the grounding line. If no floating ice-tongue is present the calving front is at the grounding line. Land-fast sea-ice in front of the floating ice-tongue of the 79N Glacier inhibits calving from the glacier and thus has an influence on the dynamics of the glacier and its mass loss (*Reeh et al.*, 2001). When stabilizing land-fast sea-ice is present, calving is inhibited and mass loss occurs mainly as submarine or surface melting. Without the stabilizing sea-ice, the glacier loses mass by calving and submarine melt. This has effects on where fresh water is released into the ocean (at the glacier terminus from melting or spread over a wider region as icebergs drift away and gradually melt) and thus on deep water and sea-ice formation (*Reeh et al.*, 2001).

Glaciers' Rates of Change Within a few kilometres of the grounding line 79N Glacier was found to thin at rates of 0.9 ± 0.1 m yr^{-1} between 1999 to 2012 with the rate increasing to 1.4 ± 0.5 m yr^{-1} between 2012 and 2014 (*Mouginot et al.*, 2015). The same study reported ZI to be thinning at rates of 0.5 ± 0.1 m yr^{-1} between 1999 and 2010 and 5.1 ± 0.3 m yr^{-1} between 2010 and 2014 4.5 km upstream of its 2014 grounding line. This occurred together with grounding line retreat and a large acceleration of ZI, which is thought to now be losing mass. This mass loss extends at least 100 km upstream along the NEGIS (*Thomas et al.*, 2009; *Helm et al.*, 2014). The entire NEGIS has been reported to undergo dynamic thinning (*Khan et al.*, 2014). 79N Glacier is still thought to be in mass balance and shows only small grounding line retreat, even though submarine melting at both glaciers appears to have increased (*Mouginot et al.*, 2015). Thinning at 79N Glacier extends at least 150 km upstream of its grounding line (*Thomas et al.*, 2009).

These records of thinning and mass loss coincide with records of warmer AW in Fram Strait (*Beszczynska-Möller et al.*, 2012) as well as in the Arctic Ocean (*Polyakov et al.*, 2010) suggesting a connection. A feedback between the strength and temperature of the
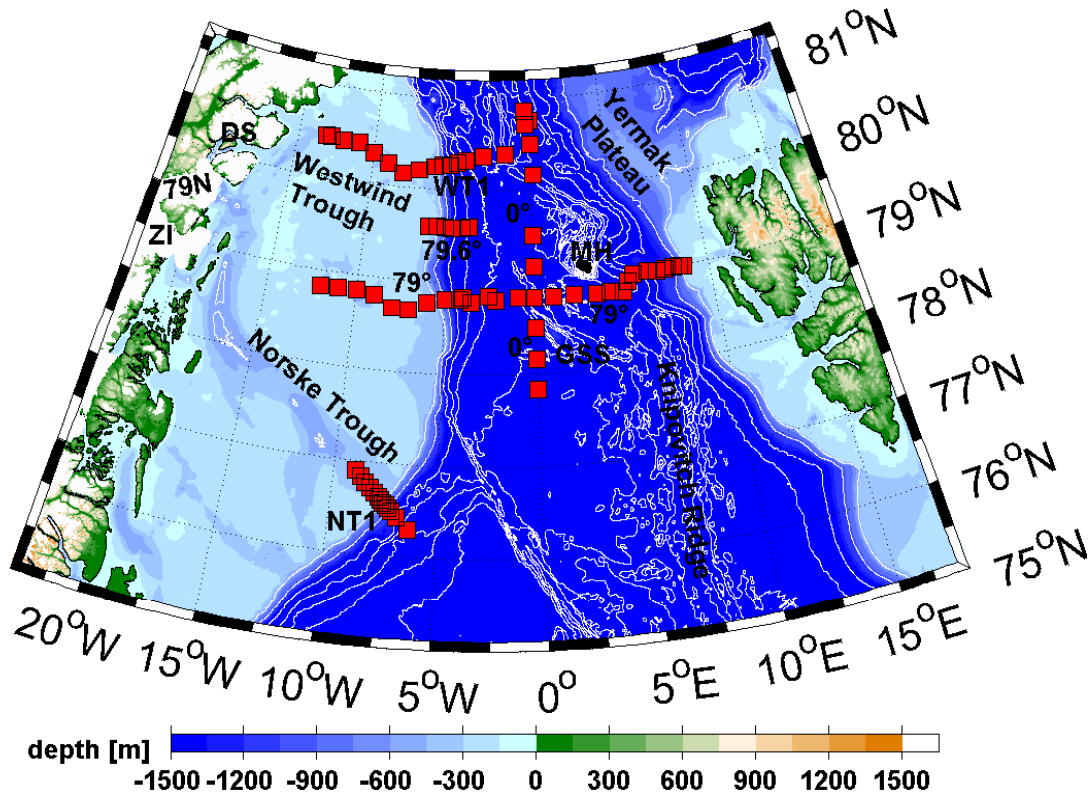
Figure 2: Map of Fram Strait between East Greenland and Svalbard. Station locations are shown in red. Section names are WT1, 79.6°N, ~79°N, NT1, 0°EW. Station information is shown in Table 4. The locations of Norske and Westwind Trough, 79N Glacier (79N), Dijmphna Sund (DS), Yermak Plateau, Knipovitch Ridge, Greenland-Spitsbergen Sill (GSS) and Molloy Hole (MH) are shown. Bathymetry from (*Schaffer et al.*, 2016), map modified from *Schaffer*, pers.comm. 2017.

EGC and Greenland glacier dynamics was proposed by *Murray et al.* (2010).

1.2 Study Area

Fram Strait is the oceanic region located between Greenland and Svalbard, i.e. to the east of the aforementioned glaciers. It plays a role in nutrient exchange between the Arctic Ocean and the North Atlantic (*Torres-Valdés et al.*, 2013). It is a pathway for sea-ice export from the Arctic Ocean, a process that is influenced both by the southward flowing currents in Fram Strait and regional wind forcing (*Halvorsen et al.*, 2015). Fram Strait is the only deep connection between the Arctic Ocean and the Nordic Seas,

formation areas for both Arctic deep water and North Atlantic Deep Water. This makes it a key area for both deep water formation and export as well as ice-ocean interaction. Processes on the Northeast Greenland shelf are only poorly understood, even though at some latitudes in Fram Strait the Greenland shelf is as wide as the deep Fram Strait itself.

On its western side Fram Strait is bounded by Greenland, on the eastern side it is bounded by Svalbard. The two largest currents in Fram Strait are the northward flowing West Spitsbergen Current (WSC) and the southward flowing East Greenland Current (EGC). The WSC is located on the eastern side of Fram Strait and transports relatively warm and salty Atlantic Water (AW) northwards (see *Hanzlick*, 1983, for a review of early studies of the WSC). Not all of the AW reaches the Arctic Ocean, part of it flows westward in Fram Strait before joining the EGC, this is called recirculation and was first proposed by *Ryder* (1895, pg. 204). The EGC is located offshore of the Greenland shelf break on the western side of Fram Strait and transports relatively fresh and cold Polar Water (PW) and sea-ice from the Arctic southwards (see *Aagaard and Coachman*, 1968, for a review of early observations of the EGC). In addition to PW and sea-ice the EGC transports recirculated AW and modified Arctic Atlantic Water (AAW). As AW flows around the Arctic Ocean in a cyclonic boundary current it is modified forming AAW which is colder and fresher than AW (*Schauer et al.*, 1997; *Rudels et al.*, 2005, 2012). The currents and different watermasses are clearly visible in temperature and velocity cross-sections. Figure 3 shows average temperature and velocity in Fram Strait measured by a mooring array at 78°50'N. On the eastern side warm water is transported northwards (the WSC) whereas on the western side cold water is located above and shorewards of warmer water. When examining the velocity measurements in this area it becomes clear that both cold and warmer watermasses (warmer than 2°C at 3°W) are transported southwards in the EGC. The watermasses can be distinguished by their temperature and salinity. In some cases depth, density and/or gradients are also used. Figure 4 shows watermass definitions from *Rudels et al.* (2002) using temperature, salinity and density criteria and in the case of Return Atlantic Water (RAW) and AAW gradients in TS-space and gradients with depth. The figure clearly shows the difference in watermasses found in the WSC (shown in red) vs the region of Arctic Ocean outflow (in blue).
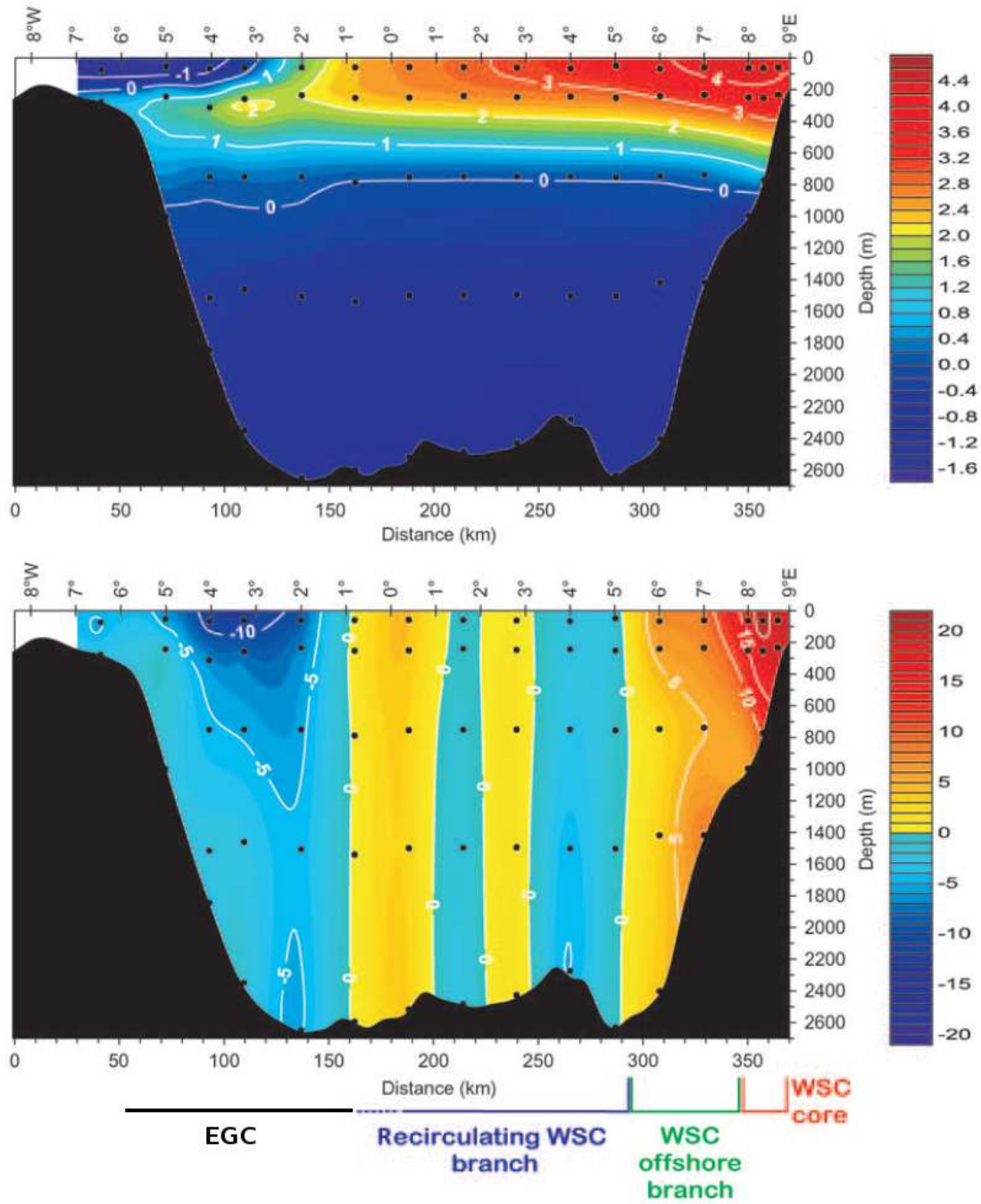
Figure 3: Mean temperature (upper panel, in °C) and meridional velocity (lower panel, normal to the mooring array, in cm/s, positive values are northward) at 78°50'N. Measurements were averaged from summer 2002 to summer 2008. On the right is east, close to the Svalbard shelf, on the left the Greenland shelf. Black dots are instrument locations. Positive velocities are northward, negative velocities are southward. Figure adapted from *Beszczynska-Möller et al.* (2012).

7
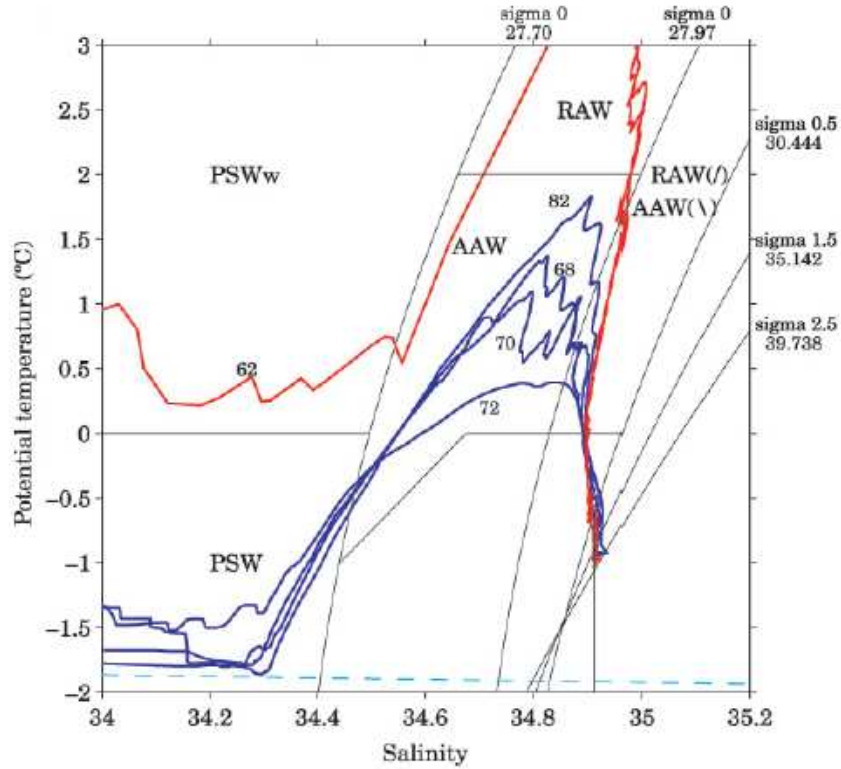
Figure 4: Potential temperature (Θ) – salinity plot. PSWw–warm Polar Surface Water; PSW–Polar Surface Water; RAW–Return Atlantic Water (in our study this watermass is called AW); AAW–Arctic Atlantic Water. RAW and AAW *sigma*>27.97 are distinguished by their depth gradient shown in brackets. Blue stations were taken in the Arctic Ocean outflow around 82°N, red stations are from the WSC around 79°N. Figure from *Rudels et al.* (2002)

1.3   Currents

1.3.1   West Spitsbergen Current

The WSC is a complex flow with barotropic and baroclinic components, that splits into multiple branches and produces eddies. It can be barotropically and baroclinically unstable, mainly during winter and spring (*Teigen et al.*, 2010, 2011). The WSC splits into three main branches (*Quadfasel et al.*, 1987), the Svalbard and Yermak branches (*Perkin and Lewis*, 1984) and the Return Atlantic Current (RAC) (*Gascard et al.*, 1995). The Svalbard branch follows the north-western coast of Svalbard crossing the Yermak Plateau (see Figure 2). This limits its depth range to about 600 m (*Rudels et al.*, 2005; *Schauer et al.*, 2008). The current has been assumed to be the main flow of AW into

the Arctic (*Manley*, 1995).

The flow along the western slope of the Yermak Plateau is called Yermak branch. It is suspected to largely recirculate in the northern Fram Strait (*Manley*, 1995).

Both the Yermak and Svalbard branches are colder and fresher than water in the WSC due to heat loss to the atmosphere and sea-ice-melt and to interactions with cold, dense waters from the Svalbard shelf (*Rudels et al.*, 2005).

1.3.2 Recirculation

The term Return Atlantic Current (RAC) has been used for the westward transport of recirculating AW in Fram Strait. However, the term 'current' is misleading as the westward transport of AW has variously been described as a branch of the Greenland Sea Gyre in the southern part of Fram Strait, a stationary eddy at the Molloy Hole (see Figure 2 for location) (*Hattermann et al.*, 2016) and an eddy field in Fram Strait (*Gascard et al.*, 1988). *Gascard et al.* (1995) described the entire RAC as topographically steered eddies, shed by the WSC and eventually merging with the EGC. These eddies are also able to subduct AW underneath the sea-ice and Polar Water advected from the north in the EGC (*Hattermann et al.*, 2016).

Recirculation Transport and Extent It is estimated that only about half of the AW flowing northward in Fram Strait enters the Arctic, the other half recirculates (*Rudels*, 1987; *Marnela et al.*, 2013). Some authors even estimate that 2/3 of the AW entering Fram Strait recirculates (*Manley*, 1995). An overview of recirculation estimates found in the literature is shown in Table 3. When estimating the transport of the recirculation some confusion might arise, as different definitions of recirculation are used. Some authors calculate net east-west transport through meridional sections (e.g. *Marnela et al.*, 2013) or examine the transport of the EGC (e.g. *Fahrbach et al.*, 2001; *de Steur et al.*, 2014) or EGC and WSC (e.g. *Schlichtholz and Houssais*, 1999a,b). Others use budget calculations from transports and mixing ratios to arrive at AW recirculation (*Marnela et al.*, 2008). The recirculation in Fram Strait is associated with different structures and processes and transports AW with different properties as outlined below. The meridional extent of the recirculation is at present unclear. *Rudels et al.* (2005) found no recirculating AW at ~81°N but did find it at 79°N. This is supported by *Marnela et al.* (2013) who found most of the recirculation to occur south of 81–82°N and the strongest recirculation at and south of 79°N. Though recirculation as far north as 82°N appears to exist as documented by a drifter path reported in (*Gascard et al.*, 1995). Due to heavy sea-ice conditions there are hardly any observational studies further to the north

(one study on Arctic water outflow using data from 82–83°N is presented in *Falck et al.* (2005). This study area is to the east and north of our expected maximum extent of the recirculation and may thus show the EGC outside of the influence of the recirculation). Models cannot help because of issues with resolution (both of the model and bathymetry) and parametrization of e.g. mixing and interactions with sea-ice. Without knowledge of the meridional extent of the recirculation we cannot explain watermass pathways through Westwind and Norske Trough on the Greenland Shelf, and thus to the NEGIS outlet glaciers, or AW transformation in and travel times across Fram Strait.

Recirculation Structure   In model results the westward flow of AW south of 78.5°N appears to trace bathymetric features and is described as the eastern branch of the Greenland Sea Gyre (*Hattermann et al.*, 2016) or as a feature dubbed Knipovitch Branch following the Knipovitch Ridge and the Greenland-Spitsbergen Sill (GSS, see Figure 2) to join the EGC (*Aksenov et al.*, 2010). In both model results the AW transported westward in these structures is relatively colder than that continuing northward in the WSC and/or recirculating further to the north. Most of the westward transport of warmer AW in the model of *Hattermann et al.* (2016) is due to the existence of a stationary eddy over the Molloy Hole at 80°N and follows the northern rim of the hole. This stationary eddy was also seen in observations (*Johannessen et al.*, 1987; *Quadfasel et al.*, 1987) further to the south around 79°30'N 3°E. Model results were found to be strongly dependent on both horizontal and vertical resolution (*Fieg et al.*, 2010) which can cause differences in circulation between models and observations.

The Mooring Array at 78°50'N   Over the years, different estimates of the recirculation in and transport through Fram Strait were made. The zonal section most frequently occupied lies at 78°50'N between Svalbard and Greenland. An array of moorings spanning the Strait has made long term observations possible. An average of temperatures and velocities through the mooring section between summer 2002 and summer 2008 is shown in Figure 3.

Temperature   The mooring array recorded two warm anomalies passing through Fram Strait in 1999–2000 and 2005–2007 and a general warming trend of AW between 1997 and 2010 of 0.06 °C per year but no increase in AW volume transport (*Beszczynska-Möller et al.*, 2012). This agrees with the warming trend of 0.058 °C yr⁻¹ from summer CTD sections across the WSC at 76°30'N that was reported by *Walczowski et al.* (2017) for the upper 400 m of the watercolumn over the time period 1996–2016. The increase

in temperature between 400 and 1000 m was lower (0.015 ℃ yr⁻¹) but still statistically significant. Net northward heat transport through Fram Strait between 1997 and 2007 reached a maximum in 2004 but decreased again even though the temperature of AW transported northwards in the WSC did not decrease (*Schauer et al.*, 2008).

Eddies   Eddy activity is often expressed as eddy kinetic energy (EKE) which is the kinetic energy from variations in the horizontal velocity components. The variation in eddy activity has been associated with shelf waves (*Nilsen et al.*, 2006) and with local wind forcing (*Jónsson et al.*, 1992). However, recent research has found that greater baroclinic instability of the WSC in winter compared to summer (*Teigen et al.*, 2011) can explain the higher eddy activity seen in Fram Strait (*von Appen et al.*, 2016). The instabilities are associated with the decreased stratification of the upper water column in winter due to stronger atmospheric cooling and local wind forcing is not required to explain the eddy activity (*von Appen et al.*, 2016).

1.3.3   East Greenland Current

The EGC at 78°50'N is seasonal, more barotropic and transports warmer AW than the EGC at 79°N (*de Steur et al.*, 2014). No seasonal signal was found at 79°N. This is explained by flow from the wind driven Greenland Sea Gyre joining the EGC between these locations. This pattern in seasonality is in conflict with the results from *Hattermann et al.* (2016) who found that the northern recirculation is seasonal, with an increase in winter when eddy activity is high. That the water in the EGC at 78°50'N should be warmer after the southern recirculation branch has joined the EGC at first seems to contradict the results from model studies which show colder AW recirculation in the Greenland Sea Gyre than further north (*Hattermann et al.*, 2016; *Aksenov et al.*, 2010). The observations by *de Steur et al.* (2014) may be influenced however by a warm anomaly passing through Fram Strait after the mooring line was shifted (*de Steur et al.*, 2014). Alternatively the AW transported by eddies may be subject to stronger atmospheric cooling or mixing with colder watermasses and thus have lower temperatures when reaching the EGC. So far there were no studies that examined the EGC north of 79°N and the northern recirculation in Fram Strait with a high enough horizontal resolution to resolve these issues conclusively.

A study of the EGC between Fram Strait (south of 78°N) and Denmark Strait concluded that the EGC there is made up of three branches: an inshore branch transporting fresh cold water, a shelf-break branch and a branch offshore of the shelfbreak believed to be a direct recirculation of AW from the western WSC branch *Håvik et al.* (2017). Further to

the south, just north of Denmark Strait the EGC plays an important role in transporting Denmark Strait Overflow Water and freshwater thus influencing regional processes, deep convection and the AMOC (*Rudels et al.*, 2012; *Våge et al.*, 2013).

1.4   Aims and Hypotheses

The aim of the thesis proposed here is to utilize the first comprehensive data set in northern Fram Strait to describe the structure of the recirculation of AW in Fram Strait and to quantify the westward transport in the northern recirculation and the southward transport in the EGC as a function of the different watermasses. I will test two hypotheses:

1. **Atlantic Water (AW) that recirculates in Fram Strait joins the EGC south of Westwind Trough**
   Westwind trough is the northern entrance to a trough system on the Greenland shelf (Figure 2) which connects to the marine termini of the North East Greenland Icestream outlet glaciers. We do not expect to find recirculated AW at the hydrographic section at the mouth of Westwind Trough but do expect to find it in the three EGC cross-sections further to the south. Section locations are shown in Figure 2.

2. **In the EGC recirculating Atlantic Water (AW) is found offshore of Polar Water (PW) and Arctic Atlantic Water (AAW) from the Arctic Ocean**
   We expect PW and AAW at the Greenland shelfbreak in all our sections crossing the EGC (WT1, 79.6°N, ~79°N and NT1, locations in Figure 2) but expect recirculated AW offshore of the shelfbreak. This horizontal watermass structure in the EGC would prevent recirculated AW from flowing onto the shelf and into troughs.

The expected watermass structure in the EGC and the recirculation would explain why AW is not found on the Greenland shelf outside of deep troughs. It would further explain the difference in watermass properties found between Norske and Westwind Troughs. A better understanding of AW pathways in Fram Strait and the EGC can inform research on the pathways of AW on the shelf and thus interactions with the outflow from the NEGIS via ZI and 79N Glacier. This work represents the first study of both the recirculation at 0°EW and the EGC north of 79°N as well as the entrances to Norske and Westwind Troughs on synoptic timescales. It aims to follow the AW from the WSC in the east through the 0°EW section to the sections sampling the EGC and the troughs in the west. Thus showing not only north-south transport in Fram Strait

but also east-west transport and at what latitude how much of the recirculation joins the EGC.

To this end CTD data and ADCP velocity data from the cruise PS100 of *RV Polarstern* collected in Fram Strait in summer 2016 will be analysed. It is important to use CTD data together with ADCP data as only the baroclinic flow component can be calculated from CTD observations alone and in the EGC the baroclinic and barotropic components of the flow are approximately equal (*Fahrbach et al.*, 2001).

This study connects the insights of *Håvik et al.* (2017) to the south, and of *Schaffer et al.* (2017) to the west with the continuing investigations with the mooring arrays at 78°N 50' and 0°EW. It will be performed in association with the Physical Oceanography Section at the Alfred Wegener Institute, Helmholtz Centre for Polar and Marine Research.

2 Data

Data was collected between 18$^{\text{th}}$ of July and 6$^{\text{th}}$ of September 2016 from *RV Polarstern* as part of the PS100 cruise. The data consists of 75 stations along 5 sections (0°EW, 79°N, WT1, 79.6°N and NT1). Station metadata can be found in Table 4 and locations in Figure 2. CTD casts were recorded with a Seabird 911+ and averaged into 1 m bins (*Kanzow*, 2017). We focus on the CTD records of temperature (T), salinity (S) (calculated from a ratio of conductivities and thus reported without units, as commonly done in physical oceanography), pressure (p) and dissolved oxygen. Density is calculated from T, S and p via the equation of state for seawater EOS-80 (*Fofonoff and Millard Jr*, 1983). A variation of this is also used to calculate potential temperature Θ (*Fofonoff and Millard Jr*, 1983; *Bryden*, 1973). Potential temperature has pressure effects removed and allows for the comparison of watermasses from different depths. Potential density is reported as $\sigma = \rho - 1000$ kg/m³, with ρ the density the waterparcel would have if brought adiabatically to the sea surface. Dissolved oxygen is used as a non-conservative watermass tracer. Watermasses generally have a lower oxygen concentration the longer they have been isolated from the atmosphere and the higher the water temperature. To remove temperature and salinity effects, oxygen saturation (in %) is calculated from temperature, salinity and oxygen concentration using the oxygen saturation value after *Garcia and Gordon* (1992). This can be used to distinguish watermasses and their 'age', that is the time since they were subducted underneath another watermass and thus lost contact with the atmosphere. Conductivity and oxygen sensors were calibrated using water samples taken from Niskin bottles mounted on the CTD rosette. The water samples were analysed with a Optimare Precision Salinometer (measuring conductivity)

on-board *RV Polarstern* and using a titration method (measuring the oxygen concentration) (*Kanzow*, 2017). The Seabird 911+ has an initial accuracy of ± 0.0003 S/m for conductivity, ± 0.001 °C for temperature and ± 0.015 % of the full scale range for pressure (SBE, 2016). An upward and a downward looking 300 kHz RDI Workhorse Acoustic Doppler Current Profiler (ADCP) were attached to the CTD rosette acting as a lowered-ADCP (LADCP) system recording ocean velocities. The LADCP was in operation between stations 041 and 095 and from 106 onwards. The LADCP used a bin size of 4 m and a maximum depth range of 108 m up to the 14th of August when the settings were changed to 8 m and 250 m respectively (*Kanzow*, 2017). A vessel-mounted 150 kHz RDI Ocean Surveyor ADCP (VMADCP) recorded ocean velocities along the cruise track. The VMADCP used a bin size of 4 m and had a range of 15 to 300 m depending on conditions such as sea-state, the presence of ice, the ship's velocity and concentration of scatterers. No data is available for 31.07. 22:00 UTC to 1.08. 6:10 UTC, 15.08. 0:30 UTC to 6:00 UTC, 17.08. 23:00 UTC to 18.08. 6:00 UTC and 28.08. 9:15 UTC to 11:00 UTC (*Kanzow*, 2017). Data is stored on the data publisher PANGAEA (www.pangaea.de). For the link to the CTD data please see *Kanzow et al.* (2017a) and *Kanzow et al.* (2017b). For LADCP data see *von Appen et al.* (2017) and for VMADCP data see *Kanzow and Witte* (2016). Echosouder data is found in *Dorschel and Jensen* (2017). For further information on the onship processing of the raw data please see *Kanzow* (2017).

3   Methods

3.1   Preprocessing and Gridding

At each of the five sections station locations are projected onto a straight line, in the case of 0°EW onto the average longitude (0.0367° E) and for 79° N, 79° N West, 79° N East and 79.6° N onto the average latitude (78.85° N, 78.80° N, 78.97° N and 79.6° N respectively). For sections which do not run parallel to a latitude or longitude a linear best fit of the station locations is used to find a optimal straight line and the stations are projected onto this line retaining their longitude. The section in Westwind Trough is split into two adjacent sections (WT1 West and WT1 East) to minimise the distance between true and projected station locations. Henceforth, 'section' will indicate the interpolated section (a straight line) unless otherwise indicated. Bathymetry from the underway echosounder measurements was projected onto the sections by defining a box around the section in which data was considered. The box had the same longitude range

(or latitude in the case of 0° EW) as the section. The box was then separated into 100 to 300 (depending on section length) strips of equal width and only the track point closest to the section within each strip was retained and projected onto the section. Outliers were picked manually and removed, resulting gaps were then closed by linear interpolation where needed. The bathymetry so obtained from the echosounder was compared to the bathymetry in IBCAO (*Jakobsson et al.*, 2012) and to the depths measured at each station which were linearly interpolated onto the section. In most cases the station depth agreed with the underway echosounder data to within 10s of meters which caused us to use the linearly interpolated station depth to plot the bathymetry in the sections. In section WT1 the location of the shelfbreak was corrected using the echosounder bathymetry. The easternmost bathymetry at 79°N near the Svalbard shelf was corrected using IBCAO bathymetry of the Svalbard shelfbreak as our section did not extend far enough east to capture this. The largest deviations between the different bathymetries was found in section 0°EW below 2000m, due to very rugged topography and gappy echosounder data. Here the bathymetry from IBCAO (which agreed qualitatively with the underway echosounder data, where available) was used for the entire section and hydrographical values appearing below the so defined seafloor set to NaN before plotting.

For each section the station data (CTD, LADCP and VMADCP) was interpolated onto a common grid (grid A) with vertical resolution of 10 m and a horizontal resolution of half the mean station distance of each section (ranging from 5 to 20 km). In cases where two stations were very close together or multiple CTD casts at a single station were available, we only included the deepest cast. If this criterion was not sufficient we included the cast that was closest to the neighbouring casts in time. The casts included in the gridding routine are marked in Table 4 in the Appendix. Interpolation was done using a minimum curvature surface under tension method (*Smith and Wessel*, 1990) (also called Laplacian-Spline method) as implemented in the MATLAB toolbox *ppzgrid* coded by Roger Goldsmith (Woods Hole Oceanographic Institution, WHOI) and provided by Chris Linder (WHOI). A standard tension of 5 was used (0 = laplacian interpolation, ∞ = spline interpolation), the search radius was set to ± 10 grid points to be able to attain smooth results in areas of lower data coverage (as in the deep ocean). Areas below the sea floor were not considered in the interpolation. To avoid loss of data points during the calculation of geostrophic shear, virtual stations with the hydrographic data of the first and last station in any one section were added to the beginning and end of the sections before gridding (see Figure 5). The horizontal distance of the first and last station to these virtual stations was chosen to equal the horizontal grid spacing in
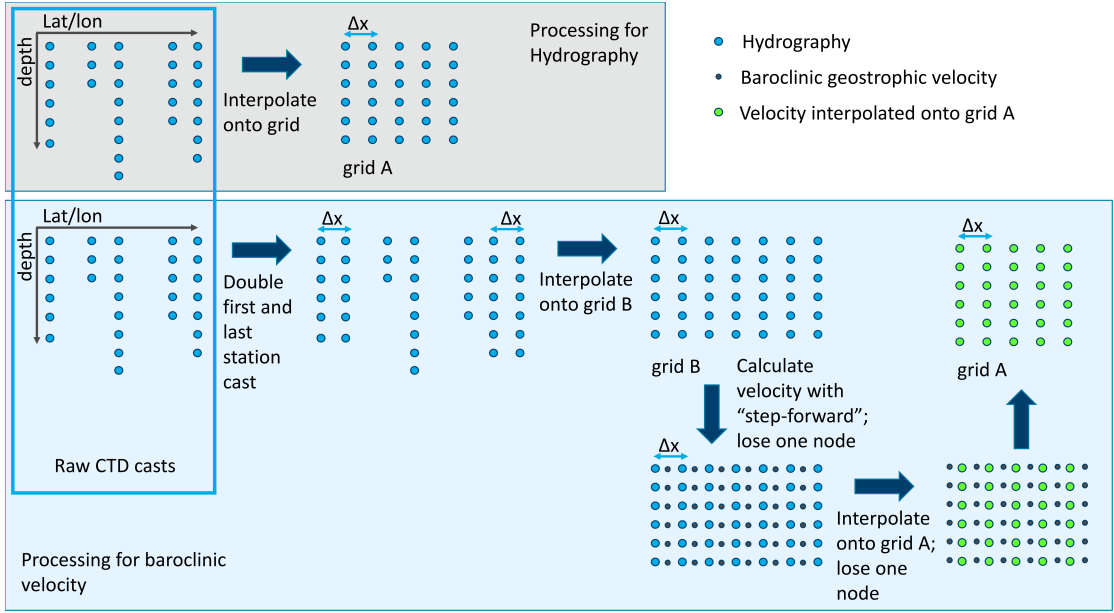
Figure 5: Schematic showing the steps for gridding hydrography (upper panel) and velocity (lower panel).

grid A. Interpolation as described above produced a grid (grid B) of hydrographic data with two more nodes in the horizontal than grid A. This larger grid was then passed to the routine for calculating geostrophic shear. Grid B was used solely for geostrophic shear calculations and not for i.e. watermass analysis. Geostrophic shear was calculated numerically with the forward step method due to relatively low horizontal resolution and linearly interpolated onto grid A.

3.2   Velocity Calculation

Baroclinic geostrophic velocities are calculated from hydrography along the following steps: The geostrophic relationship assumes a balance of Coriolis force and pressure gradient force. In a right-handed coordinate system this can be expressed as

$$-fv = -\frac{1}{\rho}\frac{\partial p}{\partial x} \tag{1}$$

Here f is the Coriolis parameter, v the horizontal velocity vector perpendicular to the investigated section, ρ the density of seawater, p pressure from hydrographic measurements and x the horizontal vector in the plane of the investigated section. Multiplying by ρ and taking the partial derivative with respect to z, which is the vertical coordinate

16

(upwards is positive), gives

$$-\frac{\partial}{\partial z}\left(\rho f v\right) = -\frac{\partial}{\partial x}\frac{\partial p}{\partial z} \tag{2}$$

Here we use the hydrostatic relationship $\frac{\partial p}{\partial z} = -\rho g$, with g the gravitational acceleration. Inserting this into Equation (2) yields

$$-\frac{\partial}{\partial z}\left(\rho f v\right) = g\frac{\partial \rho}{\partial x} \tag{3}$$

Using the Boussinesq approximation we can neglect the term $v\frac{\partial \rho}{\partial z}$ as it is small compared with $\rho\frac{\partial v}{\partial z}$ which gives us

$$-\frac{\partial v}{\partial z} = \frac{g}{\rho f}\frac{\partial \rho}{\partial x} \tag{4}$$

Going from partial derivatives to finite differences we arrive at

$$-\frac{\Delta v}{\Delta z} = \frac{g}{\rho f}\frac{\Delta \rho}{\Delta x} \tag{5}$$

which can then be integrated in the vertical giving us the horizontal velocity perpendicular to a measured section of density up to an integration constant. This is done for every grid point. Transports through the sections are then calculated by multiplying the velocity by the area through which it flows.

In order to enable us to compare our results with other estimates of the AW recirculation (Table 3) we have not attempted to impose constraints on the transports calculated as done e.g. in *Marnela et al.* (2013) where salt, heat and volume conservation was applied between sections. This is also the reason why we calculated baroclinic transports as well as barotropic and absolute geostrophic transports.

The integration constant from the calculation of baroclinic geostrophic velocities is the barotropic geostrophic velocity component which is constant with depth. In our case, we can reference our baroclinic velocity profiles to the ADCP measurements to get absolute geostrophic velocities. Since the LADCP measures velocity in instrument coordinates we have to correct for movement of the LADCP relative to our absolute coordinate system (pitch and roll, vertical and horizontal velocity and rotation of the instrument). For a description of LADCP profiling and analysis methods see *Fischer and Visbeck* (1993); *Visbeck* (2002); *Thurnherr* (2010). LADCP velocity profiles can be calculated via integration ("shear method" *Fischer and Visbeck*, 1993) or with a least squares approach

("inverse method" *Visbeck*, 2002). Velocities from the shear method were discarded due to unrealistically high gradients and velocities. Due to increased velocity errors when the ship is in transit (*Osinski*, 2000), only those VMADCP measurements collected whilst the ship was on station were used. These were averaged over the time the ship was on station to attain a single velocity-depth profile for each station. LADCP and VMADCP velocities were detided by subtracting the barotropic tidal component calculated from the Arctic Ocean Tidal Inverse Model (AOTIM) (*Padman and Erofeeva*, 2004). When sections were not north-south or east-west oriented, velocities from the ADCP measurements were rotated such that the horizontal velocity u lies in the section plane and horizontal velocity v is positive into the section plane, thus matching the sign of the baroclinic geostrophic velocity. The ADCP velocities were averaged between 50-150 m depth. This range was chosen as the interval in which there was least spread in successive VMADCP measurements whilst on station suggesting that this depth range was least affected by errors. Variation of the interval bounds by some tens of meters did not greatly change the resulting velocity averages, implying that the results are not substantially biased by our choice. The average of the baroclinic velocity over the chosen depth interval was then subtracted leaving the depth independent (barotropic) part of the velocity. Results from VMADCP and LADCP were then compared. Strong deviations could be traced back to differences in section resolution (in general VMADCP resolution was higher as LADCP casts were not performed at all stations) or high uncertainties in the LADCP velocity calculation. It was found that the LADCP performed better than the VMADCP only in section NT1 (due to data gaps in the VMADCP section). This lead us to use the barotropic velocities calculated from VMADCP for further analysis for all sections except NT1 where the LADCP data was used. To get the absolute velocity over the entire water column, the baroclinic velocity is added to the depth varying profile calculated from hydrography (*Osinski et al.*, 2003; *Meinen et al.*, 2000) thus acting as the integration constant. It has to be noted that velocities from ageostrophic processes, such as tides, wind, frontogenesis and internal waves produce unknown (except for the tides) errors in this calculation (*Osinski et al.*, 2003; *Meinen et al.*, 2000).

We defined the EGC following *Håvik et al.* (2017). The EGC core was identified as the location of the maximum mean southward velocity in the upper 150 m of the watercolumn, the boundary of the EGC was set to the locations at which the mean velocity in the upper 150 m had decreased to 20% of the core value.
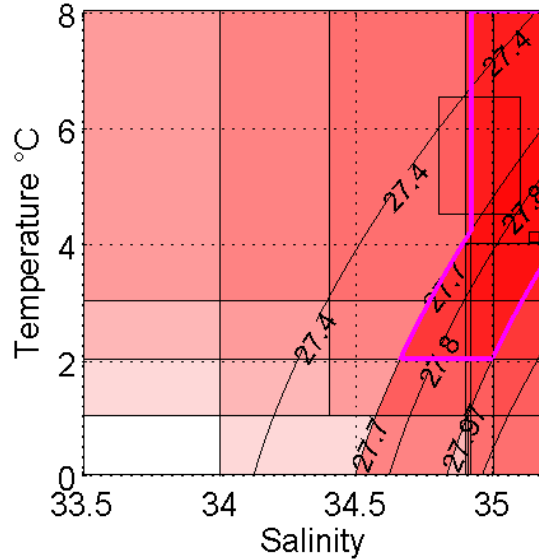
Figure 6: Boundaries of AW definitions in the Arctic Mediterranean as shown in Table 5. Areas overlap, the stronger the saturation the more authors assign an area in θ-S space to AW. The definition we use is outlined in the bold magenta line.

3.3   Watermasses

Watermass definitions (see Table 1) follow *Rudels et al.* (2005) except for very warm AW. Following *Walczowski et al.* (2017)), we here include water lighter than 27.7 kg/m^3 with salinities above 34.92 in our definition of AW. This definition ensures that surface water in the WSC is defined as AW. The salinity boundary at 34.92 is also low enough that all deep temperature maxima in the AW domain defined by *Rudels et al.* (2005) observed in our study area are included. Our choice of AW definition can be seen in Figure 6 in context with other AW definitions from the literature (see Atlantic Water in Table 5 for the boundaries used). The choice of AW definition depends both on the scientific question examined as well as the study area. Since a discussion of the details of watermass definitions in the literature is beyond the scope of this study, the reader is referred to the table of watermass definitions found in the Appendix (Table 5). θ-S diagrams of the station data were plotted for each section (discussed later in Section 4.2). They were used to define watermasses as follows: The deep temperature maximum was defined as either the overall temperature maximum (at stations where the temperature maximum was not at the surface) or as the salinity maximum. In cases where both criteria were not able to capture the θ-S peak in the AW or AAW domain the peak was

Table 1: Watermass definitions after *Rudels et al.* (2005). Boundaries of potential temperature θ in °C and potential density σ in kg/m³ are given. σ_θ is potential density referenced to the sea surface, $\sigma_{0.5}$ is potential density referenced to 500 m and $\sigma_{1.5}$ is potential density referenced to 1500 m.

Watermass	Acronym	Definition
Polar Surface Water	PSW	$\sigma_\theta \leq 27.70, \theta \leq 0$
warm Polar Surface Water	PSWw	$\sigma_\theta \leq 27.70, 0 < \theta$
Atlantic Water	AW	$27.70 < \sigma_\theta \leq 27.97, 2 < \theta$ $27.97 < \sigma_\theta, \sigma_{0.5} \leq 30.444, 0 < \theta$[1]
Arctic Atlantic Water	AAW	$27.70 < \sigma_\theta \leq 29.97, 0 < \theta \leq 2$ $27.97 < \sigma_\theta, \sigma_{0.5} \leq 30.444, 0 < \theta$[2]
Arctic Intermediate Water	AIW	$27.97 < \sigma_\theta, \sigma_{0.5} \leq 30.444, \theta \leq 0$[1]
upper Polar Deep Water	uPDW	$27.97 < \sigma_\theta, \sigma_{0.5} \leq 30.444, \theta \leq 0$[2]
Nordic Seas Deep Water	NDW	$30.444 < \sigma_{0.5}, S \leq 34.915$
Canadian Basin Deep Water	CBDW	$30.444 < \sigma_{0.5}, \sigma_{1.5} \leq 35.142, 34.915 < S$
Eurasian Basin Deep Water	EBDW	$35.142 < \sigma_{1.5}, 34.914 < S$

[1] θ decreasing, S decreasing with depth: only temperature stratified
[2] θ decreasing, S increasing with depth: doubly stable

picked manually. This was only the case at 12 stations (at three stations in the WSC at 79°N, at the three southern stations along 0°EW and at six stations in the inner trough at WT1). Additionally we define DSOW (Denmark Strait Overflow Water) as water above 800 m depth and denser than 27.8 kg/m³.

Watermass endmembers chosen to calculate mixing ratios are shown in Table 2. AW was selected as the warmest θ-S peak found in the eastern casts of section 79°N (the region of AW inflow and the WSC). This necessarily is colder than the surface water in the WSC which we still call AW and also colder than some of the deep θ-S maxima picked in the WSC and at 0°EW. Our definition of the AW endmember lies close to that chosen by *Håvik et al.* (2017) of θ=4.1°C and S=35.1 for their study of the EGC south of 79°N. Our AW salinity is within the climatological values in the WSC in 75 m depth for July and August (*von Appen et al.*, 2016). Nevertheless, our chosen temperature value is well below the temperatures in the WSC at that depth. This means that water in the south-eastern part of Fram Strait (at the onset of the recirculation) is too warm to fall into our mixing triangle; mixing ratios in that area can therefore not be calculated, since this is not our focus, that is not a serious limitation of our method. We work with our value of 4.09°C for AW as it is able to capture the properties of the AW we observe

Table 2: Table of the watermass endmember definitions used to calculate mixing ratios. AW is Atlantic Water, AAW is Arctic Atlantic Water, PSW is Polar Surface Water and DW stands for Deep Water.

WM.	Temp. °C	Sal.
AW	4.09	35.10
AAW	0.80	34.80
PSW	-1.83	34.17
DW	-0.89	34.93

once it is no longer in contact with the atmosphere and thus no longer undergoing transformation through direct air-sea fluxes. AAW was picked as the coldest T-S peak in the AAW domain defined above. PSW is defined as the coldest water recorded in our measurements, lying on the freezing line at the point where temperature changes from slowly decreasing with increasing salinity, due to the lowering of the freezing point with increasing salinity, to sharply increasing with salinity. Deep Water (DW) is not a specific deep watermass like the ones shown in Table 1, but we set it to the T and S properties of the deepest water sampled (in section 0°EW). From these endmembers two mixing triangles were formed: a AW-AAW-PSW triangle and a AW-AAW-DW triangle (see Figure 7). Our observed watermasses were either composed of a AW-AAW mixture with a contribution of lighter PSW located shallower in the water column, or of a AW-AAW mixture and a contribution of denser DW located deeper. We thus assume that there was no mixing between PSW and DW and the observations can be described either as AW-AAW-PSW or as AW-AAW-DW mixtures. By definition, either the fraction of PSW or of DW must be zero. We established on which side of the AW-AAW mixing line, (dashed line in Figure 7), the PSW or the DW side, a θ-S measurement lay and then calculated the mixing ratio of the three appropriate endmembers. This method allowed us to use only three constraints (heat, salt and volume conservation) in a least-squares approach. In cases where the measured T-S points lay outside of the mixing triangles no mixing ratio was calculated.

3.4   Error Estimates of Velocity

To examine errors made in the gridding process, the CTD and ADCP data were regridded increasing or decreasing tension, search radius and grid resolution individually by a factor of two. From these modified grids absolute geostrophic velocity was calculated. The relative absolute error of the absolute (baroclinic and barotropic) geostrophic ve-
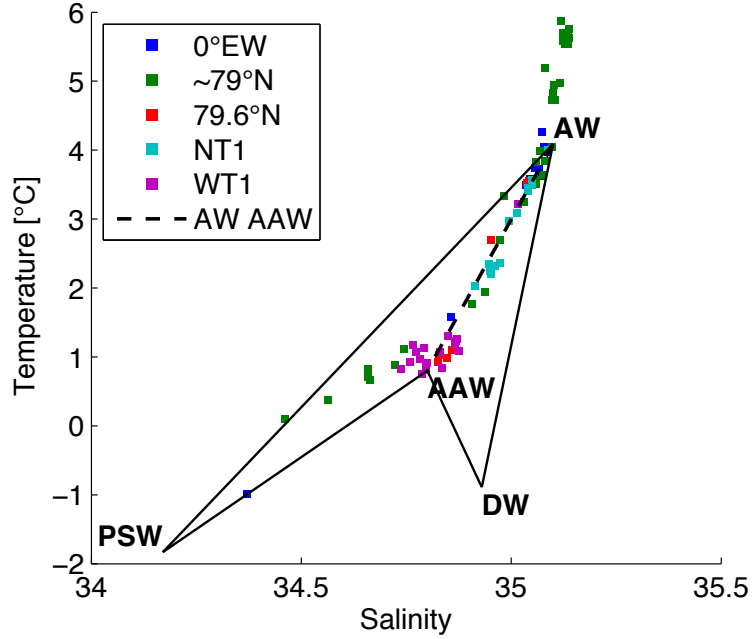
Figure 7: Mixing triangles with endmembers defined as in Table 2. Squares show the properties of the deep θ-S maximum in θ-S space at each station (defined in Section 3.3 and discussed in Section 4.3).

locity between the modified grid and the grid used in this study was determined. To prevent division by zero which would result in misleadingly large relative errors in areas where the original absolute velocity is small or changes sign, all velocity points with an absolute value below 0.05 m/s were set to 0.05 m/s.

The error of the VMADCP measurements was calculated as the median absolute deviation in time (multiple measurements whilst the ship was on station) and space (between 50 and 150 m, the depth range used to calculate the barotropic velocity). The error due to misalignment between the instrument coordinates and natural coordinates was not examined separately (it was corrected for during onship preprocessing (*Kanzow*, 2017)), but is an order of magnitude lower for measurements taken on station compared to the error during the time the ship is making headway (*Osinski*, 2000). The processing routine for LADCP velocities gives an error estimate dependant on depth for each cast (see *Thurnherr*, 2010; *Kanzow*, 2017, for information on the processing package and error calculation). The error of the LADCP measurements at section NT1 was calculated as the median absolute deviation of this estimate, though in space (50 to 150 m depth) only, as there were no repeat casts at individual stations. We used median absolute deviations as the repeat measurement velocities from the VMADCP and error estimates

of the LADCP were not normally distributed.

# 4   Results

4.1   Hydrography and Velocities

We now describe the potential temperature, salinity, potential density and absolute velocity fields along the path of Atlantic Water (AW) in Fram Strait. We start with the inflow region of AW from the south and the WSC in the east of section 79°N. Next, we turn to the centre of Fram Strait with the western recirculation of AW crossing 0°EW before we follow the path of the EGC along the East Greenland shelf from north to south, shown in sections WT1, 79.6°N, 79°N west of 0°EW, and NT1. Temperature, salinity and density are shown in panels a and b and absolute geostrophic velocity is shown in panel c of Figures 9 – 12.

4.1.1   The AW Inflow and the WSC

Warm, salty water enters the Fram Strait flowing northward in the WSC. The WSC can be seen on the Svalbard slope east of 7.5°E with velocities reaching 0.11 m/s (Figure 8 (c)). The layer of water warmer than 2°C is thickest (over 500 m, see Figure 8 (a)) in the WSC and gets thinner toward the west (<400 m at 0°EW). Water warmer than 5°C is found in the upper 200 m east of 1°EW (~150 km in Figure 8 (a)). The deep 0°C isotherm is located between 500 and 1000 m. Salinity variations are small throughout the section east of 0°EW (Figure 8 (b)) and the density field follows the temperature field. Whilst the isopycnals < 27.8 kg/m³ are almost flat above 100 m depth in the deep Fram Strait (west of 2.5°E), they slope downward toward the east (0.64 m/km in the case of the 27.8 kg/m³ isopycnal) and the 27.8 kg/m³ isopycnal reaches a depth of 150 m in the east. The strong fluctuations of temperature, density and velocity are paired around domes in the density field. The features are approximately 30 km wide regions of alternating northward and southward velocities. The strongest of these lies just east of 5°E (at 250 km in panel 8 (c)) with peak velocities of -0.18 and 0.23 m/s.

4.1.2   The Deep Fram Strait and the Westward Recirculation

At 0°EW temperatures (Figure 9 (a)) are highest at the surface of the southern end of the section. In all watermass properties a strong gradient can be observed at about 150 m depth with the exception of stations in the southern Fram Strait. A tongue of
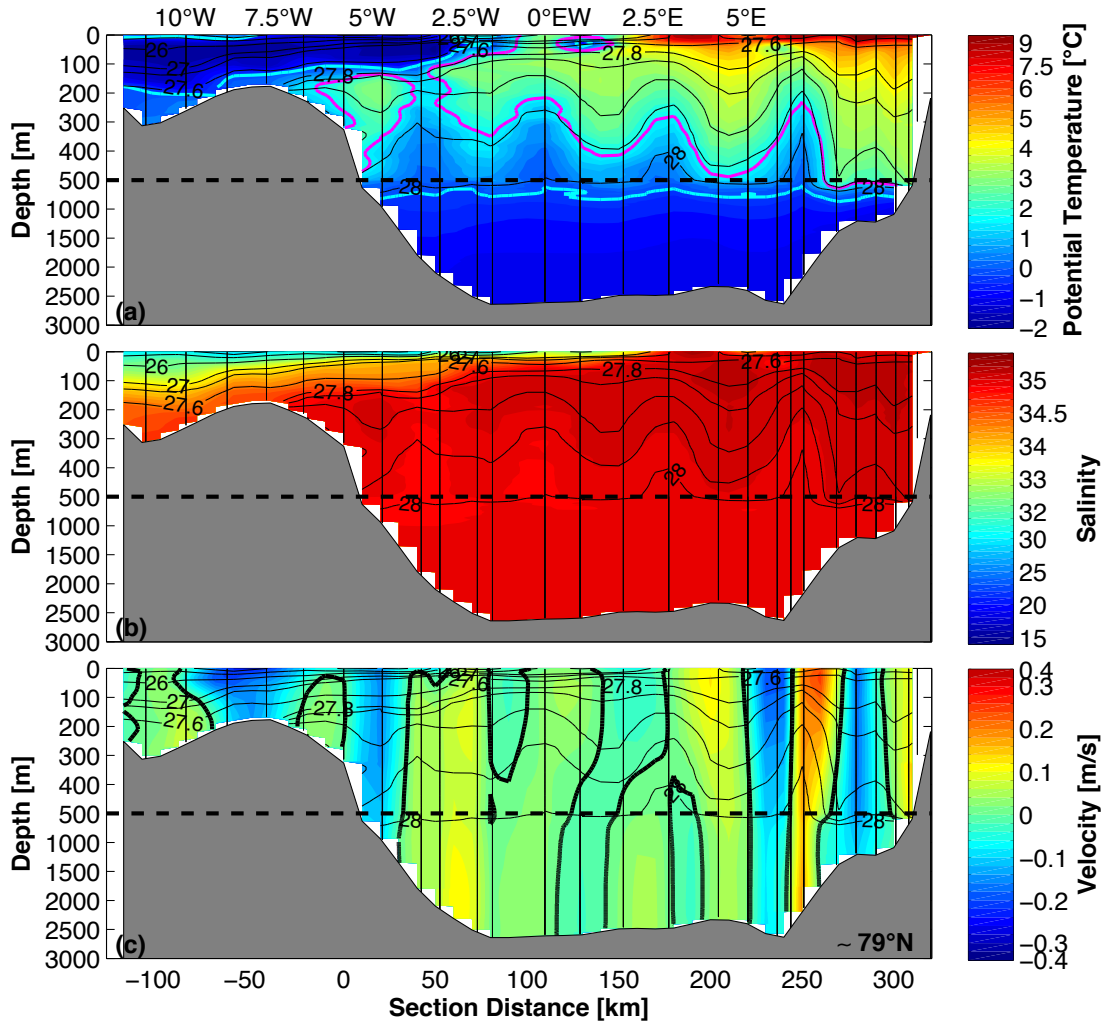
Figure 8: Temperature (a), salinity (b) and absolute geostrophic velocity (c) at section 79°N. Solid thin lines show potential density referenced to 0 dbar in steps of 1 kg/m³ up to 27 kg/m³ and in steps of 0.05 from 27.8 kg/m³ onwards. The 27.3 and 27.6 kg/m³ isopycnals are also shown. Thin vertical lines show station locations and depth. Please note that the y-axis changes scale at 500 m depth (dashed line) and the non-linear colourbars. In panel (a) the magenta contour shows 2 °C, the cyan contour 0 °C. In the bottom panel (c), solid bold lines show the 0 m/s isotach. Positive velocities are northward, negative velocities are southward. Section distance is 0 at the western shelfbreak.
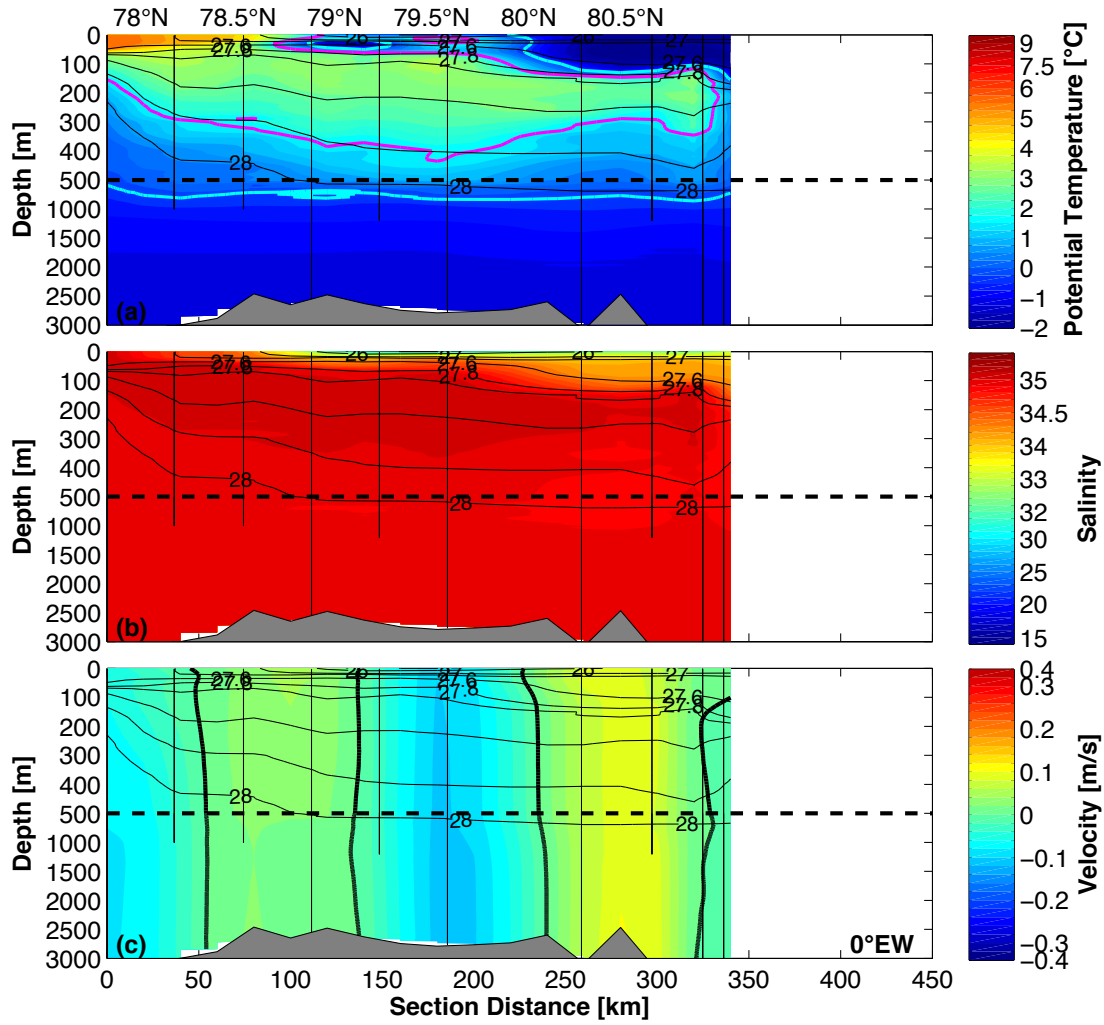
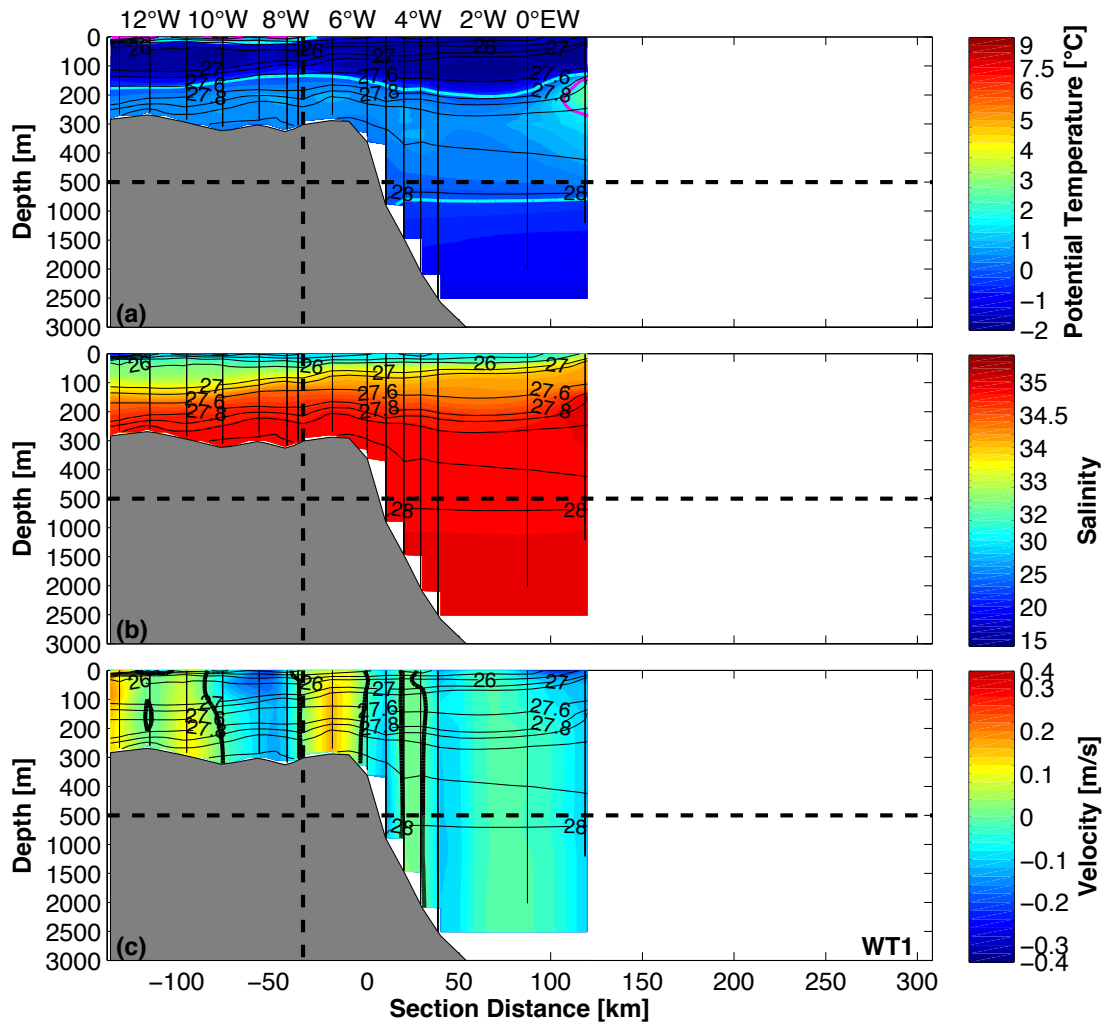**Figure 9:** As in Figure 8, but for section 0°EW. Positive velocities are westward, negative velocities are eastward.

warm water stretches the width of the section. North of 78.5°N (70 km) the temperature maximum is no longer at the surface but found between 100-150 m depth. The depth of the deep warm layer increases northward and the thickness of the layer warmer than 2°C decreases. Apart from a shallow lens of cold surface water at 79°N, the shallow 0°C isotherm first outcrops at 79.8°N sloping downward to over 100 m at the northern end of the section. The deep 0°C isotherm lies below 500 m depth along the entire section, marking the transition to deep waters. Lowest salinities are found in the upper 120 m at the northern end of the section and isohalines shoal toward the south (Figure 9 (b)). A salinity front is located between 79.5 and 80°N (200 and 250 km) where the 34.5 isohaline slopes upward by almost 80 m. South of this, the isohalines remain almost horizontal until they outcrop steeply around 78.5°N (75 km). The density field follows the salinity and temperature field north of 78.5°N and the temperature field to the south of this (thin contour lines in Figure 9 (a) and (b)). The 27.8 kg/m^3 isopycnal is deepest in the north with 150 m, shoals to ~70 m between 79.5 and 80°N and then stays virtually flat until the southern end of the section. A strong surface density gradient is found around 78.5°N where shallow isopycnals outcrop.

At 0° EW (Figure 9 (c)) the absolute geostrophic velocity field switches between broad sectors of weak eastward (around 78°N and 79.5°N) and westward velocity (around 78.5 to 79°N and around 80 to 80.5°N). Velocities reach $\pm$ 0.12 m/s. The velocity field is mostly barotropic and the sectors are ~80 km wide.

4.1.3   The Evolution of the EGC from North to South

In all sections described below a strong gradient can be observed at about 150 m for both temperature and salinity. At WT1 water with temperatures above 2°C is found only in the extreme east at 150-250 m depth where the section intersects with the 0°EW section (Figure 10 (a)). The deep 0°C isotherm is located below 750 m. The shallow 0°C isotherm is at its shallowest at 0°EW, dips to over 200 m depth at 3°W, shoals to about 150 m over the shelfbreak and subsequently dips to 200 m depth in the innermost trough. Inside the trough, between 7°and 13°W (-20 and -130 km) the surface water is warmer than 0°C. Salinity (Figure 10 (b)) increases strongly over the upper 150 m and the 35 isohaline lies, at ~150 m, well above the depth of the trough entrance. The 33.5 isohaline outcrops at 0°EW and slopes down to over 100 m in the inner trough. The isopycnals closely follow the salinity field with the 27.7 kg/m^3 isopycnal at 150 m in the east and at 200 m in the west (thin contour lines in Figure 10 (b)). Downward sloping of isopycnals toward the shelfbreak is absent of very weak (0.25 m/km for the

Figure 10: As in Figure 8, but for section WT1. The vertical dashed line shows where sections WT1 West and WT1 East meet. Positive velocities are NNE-ward in WT1 West and NNW-ward in WT1 East.
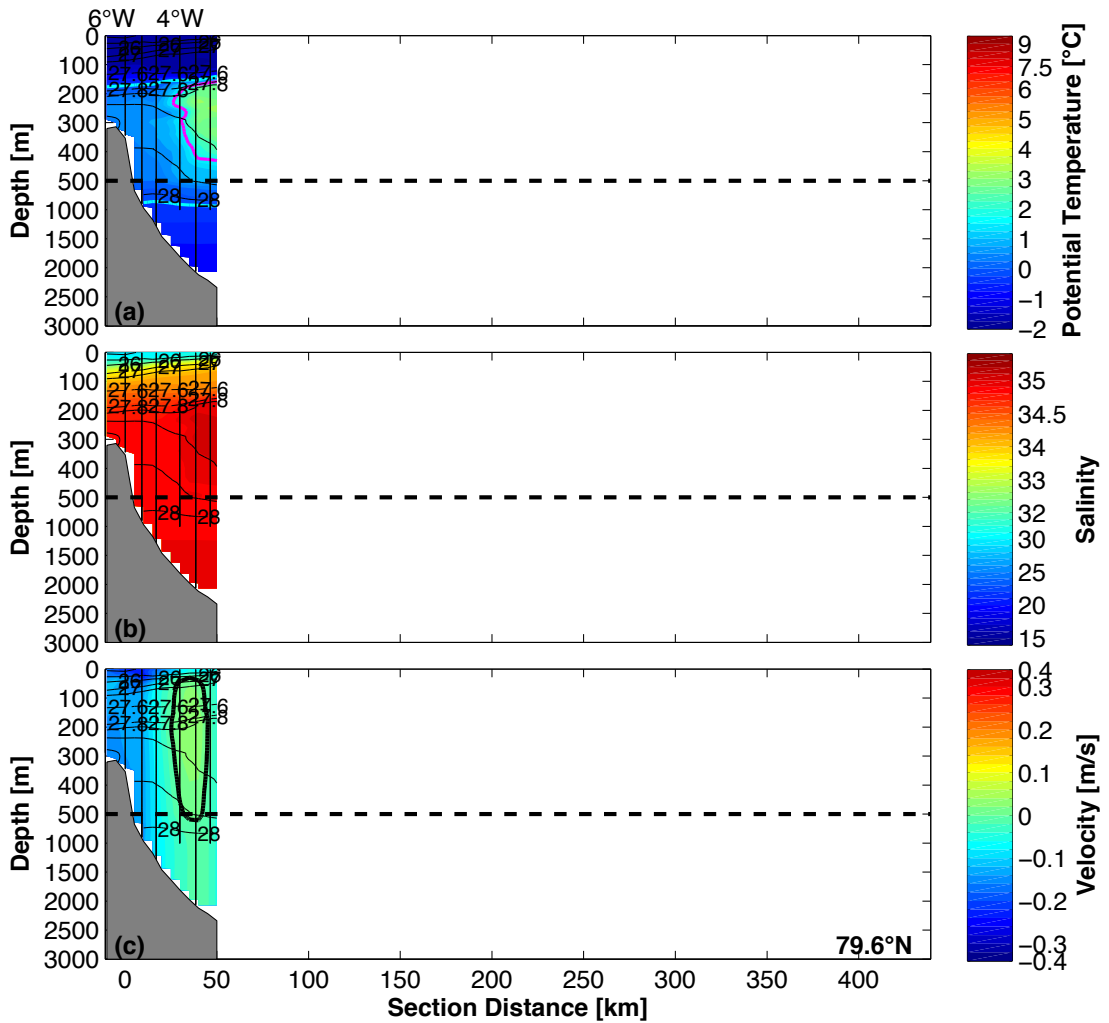
Figure 11: As in Figure 8, but for section 79.6°N.

27.8 kg/m^3 isopycnal).

Two regions of southward flow were sampled (Figure 10 (c)). One offshore of the shelf-break around 6°W (between 0 and 20 km) with core velocities of -0.09 m/s, the other between 5°W and 0°EW (30 km and 120 km). We identify the southward flow at the shelfbreak as the shelfbreak EGC. Both the southward flow at the shelfbreak and at the eastern end of the section are highly barotropic though some surface intensification is found around 1°W (100 km). In section 79.6N water warmer than 2°C is found in a core between 150 and 450 m depth east of 4.5°W (30 km) (Figure 11 (a)). The shallow 0°C isotherm lies at 150 m depth in the east and dips only slightly toward the shelfbreak. The deep 0°C isotherm lies just above 1000 m. Salinity (Figure 11 (b)) is lowest at the

surface close to the shelfbreak. The 34.5 isohaline lies between 150 and 200 m. The density field follows the salinity field with the exception of the 27.8 and 27.9 kg/m³ isopycnals which diverge offshore in the vicinity of the subsurface temperature maximum (thin contour lines in Figure 11 (a) and 11 (b)). The 27.7 kg/m³ isopycnal lies at ~150 m depth. The 27.8 kg/m³ isopycnal slopes toward the shelfbreak with a slope of 0.5 m/km.

Section 79.6° N (Figure 11 (c)) shows high southward velocities (~0.16 m/s), with a strong barotropic component, just offshore of the shelfbreak with some weak northward flow close to 4°W (40 km). The centre of the southward flow is at 6°W (5 km) and the eastern edge at 4.5°W (25 km). The section does not extend far enough onto the shelf to sample the western edge of the current (the shelfbreak EGC).

In the western half of section 79°N, the shallow 0°C isotherm outcrops at 2.5°W (~70 km) and dips to about 200 m depth on the east Greenland Shelf. No >0°C water is found shoreward of the East Greenland shelfbreak apart from a thin layer following the downward sloping bathymety west of 7.5°W (-50 km). Low salinity water (S<34.5) reaches down to 250 m on the shelf (Figure 8 (b)). This isohaline shoals toward the east until it reaches about 50 m depth at 2.5°W (70 km). As with the >0°C water, water with salinities higher than 34.5 is found shoreward of the shallowest bathymetry west of 7.5°W (-50 km) and occupies the deepest tens of meters closely following the bathymetry. Lowest densities are found in the surface layer on the shelf (thin contour lines in Figure 8 (b)). Whilst the isopycnals < 27.8 kg/m³ are almost flat above 100 m depth in the deep Fram Strait (between 2.5°W and 2.5°E), they deepen to the west of this and the 27.8 kg/m³ isopycnal reaches 200 m at the east Greenland shelfbreak (the slope is 0.75 m/km). A different pattern is seen in the 27.9 kg/m³ isopycnal which undulates strongly, following the temperature field and is generally shallower in the west than in the east.

In section 79°N (Figure 8 (c)) a sector of southerly velocities at the shelfbreak indicates the EGC. There are two cores of southward velocities, one surface intensified core east of 7.7°W (around -60 km) with velocities reaching -0.17 m/s, and a more barotropic core just offshore of the shelfbreak centred around 5°W (20 km) and reaching -0.15 m/s. We identify the southward current at the shelfbreak (between 0 and 40 km) as the shelfbreak EGC. At the southernmost section NT1 the deep 0°C isotherm is located between 750 and 1000 m (Figure 12 (a)). The shallow 0°C isotherm outcrops just offshore of the shelfbreak and dips steeply westward to 150 to 200 m depth. A shallow surface layer with temperatures above 0°C is located in the western most part of the section. Water with temperatures above 2°C is found in a broad core between 350 and 100 m immedi-
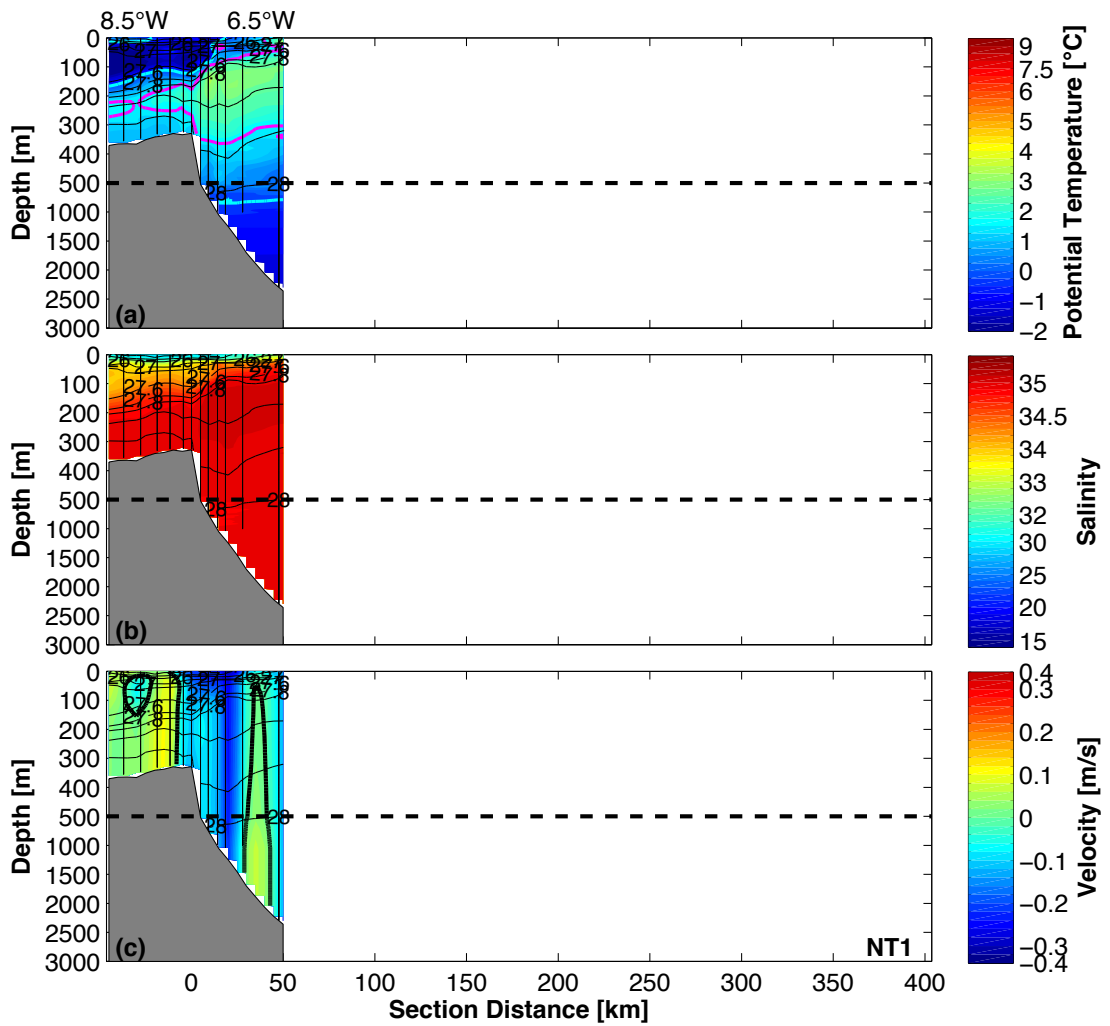
Figure 12: As in Figure 8, but for Section NT1. Positive velocities are northeastward, negative velocities are southwestward.

ately offshore of the shelfbreak and further to the east where the upper boundary shoals steeply before eventually outcropping at the easternmost station (at 6.5°W). Inside of the trough a thin layer of water warmer than 2°C is found between 200 and 250 m. Salinities (Figure 12 (b)) are lowest at the surface and shoreward of the shelfbreak. The 34.5 isohaline slopes downward from east (30 m) to west (150-200 m). The thickness of the surface layer with salinities below 34 remains around 30 m across the section. The density field follows the salinity field with the 27.7 kg/m^3 isopycnal at 50-100 m depth in the east and at 200 m depth in the west (Figure 12 (b)). The 27.8 kg/m^m isopycnal slopes toward the shelfbreak with a gradient of 1.66 m/km.

At NT1 (Figure 12 (c)) a northeastward flowing region lies west of the shelfbreak and a southwestward flowing region, with high velocities down to the seafloor, offshore of the shelfbreak. The core of this flow, which we identify as the shelfbreak EGC, is located around 7°W (at 20 km) and reaches -0.26 m/s. The current has a width of approximately 40 km (from -10 to 30 km) and shows some surface intensification in its western half whereas the eastern part is highly barotropic. At 6.5°W there is some indication of a second southward flow but the section does not extend far enough offshore to identify a possible current it in its entirety.

4.1.4   Error estimates

Error estimates for absolute geostrophic velocities are not shown. As expected the relative error from varying the search radius was mostly negligible or very small (<10 %). Changing the tension produced mostly small errors below 10 % with some areas of higher relative error where station spacing was higher than the average for that section. The only exception is the section at 79.6°N where relative errors rise to 40 %, in areas below 500 m and outside of what we define as the EGC. The largest errors were produced when the grid spacing was changed. The relative error is below 30 % in most areas but some very high values (over 50 %) occur in areas of uneven and large station spacing (the eastern sides of section WT1 and NT1). Large relative errors in section 79°N occur mainly below 500 m and are not within the boundary currents. The median absolute deviation of the VMADCP data was generally very low with maximum values of 0.012 m/s found in the shelfbreak EGC at 79°N. The deviation at other stations was on the order of 0.005 m/s. The maximum median absolute deviation of the LADCP velocities at NT1 was 0.007 m/s, the majority of deviations did not exceed 0.004 m/s.

4.1.5   Key Points

The key points from examining the hydrography and velocity fields along our sections are: The temperature maximum can be found at the surface in the south and east of Fram Strait where warm, salty AW enters near the Svalbard shelf. The water layer warmer than 2°C gets thinner and the shallow 2°C isotherm slopes downward toward the north and west. There is no water warmer than 2°C at 80.8°N and 0°EW (the northern end of section 0°EW) and inside of Westwind Trough. At the entrance to Westwind Trough isopycnals do not slope downward towards the shelfbreak, there is some sloping of isopycnals at 79.6°N and downward sloping isopycnals are clearly visible at the shelfbreak at 79°N and the entrance to Norske Trough. Flow through 0°EW at 79°N is westward. The hydrography sections do not allow easy investigation of the spreading and mixing of watermasses characterized by their potential temperature, salinity and density signature. Therefore, we now examine the watermass properties at each station within our sections.

4.2   Watermasses in Fram Strait

In the previous section we presented the temperature, salinity, density and absolute geostrophic velocity fields in Fram Strait. We will now take a closer look at the watermasses defined by these properties (Table 1). For this we will examine the potential temperature and salinity from each station (not gridded) in θ-S space. We show θ-S plots in which colour coding depends on the along section location of a station.

All θ-S diagrams (Figure 13–17) share the same general shape seen clearest in the θ-S diagram of section 79.6N (Figure 16). Surface water follows the freezing point line until some salinity, higher than 34, at which the temperature increases sharply to a (local) maximum, and then decreases again sharply toward the deep ocean. This shape is varied in cases where temperatures in the upper ocean are higher than the freezing point. The point at which the temperature starts increasing sharply with depth is called the 'knee' in older literature and sometimes identified as a distinct watermass, the 'knee water' (*Bourke et al.*, 1987; *Budéus et al.*, 1997). Atlantic Water (AW) is found in all sections though in the case of WT1 only at 0°EW, 120 km east of the shelfbreak. When following the path of the AW in Fram Strait, from the WSC at 79°N, crossing 0°EW as recirculating AW to the EGC along the Greenland shelfbreak, a deep temperature maximum colder than 2°C (Arctic Atlantic Water (AAW) lighter than 27.97 kg/m³) is first found in the northernmost cast of section 0°EW. Before that, in the southern part of the 0°EW section and the eastern part of the 79°N section, the deep temperature maximum is ei-
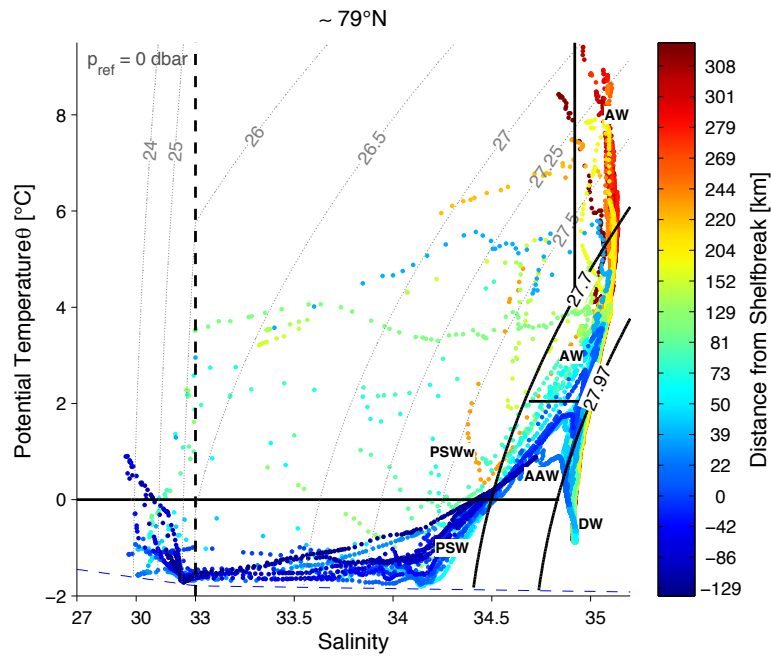
Figure 13: Potential temperature, salinity diagrams for Section 79°N. Individual casts are colour coded depending on their distance to the East Greenland shelfbreak. Please note that the x-axis changes scale at 33 (vertical dashed line). Thin gray contour lines show potential density referenced to 0 dbar. Solid black lines show watermass boundaries. Acronyms as in Table 1, boundaries for watermasses denser than 27.97 (deep water (DW)) are not shown. Watermass definitions after *Rudels et al.* (2005), compare Table 1.

ther warmer than 2°C (AW) or the temperature increases all the way to the surface (in the WSC, the easternmost part of section 79°N). A deep temperature maximum colder than 2°C is present in all WT1 casts west of 0°EW, in the four shoreward casts of 79.6N which lie within 17 km of the shelfbreak, in some of the casts in 79°N (though no further from the East Greenland shelfbreak than ~20 km), and is conspicuously absent in NT1 where the subsurface temperature maximum is above 2°C in all cases.

4.2.1   The AW Inflow and the WSC

The inflow region of AW into Fram Strait in section 79°N is characterized by high salinities throughout the entire water column, a temperature maximum at the surface and a temperature minimum, significantly above the freezing point, in the deep ocean. The surface temperatures (at 308 km) of over 9°C on the West Spitsbergen slope are the highest measured in our study. (Temperatures are higher than the freezing point throughout the watercolumn). AW reaches up to the surface east of 5°E (240 km). In the upper tens of meters it is often too warm to still fall into the density range of AW defined by *Rudels et al.* (2005). Since the water is part of the WSC and temperature stratified we expanded our definition to include water lighter than 27.7 kg/m^3 with salinities above 34.92 in our definition of AW. Towards the west, surface salinity decreases and the depth of the temperature maximum increases.

4.2.2   The Deep Fram Strait and the Westward Recirculation

Section 0°EW shows a south to north transition. At the southern most station the water has an almost uniform salinity with high temperatures at the surface and low temperatures at depth, similar to the station sampled in the WSC along 79°N. Further to the north, stations show a subsurface temperature maximum at densities between 27.7 and 27.97 kg/m^3 that gets colder and fresher with increasing latitude. This (local) maximum is located at depths between 50 and ~220 m and its depth increases northward. Close to the surface, the water is generally fresher than at depth. The middle stations show near surface warming whereas the temperature at the northern stations is close to the freezing point. AW is found at all stations except the northern most at 80.8°N, were only AAW is found. The depth at which AW is found increases from the south where it lies at the surface, to a core depth of about 200 m in the north.
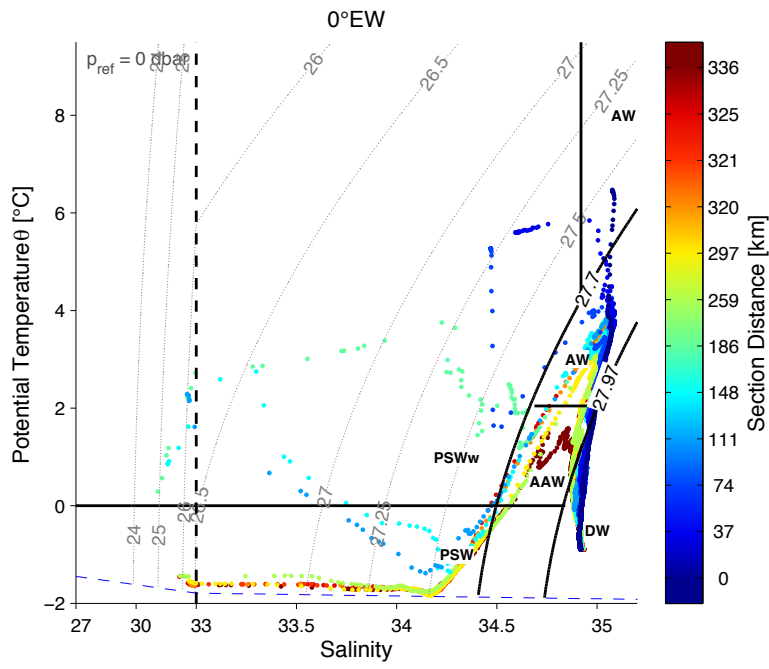
Figure 14: As in Figure 13 but for section 0°EW.
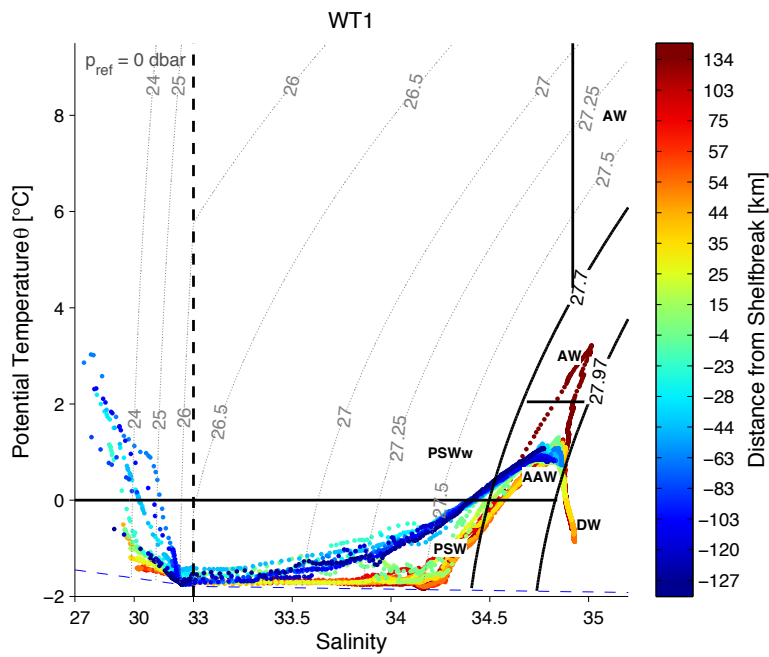
Figure 15: As in Figure 13 but for section WT1.
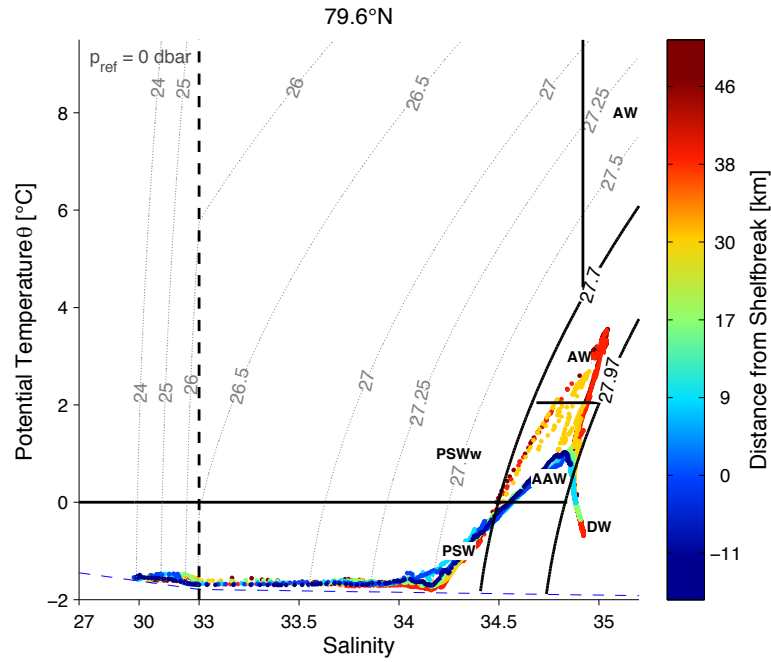
Figure 16: As in Figure 13 but for section 79.6°N.

4.2.3   The Evolution of the EGC from North to South

At the mouth of Westwind Trough (section WT1) the deep temperature maximum is much lower than at the eastern most station (0°EW). Towards the west the salinity at which the temperature approaches the freezing point gets lower. At the same time the surface salinities decrease and the surface temperatures increase. The surface salinity measured at the western most station of WT1 is the lowest of our study. The only AW found in this section is from the station shared with the 0°EW section which lies over 130 km to the east of the shelfbreak.

Further to the south at section 79.6°N surface temperatures are close to the freezing point for all stations. There is little variation in the θ-S properties of the knee between stations. The temperature of the deep temperature maximum is higher for stations further to the east though there is no clear trend in the depth at which this maximum occurs. No AW is found shoreward of 30 km off the shelfbreak, offshore of 30 km AW was found below 200 m depth.

At 79°N the depth of the temperature maximum reaches 200-300 m (or the sea floor) at the western most stations. The AW core is found at ~200 m depth near the East Greenland shelfbreak, no AW is found on the East Greenland shelf at 79°N (outside of the troughs). At the stations close to and on the east Greenland shelf the temperature
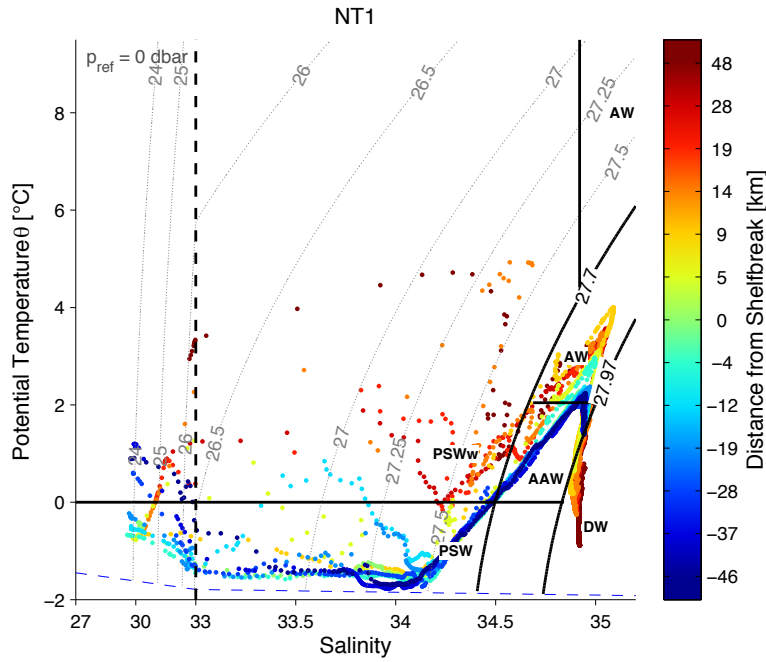
Figure 17: As in Figure 13 but for section NT1.

minimum is reached at salinities lower than 33, as already seen in the on-shelf stations at WT1. Only the stations in the western deep Fram Strait (around 2.5°W, 70 km east of the East Greenland shelfbreak) have a deep temperature minimum close to the freezing point at salinities greater than 34.

At section NT1, at the mouth of Norske Though, the temperature of the deep temperature maximum decreases from east to west. The eastern stations have a secondary temperature maximum, shallower than the clearly defined peak at densities greater than 27.7 kg/m³. The temperature of this shallow near surface temperature maximum also decreases toward the west. Conversely, the surface temperature decreases westward only up to the middle of the section before increasing again shoreward of the shelfbreak. The stations shoreward of the shelfbreak are also the only stations to show a deep temperature minimum close to the freezing point in this section. The salinities at this deep minimum are very similar, though not as close together as the salinities of the temperature minimum at 79.6°N. AW is found at all stations in this section, although the layer is very thin (~50 m) and located at ~250 m at the western 3-4 stations in Norske Trough. To the east the AW core gets thicker, warmer and shallower. At the shelfbreak it is located at ~200 m depth and about 50 km seaward of the shelfbreak, it is located at 100-150 m.

4.2.4   Key Points

Important aspects of the θ-S plots are: The almost uniform salinity and temperature stratification with very warm AW in the east of section 79°N (the AW inflow in the WSC), the absence of AW at the northern most station of 0°EW and at WT1, the absence of knee-water on the shelf at WT1 and 79°N and the absence of AAW at NT1. In the following section we will take a closer look at the mixing of watermasses and associated changes in properties at the deep temperature-salinity maximum.

4.3   The Deep θ-S Maximum and Mixing of Watermasses

The watermasses forming part of the deep maximum, described in the previous section, can be seen in Figure 7. When examining the deep maximum properties and endmember mixing triangles in T-S space we see that the two mixing triangles are well able to represent the watermasses involved in the maxima. Most points lie near the mixing line between AAW and AW (dashed line in Figure 7). Points that do not lie within the triangle are located in the east of section 79°N and in the south of section 0°EW, the location of the AW inflow to Fram Strait and the WSC. Here the water is warmer than the AW endmember used for our calculations (Table 2). See Section 3.3 on how the endmembers used here were defined. Other stations that do not fall within our mixing triangles are very close to it. Since section 79°N spans both the AW inflow in the WSC and the AAW outflow in the EGC this section has the most spread. Near the WSC, in the eastern part of the section, water is warmer than the AW endmember whilst in the EGC and on the east Greenland shelf the water has large AAW and PSW fractions. Water at the deep maximum in section 0°EW is clustered around the AW endmember, with only the northernmost station closer to the AAW endmember. At WT1 T-S properties are clustered around the AAW endmember with some PSW and DW fractions, the station shared with 0°EW is closer to AW. At 79.6°N deep maximum properties are distributed along the entire mixing line between AAW and AW, with clusters at the respective endmembers and only very small fractions of other watermasses. At NT1 points are clustered in the centre of the mixing line between AAW and AW with the eastern stations closer toward AW.

Properties (potential temperature, depth, salinity, density, oxygen concentration and AW fraction) of the deep temperature-salinity maximum at each station are shown for each section in Figure 18 to 22. These properties can distinguish the watermasses by their temperature and salinity. They provide an indication for the age of the water (the oxygen saturation in old watermasses—which have not been in contact with the atmo-
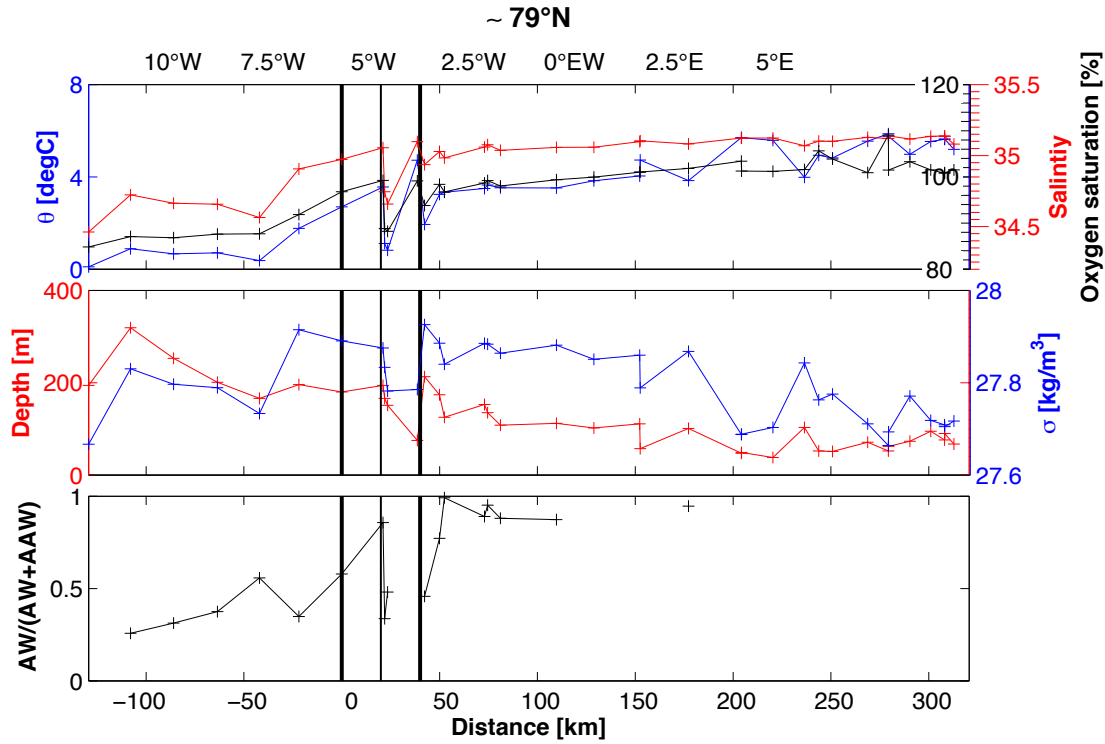
Figure 18: Properties of the deep temperature-salinity maximum at 79°N. The definition of the depth of the deep temperature-salinity maximum is given in Section 3.3. The thin vertical black line denotes the core of the shelfbreak EGC, bold black lines show the boundaries of the shelfbreak EGC (for definition see Section 3). The upper panel shows potential temperature, salinity and oxygen saturation, the middle panel shows depth of and potential density and the lower panel displays AW fraction relative to AAW.

sphere for a long time—is lower than in new watermasses). From the depth of the deep temperature maximum we can see if it subducts under shallower watermasses and finally, the mixing ratio of AW to AAW shows how much of the two watermass endmembers we expect to form the deep maximum is actually present. In general, potential temperature, salinity, oxygen saturation, and AW fraction are correlated, whereas depth and density are anticorrelated to the former. Values for PSW and DW fractions are given in the text, though not included in the figures. By definition the fraction of either PSW or DW is 0 at each cast.

4.3.1 The AW Inflow and the WSC

The largest spread in properties of the deep maximum is seen in the section crossing Fram Strait at ~79°N (Figure 18). This is not surprising as the section crosses both the

39
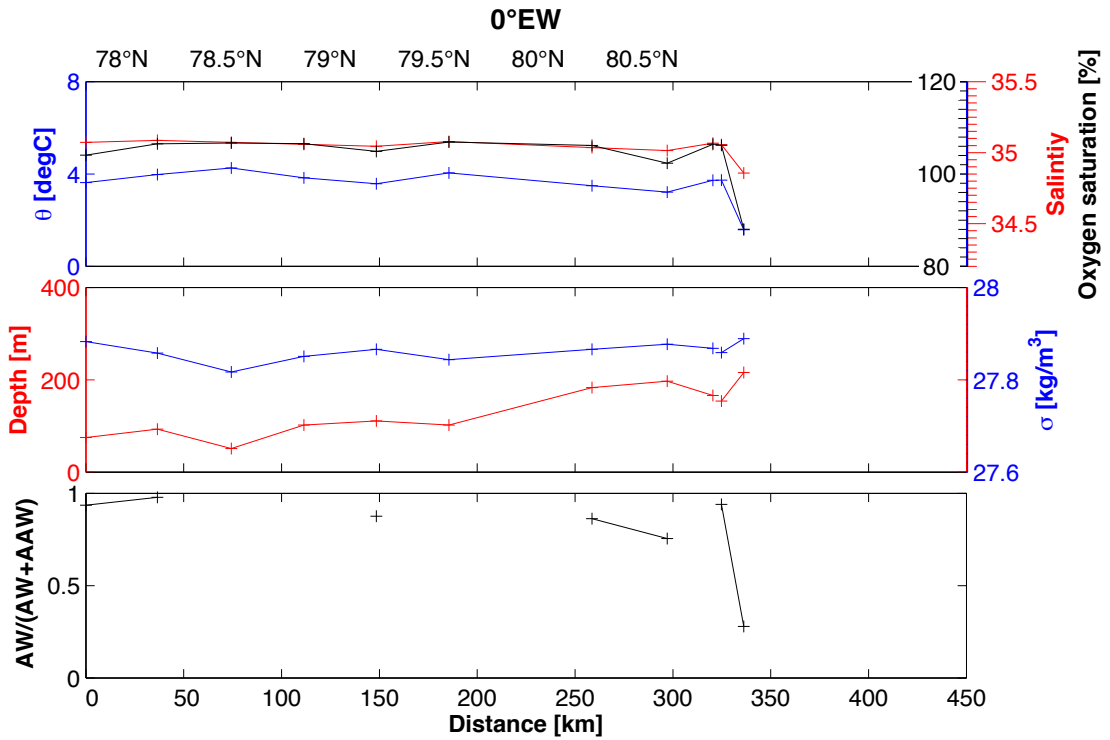
Figure 19: As in Figure 18 but for section 0°EW.

EGC and the WSC.

As expected temperature, salinity and oxygen concentration are higher in the east (toward the WSC) and the deep temperature-salinity maximum is shallower. In the WSC itself the deep temperature maximum disappears and the water is completely temperature stratified with the highest temperatures at the surface (see Figure 13). The depth shown here is that of the shallow salinity maximum (see Section 3.3 for the criteria used to pick the deep maximum). This maximum lies between 40 and 110 m east of 0°EW (150 km). The density of the deep maximum is highest in the deep Fram Strait.

AW fractions in the south-east of Fram Strait, seen in the eastern part of section 79°N, are very high as this is where AW enters Fram Strait from the south via the WSC. Those stations in the eastern part of section 79°N that could be described with our choice of mixing triangle, show a high AW fraction (>80 %), around 10-20 % of AAW and very small fractions of other watermasses. At stations where no value is displayed for the watermass fractions the water was warmer than the AW endmember and thus outside of the mixing triangle, though within our definition of the AW watermass.
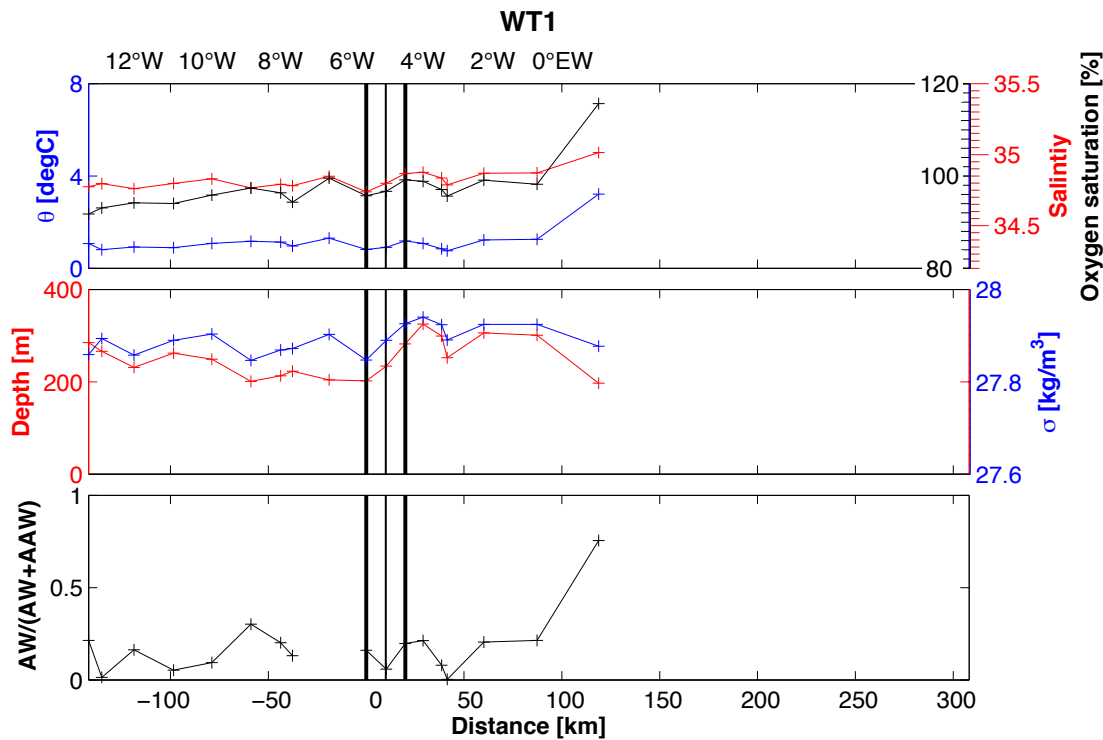
Figure 20: As in Figure 18 but for section WT1.

4.3.2 The Deep Fram Strait and the Westward Recirculation

There is no clear trend in the properties of the deep temperature maximum along 0°EW (Figure 19) with the exception of depth which increases northward as expected. Interestingly, there is no northward decrease in temperature with the exception of the northern most station, which contains >75 % AAW. Here temperature, salinity and oxygen concentration decrease sharply while the depth and density of the deep maximum increase. At 0°EW (bottom panel in Figure 19) the deep maximum contained a high fraction of AW at all stations except for the northern most station where the AW fraction decreases sharply from >90 % to <30 %. AAW behaves in the opposite fashion, increasing sharply from ~10 % to ~70 %. Fractions of DW and PSW (not shown) are very low.

4.3.3 The Evolution of the EGC from North to South

At WT1 (Figure 20) no clear trends can be observed, especially density varies strongly along the section. In the vicinity of the EGC, salinity, depth and density appear to increase eastward, which in the case of depth is contrary to what we see in the EGC further to the south. Between the two eastern most stations, at 0°EW, temperature,
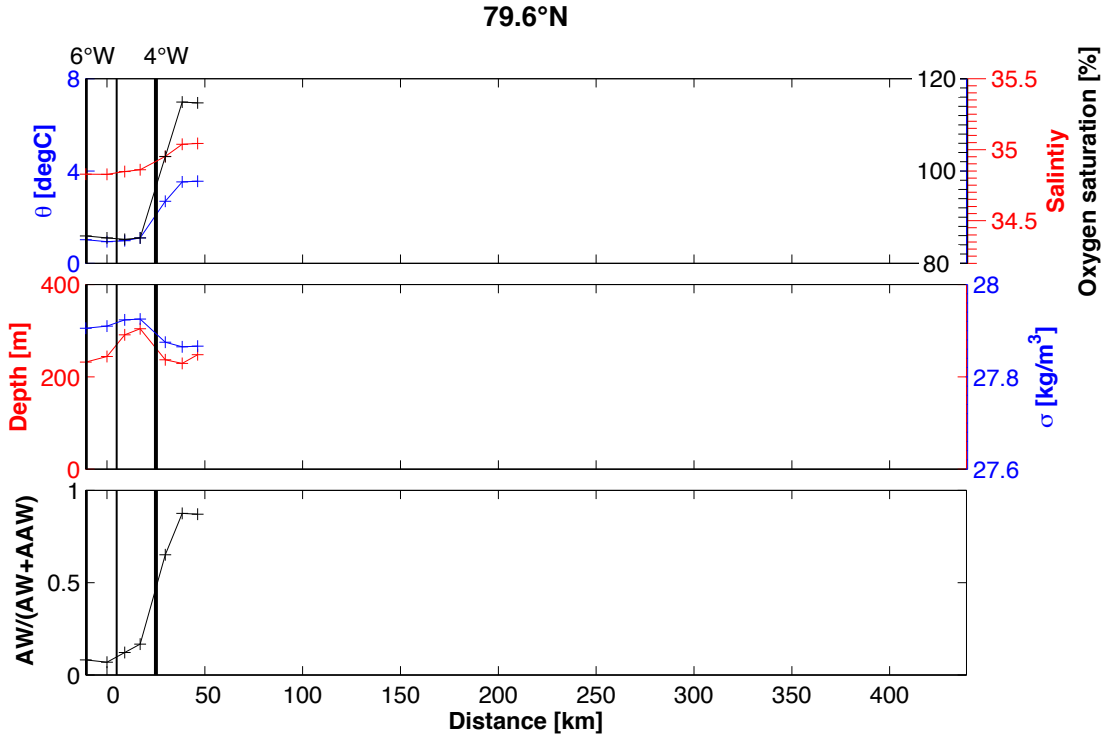
Figure 21: As in Figure 18 but for section 79.6°N.

salinity and oxygen concentration increases eastward whilst depth and density decrease. This can be identified as the signal of AW found at this station but not at any other in WT1.

Inside Westwind Trough AAW fractions are high (~60 to >90 %; bottom panel in Figure 20). PSW and AW make up less then 20-30 % each. The DW fraction in the trough is 0 and rises to 20 % offshore of the shelfbreak. AW reaches ~80 % only at the eastern most station (at 0°EW). WT1 has the second highest fraction of PSW (20 %) for deep maxima measured in any section, only some deep maxima on the shelf at 79°N have higher PSW fractions.

In our sections south of WT1 the depth of the deep maximum did not increase eastward crossing the EGC. Section 79.6°N (Figure 21) shows the clearest signal of all investigated sections. East of the eastern EGC boundary, AW is prominently present, while to the west, almost pure (>90 %) AAW is found. The other properties follow this characteristic.

At 79°N, the west to east gradient is strong in all properties. Density is not anticorrelated to temperature, forming an exception from the other sections. At 79°N density is highest to the east of the EGC and decreases toward both the Greenland and Svalbard
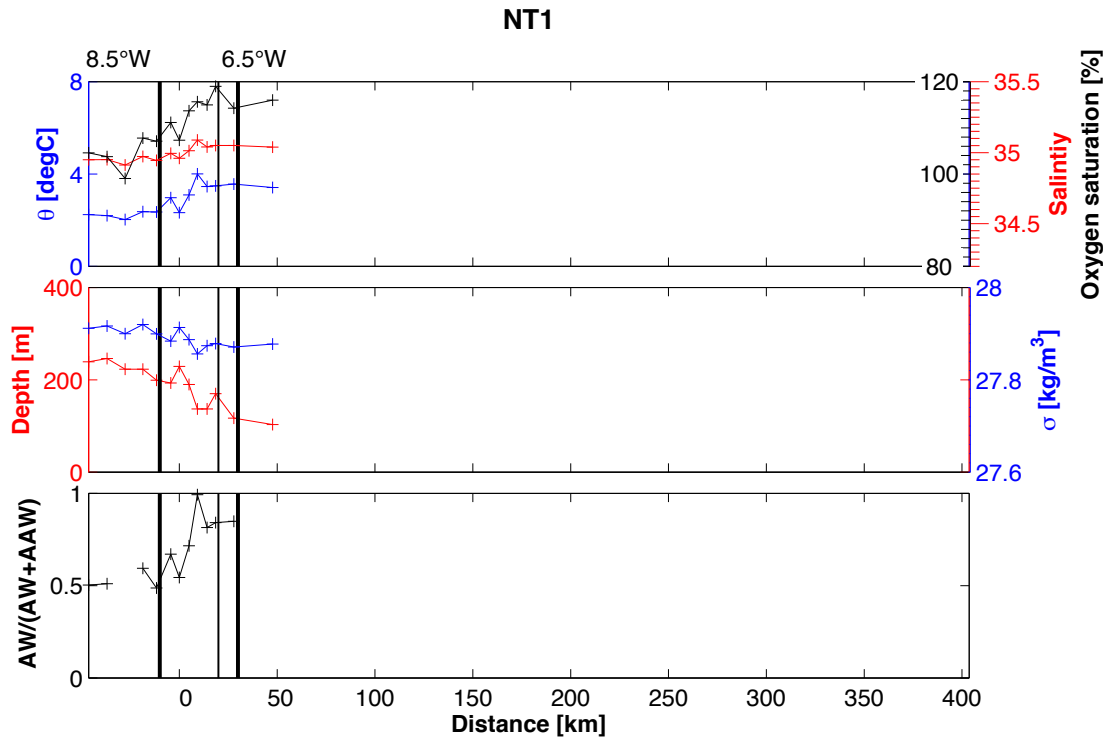
Figure 22: As in Figure 18 but for section NT1.

coast. Strong excursions in all properties can be seen between the centre of the EGC and 50 km, close to its eastern boundary. The excursions, positive and negative, correlate with each other except for depth and density which are anti-correlated. Between -50 and 50 km (which includes the location of the EGC) all properties increase except for depth which decreases.

On the East Greenland shelf at 79°N high fractions of PSW and AAW are found (20 to >60 % for AAW, 20 to 50 % for PSW). DW fractions are generally very low (<15 %). At the shelfbreak the AW fraction increases sharply, then shows strong variation in the next 50 km before staying at high values of over 80 %. The AAW fraction shows the same behaviour in the opposite direction.

The properties of the deep maximum show little variation along NT1 (Figure 22) compared with 79.6°N and 79°N. Temperature, salinity and oxygen concentration increase eastward, the other two properties decrease. The gradient is located in the EGC and the values show sharp excursions within the EGC.

At Norske Trough (bottom panel in Figure 22) the fractions of AAW and AW are almost equal at 50 % inside the trough. Offshore of the shelfbreak the AW fraction increases from west to east to over 80 %, as the AAW fraction decreases to under 20 %. Fractions
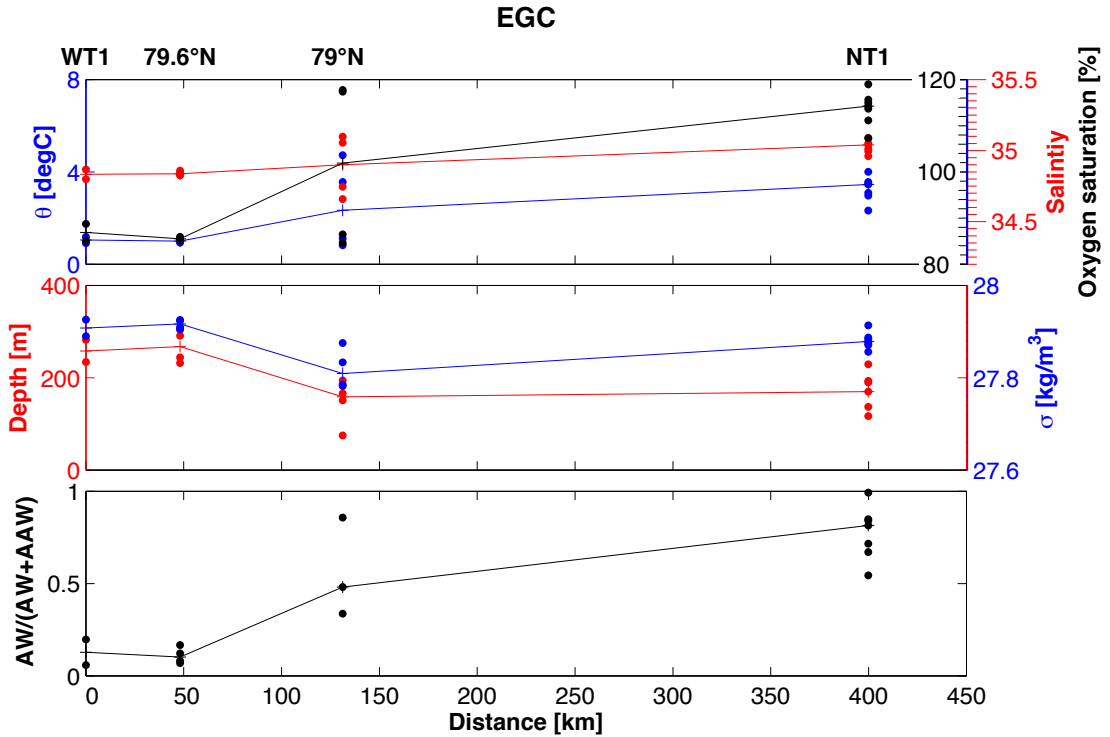
Figure 23: Properties of the deep temperature-salinity maximum in the shelfbreak EGC from north to south, criteria are the same as in Figure 18–22. See Section 3 for the criteria employed for choosing the deep maximum and the width of the shelfbreak EGC. Coloured points show the individual measurements within the EGC, lines the median.

of DW and PSW are very low (below 10 %).

4.4   Properties of the EGC from North to South

When examining the deep maximum in the EGC from north (WT1) to south (NT1, Figure 23) temperature, salinity and oxygen concentration increases, depth decreases and density shows a minimum at 79°N with the value at NT1 lower than at the two northern sections. The section at 79°N also stands out as having the highest spread of values for all examined properties.

4.4.1   Transport in the EGC

The southward transport of the shelfbreak EGC varies between 0.9 Sv at WT1 and 4.0 Sv at NT1 and generally increases downstream (Figure 24). The exception is 79°N where
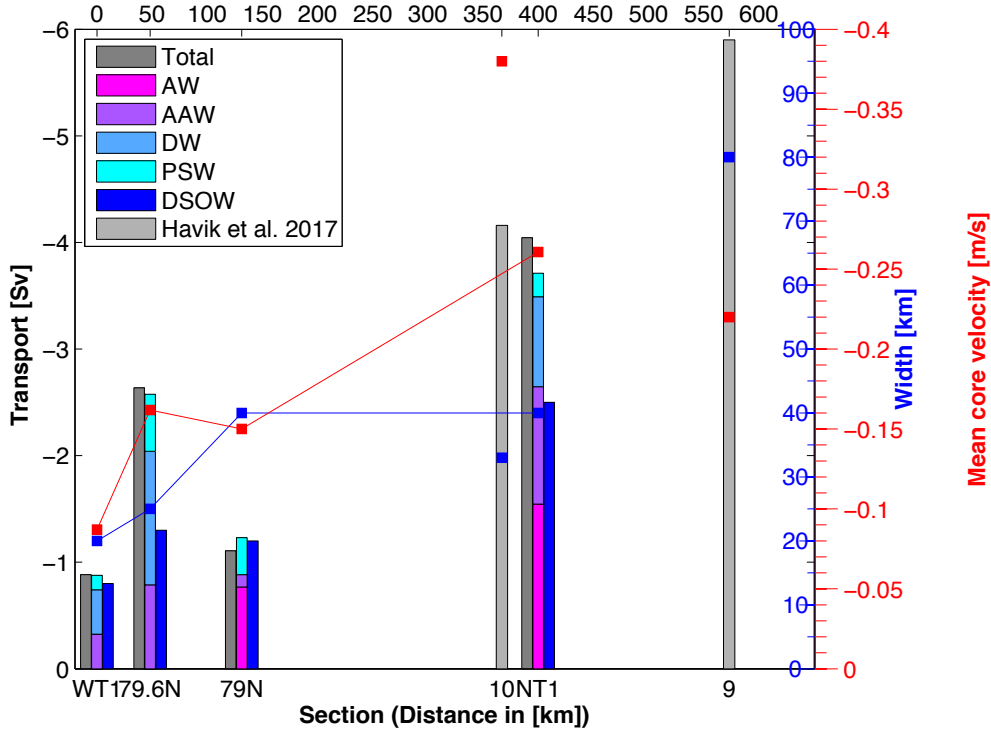
Figure 24: Transport, velocity and width of the shelfbreak EGC in Fram Strait as defined in *Håvik et al.* (2017). Transport is in Sv ($10^6 m^3$/s; southward transport is negative), velocity is the maximum of the depth-mean southward velocity in the upper 150 m within the shelfbreak EGC (the EGC edges are at the points where the depth-mean velocity over the upper 150 m of the water column has decreased to 20% of the maximum value). DW is water denser than 27.97 kg/m³ (AW(/), AAW(\), AIW, uPDW and NDW in Table 1). DSOW is all water above 800 m that is denser than 27.8 kg/m³. Downstream distance (in km) is 0 at WT1 and follows the East Greenland shelfbreak southward. Values for Section 9 and 10 of *Håvik et al.* (2017) are taken from their paper.

the shelfbreak EGC transports over 1.5 Sv less than at 79.6°N. This value may be even higher as we did not sample the western edge of the shelfbreak EGC in section 79.6°N. In general all values presented are minimum estimates and synoptic measurements, which therefore do not need to obey volume conservation. The width of the shelfbreak EGC increases downstream from 20 km at WT1 to 40 km at NT1. Mean southward core velocity also increases from -0.08 m/s at WT1 to -0.26 m/s at NT1, again section 79°N forms an exception with a decrease in velocity between 79.6°N and 79°N. The EGC at WT1 and 79.6°N transports no AW, DSOW transport increases from -0.8 Sv at WT1 to -2.5 Sv at NT1.

4.4.2   Key Points

The northern most station at 0°EW and the eastern most station at WT1 are very different from the other stations sampled in those sections. Crossing the EGC there are strong variations in all properties of the deep maximum and in watermass fractions. AW fractions at WT1 are very low and increase downstream along the EGC. At 79.6°N there is a very steep gradient and large difference between watermasses to the east and west of the EGC, this difference gets smaller further downstream i.e. at 79°N and NT1. With the exception of 79°N, the transport, mean core velocity and width of the EGC increases from north to south. Transport of AW at 79°N makes up a higher fraction of the total EGC transport at 79°N than at AW transport does to the total EGC transport at NT1.

4.5   Net Transport Through Fram Strait

Net cross-sectional transports were calculated for 0°EW and 79°N but due to the synoptic nature of the data these transports are not interpretable. The same is true for east/west and north/south transports in section 0°EW and 79°N respectively.
Northward transport in the WSC at 79°N was only 0.2 Sv and thus much lower than transports reported from previous combined CTD/ADCP studies (*Osinski et al.*, 2003). Net and southward transport was calculated for 0°EW to 6°W along 79°N and resulted in northward net transport and a southward transport of 2.4 Sv. Transport in the PSW jet was 1.1 Sv toward the south, with boundaries of the current chosen by the same method as for the EGC.

5   Discussion

5.1   Watermasses

In the following we will discuss the hydrography in Fram Strait. We will follow AW around Fram Strait and examine its modification. Next, we will discuss the presence and absence of a 'knee' in θ-S casts on the East Greenland shelf before looking at the implications of oxygen saturation. We will start however, with the more general feature of the temperature and salinity gradient at 150 m depth found in northwestern Fram Strait.
The strong gradient in watermass properties in the upper 150 m found in most sections is the halocline, described by other authors for the Arctic Mediterranean (e.g. *Rudels*

et al. (2005)). It is formed by heat loss of the upper water column to the atmosphere and to ice-melt, and by freshening through ice-melt and surface runoff (*Rudels et al.*, 1996). The halocline is then located between the fresher, colder surface mixed layer and the warmer, saltier intermediate layers of Atlantic origin. It thus acts as an important barrier between the warm Atlantic Water inflow below and surface processes such as sea-ice formation in the Arctic Ocean by inhibiting mixing and upward heat transport from the Atlantic Layer to the surface (*Rudels et al.*, 1996). However, warming of the Atlantic Water layer in the Arctic Ocean seems to have an increasing effect on sea-ice formation and distribution (*Polyakov et al.*, 2010), with a possible positive feedback between sea-ice loss and Atlantic Water impact on sea-ice (*Ivanov et al.*, 2016).

The watermass definitions used in this thesis are chosen to be able to capture the situation in Fram Strait as it was in summer 2016 and both our AW watermass definition as well as the endmembers chosen for mixing calculations lie within a θ-S range frequently identified by previous studies in our area as AW (Figure 6). Extending the AW definition of *Rudels et al.* (2005) to include water lighter than 27.7 kg/m³ was necessary due to the unusually high surface water temperatures in southeastern Fram Strait, the region of AW inflow. The θ-S diagram in Figure 13 shows quite plainly that water on both sides of the 27.7 kg/m³ isopycnal belongs to a single watermass in eastern Fram Strait. Here, the entire water column is temperature stratified with a temperature maximum at the surface of the water column. The salinity of this water is almost uniform with depth. We included water with salinities higher than 34.92 and densities lower than 27.7 kg/m³ in our watermass definition following *Walczowski et al.* (2017). This salinity boundary is high enough not to include watermasses obviously influenced by fresher PSW and low enough to ensure that the salinity of every deep θ-S maximum from any cast included in this study is higher than the boundary.

In the east of section 79°N AW is still in contact with the atmosphere. This is seen most plainly in the θ-S diagram for that section (Figure 13). In eastern Fram Strait the watercolumn is temperature stratified to the surface, with only negligible salinity variations. Surface salinities low enough to make the uppermost meters of the watercolumn lie in the PSW domain are only seen in the very east of section 79°N. This station is closest to the Svalbard coast and the surface water here is likely influenced by lateral mixing with shelf waters freshened by runoff and/or icemelt (*Saloranta and Haugan*, 2004). The monthly mean climatology in the WSC in 75 m depth from 1997–2012 has been determined from moorings (*von Appen et al.*, 2016). Our salinity falls within the range reported, the same is true for our temperatures when examining the entire spread from all 6 moorings and over the months of July and August. Our values may however

be outside of the climatology due to synoptic variability. The surface temperatures observed in the WSC at 79°N of ∼9°C (Figure 13) are the highest reported so far. This may be a signal of the warming AW inflow to Fram Strait (*Beszczynska-Möller et al.*, 2012; *Walczowski et al.*, 2017). In summer 2000 maximum temperatures of 9°C in the WSC were recorded south of 70°N with maximum temperatures at the entrance to Fram Strait merely reaching 6°C (*Piechura et al.*, 2001). The high temperature of AW in the southeastern Fram Strait also explains why we could not calculate a watermass mixing ratio for the deep temperature-salinity maximum at some stations along 79°N and 0°EW with our choice of watermass endmembers. The watermass properties lay outside of our mixing triangle (see Figure 7).

If we follow the path of AW around Fram Strait, AW is seen to subduct under colder and fresher surface water toward the north and west (Figure 8 (a) and 9 (a)). This was also simulated in the eddy resolving model study of Fram Strait by *Hattermann et al.* (2016) and attributed to eddies helping to subduct AW under PSW and sea-ice.

Section 0°EW reaches far enough northward to capture the northern extent of the (now subsurface) AW propagation in this summer 2016 synoptic realization. Section WT1 west of 0°EW consists of the on, near and far shelf waters uninfluenced by directly recirculating AW (AW warmer than 2°C). This is also indicated by the near 0 % contribution of the AW endmember to the water at WT1 calculated from the watermass triangles described above (Section 3.3). The absence of AW in all but the eastern most station at WT1 agrees with *Rudels et al.* (2005); *Nilsson et al.* (2008) who report AW only at the 0°EW intersect of their zonal section along 81°20'N sampled in May 2002. The properties of the deep water maximum sampled at WT1 agree with those stations sampled between 82–83°N and 10–5°W in 2004 (*Rudels et al.*, 2012) and the baroclinic geostrophic transport at this latitude was southward with 5.1 Sv (*Marnela et al.*, 2008). This would indicate that the AAW sampled at WT1 may be advected from the northwest along the east Greenland shelfbreak and possibly originates at least in part in the Canada Basin (*Rudels et al.*, 2012). The AW fractions larger than 0 % calculated from the mixing triangle for the inner trough at WT1 may be an expression of warm PSW found within the trough and not of AW since salinities are generally too low to fall near the AW definition and we saw in the hydrography section of WT1 (Figure 10) that no AW enters the trough. The three sections crossing the EGC downstream of WT1 show different stages of watermass transformation in the deep temperature maximum; from AAW and AW located horizontally next to another to successively greater mixing between the two until the deep temperature maximum is warmer than 2°C (and thus falls into the AW definition) at all stations sampled in section NT1. The points dis-

cussed above—AW in contact with the atmosphere in the eastern part of section 79°N, the subduction of AW toward the northwest, the absence of AW at the northern most station of 0°EW and at WT1 and its gradual mixing with AAW in the EGC from north to south—make us confident that the pathway of AW in Fram Strait was well captured in our sections.

The deep temperature maximum lies above 2°C and inside the AW definition at all stations sampled along section NT1 (see previous paragraph). This means that AW is found inside Norske Trough. The AW layer warmer than 2°C lies between 300 and 200 m depth inside Norske Trough (the solid magenta line in Figure 12) and thus above the depth of the shallowest sill (320 m) (*Schaffer et al.*, 2017). The depths of the deep temperature maximum, of the 1°C isotherm and of the 0.5°C isotherm all agree with the respective depths shown in the climatology presented in *Schaffer et al.* (2017). We can thus conclude that our synoptic section at NT1 is representative of the average situation in Norske Trough and that AW is able to reach the terminus of 79NG by this pathway. The absence of AW inside of Westwind Trough is also corroborated by the climatology presented in *Schaffer et al.* (2017) and we may conclude that at present the only direct pathway for AW to the glacier terminus is via Norske Trough. This has important implications both for the submarine meltrate at 79NG as well as for the trough and shelf circulation. AW reaching the glacier cavity is modified by ice melt and runoff to form a colder, fresher and less dense watermass that exits the glacier cavity at shallow depths (*Wilson and Straneo*, 2015). The precise pathways of deep transport in the troughs and of shallow transport in the troughs and on the shelf are still under discussion (e.g. *Topp and Johnson*, 1997; *Budéus et al.*, 1997; *Wilson and Straneo*, 2015; *Schaffer et al.*, 2017).

There has been some discussion in the literature about the origin of Knee Water (KW) (e.g. *Bourke et al.* (1987); *Budéus and Schneider* (1995); *Falck* (2001)). The most widely accepted scenario is that this watermass is advected from the Arctic Ocean (*Bourke et al.*, 1987; *Budéus et al.*, 1997) and is modified water of Atlantic origin (*Falck*, 2001). It is most likely formed north of Svalbard where the northward flowing AW encounters sea-ice and is cooled to the freezing point and freshened to a distinct salinity by melting sea-ice and heat loss to the atmosphere (*Moore and Wallace*, 1988; *Rudels et al.*, 2005). The Arctic origin of KW is somewhat supported in our data by the presence of KW in the north of section 0°EW and the absence of KW in the south-east of Fram Strait where waters are of Atlantic origin. The lack of a 'knee' on the shelf at WT1 and at 79°N can have a number of causes. The hypothesis that KW may be located too deep in the watercolumn to propagate onto the shelf (*Budéus and Schneider*, 1995) does not apply in our case as KW is found above 100 m depth and thus above the bathymetry of the

shelf regions at WT1 and 79°N. The knee may be mixed away on the shelf. *Topp and Johnson* (1997) identified a watermass which they termed Modified Knee Water. It is formed by mixing PW, AIW (defined as water between 0 and 3°C and with salinities between 34.5 and 34.9, which is roughly equivalent to our AAW) and KW offshore of the shelf and subsequent advection of the resulting watermass onto the shelf. This implies that these three watermasses are close together spatially somewhere offshore. We do not see profiles without the knee offshore of the shelfbreak at WT1, but do see a more gradual transition from 'knee' to 'no knee' at the shelfbreak at 79°N. It is not possible to decide from the available data alone whether the knee is eroded by mixing offshore of the shelfbreak with the resulting watermass then being advected onto the shelf.

Another possibility by which the knee may be eroded is mixing with coastal watermasses present on the shelf. For instance watermasses modified by glacial runoff or watermasses which had been in direct contact with a glacier or floating ice tongue may have caused the erosion. The 'non-knee water' would then originate in the inner troughs and not at the shelfbreak. Close to the 79NG terminus, glacially modified water is found at the same density level as KW allowing lateral mixing between the two watermasses to take place (*J. Schaffer*, pers. comm. 2017). If the shelf circulation is anti-cyclonic (as suggested by e.g. *Bourke et al.* (1987); *Budéus and Schneider* (1995); *Johnson and Niebauer* (1995); *Topp and Johnson* (1997)), then lateral mixing of glacially modified water with KW could explain the absence of KW in Westwind Trough and its presence in Norske Trough. This 'non-knee water' signature could then be transported south to 79°N by the southward jet found on the shelf at WT1 and 79°N and by the shelfbreak EGC (see Figure 8 (c) and Figure 10 (c)). Further lateral mixing on the transit south could then explain the more gradual transition from 'no-knee' to 'knee' at 79°N. It can however not explain the lack of 'non-knee water' at 79.6°N and at NT1. An explanation of the lack of non-knee water at 79.6°N may be that this section did not extend far enough onto the shelf to encounter non-knee water, this could be tested by extending the section further west should it be repeated. The lack of non-knee water at NT1 may be caused by stronger mixing. Non-knee water may have been, similar to AAW, mixed in with the ambient watermasses and may thus not be visible in the θ-S plot examined here.

A correct representation of Greenland runoff, both precipitation and glacier discharge, may be crucial to represent the Northeast Greenland shelf circulation correctly in a numerical model. This would likely have effects both on the surface circulation on the shelf as well as the circulation in Westwind and Norske Troughs and the PSW transport and AW modification in the EGC.

5.1.1   Oxygen Saturation

We saw in our analysis of the deep θ-S maximum in Section 4.3 that the oxygen saturation of AAW, which has transited the Arctic Ocean, is lower than that of directly recirculating AW. Oxygen saturation is dependant on a number of physical and biological processes such as temperature, salinity, sea-ice formation, air-sea interaction, photosynthesis and respiration (*Garcia and Gordon*, 1992; *Spitzer and Jenkins*, 1989; *Loose et al.*, 2009; *Eveleth et al.*, 2014). Due to the effect of biology, the oxygen saturation is not a conservative tracer but changes after the watermass has lost contact with the atmosphere. This aspect has been used in the past to estimate the 'age' of a watermass, that is the time elapsed since the watermass has lost contact with the atmosphere (*Jenkins*, 1987; *Karstensen and Tomczak*, 1998). Such calculations are by no means exact and knowledge of the respiration and production rate of oxygen is needed to arrive at an interpretable time (*Jenkins*, 1987; *Karstensen and Tomczak*, 1998). We did not attempt to calculate an age here, but rather use oxygen saturation as a qualitative indicator of relative ages. The strong correlation we see between oxygen saturation and AW fraction makes oxygen saturation an additional tracer for this watermass. We saw that AW is still in contact with the atmosphere in the WSC in the eastern part of section 79°N. This is the source region for both recirculating AW and AAW. The WSC splits into branches with probably at least 50% of the AW recirculating in Fram Strait and the remainder circulating around the Arctic Ocean becoming AAW in the process (*Rudels*, 1987; *Manley*, 1995; *Marnela et al.*, 2013). Both recirculating AW and AAW lose contact with the atmosphere before they reach the EGC. However, transit through the Arctic Ocean takes longer, on the order of 10 years (*Karcher et al.*, 2003; *Polyakov et al.*, 2011), whereas the recirculation in Fram Strait is thought to take only a couple of months (*Gascard et al.*, 1995; *von Appen et al.*, 2016; *Hattermann et al.*, 2016). This difference in time is visible in the oxygen signal. If the rate of respiration and production along the path of AAW and AW were known it would be possible to calculate the time since subduction for each watermass at a given location and thus make inferences on the transport.

5.2   Circulation

Here we will take a closer look at the error estimate of our velocity calculation. The velocity field in the deep Fram Strait will be discussed before following the path of the EGC from north to south. Finally, we will integrate our view of the velocity field in the entire Fram Strait into a circulation scheme.

5.2.1   Error Estimates

The low relative error incurred by varying the search radius indicates that the sample density was sufficiently high for our chosen grid spacing. Due to large errors from changes in tension and grid spacing inside of the trough at WT1, especially in the upper tens of meters of the water column, we do not interpret the velocities in that area. In general we feel confident that our results do not suffer from large errors introduced through our choice of gridding parameters. Especially in the EGC, errors are generally low (below 20 %). Also note that the doubling and halving of the gridding parameters with respect to their optimal values is a rather large change leading to errors estimates larger than the probable ones. Errors made in transport calculations are expected to be even lower than the velocity errors due to the fact that transports more closely relate to the large scale gradients than the detailed velocity structure. We can not quantify the errors introduced in the ADCP measurements through environmental effects such as sea state and backscatter concentration or through interference with other acoustic instruments in operation during measurements (*Kanzow*, 2017). The low (< 1 cm/s) median absolute deviations of the ADCP measurements between 50 and 150 m depth suggest that no large error was incurred through the barotropic component of the absolute geostrophic velocity.

5.2.2   The Deep Fram Strait and the Westward Recirculation

The absence of AW at the northernmost station sampled along 0°EW (Figure 9 (a)) suggests that we captured the northern extent of the direct AW recirculation in Fram Strait. The eastward velocities in 0°EW may result from eddies or a meandering southward or northward current. It is possible that the structure of the velocity field is not well represented in our section as the station spacing was very large, thus increasing the effects of aliasing. Further, section 0°EW is less synoptic than the other sections presented in this thesis, with longer periods of time between individual station casts (see Table 4 in the Appendix for the time and date of casts). This increases the possibility of errors from spatially interpolating a time varying field sampled at different points in time. Previous studies have however reported eastward transport north of 79°30'N at 0°EW (*Marnela et al.*, 2013) variously related to the northern rim of the Molloy Hole eddy (e.g. *Hattermann et al.*, 2016). The model study by *Hattermann et al.* (2016) saw two branches of westward recirculation through Fram Stait, at 78.5°N and at 80°N. This agrees with our synoptic section at 0°EW (Figure 9 (c)). Longterm averages of model output suggest that the mean zonal current through 0°EW is southwestward (*Hatter-*

mann et al., 2016; *Kawasaki and Hasumi*, 2016; *Wekerle et al.*, 2017) and daily averages of the velocity field show eddies advected southwestward (*C. Wekerle, pers. comm., 2017*).

It is still unclear where the northern limit of the recirculation in Fram Strait lies. It is probable that the answer may depend on the watermass tracked as well as the time of the measurements. There is evidence from drifter data (*Gascard et al.*, 1995), an inverse modelling study (*Schlichtholz and Houssais*, 1999a) and a numerical ocean model (*Kawasaki and Hasumi*, 2016) that the recirculation in Fram Strait may extend beyond 81°N, possibly as far north as 82°N. Our synoptic section along 0°EW did, however show no AW at the northern most station (80.8°N). Due to the synoptic nature of our section it is not possible to ascertain if the lack of AW at 80.8°N is a transient feature or more permanent in time and space. A repeat survey along 0°EW extending beyond 81°N with a closer station spacing than in the present study and less time between casts, supported by a mooring array extending this far north, would be needed to get a better picture of the northern limit of Fram Strait recirculation and its meridional structure. The mooring array currently deployed at 0°EW only extends as far north as 80°51'N (*Kanzow*, 2017). Evidence from model studies is at present inconclusive as the northern limit of the recirculation and the strength of individual branches varies between models, possibly related to resolution (*Fieg et al.*, 2010; *Aksenov et al.*, 2010; *Hattermann et al.*, 2016; *Ilicak et al.*, 2016; *Wekerle et al.*, 2017).

The ~30 km wide areas of northward and southward velocity paired around domes in the density field seen along 79°N may represent eddies or a meandering current flowing parallel to 79°N and crossing the section repeatedly. The westward velocity observed at 79°N as a broad region in section 0°EW would point toward the latter explanation. Alternatively, the velocity structures seen in section 79°N may also be eddies advected westward by a background current. The average station distance along 79°N is 20 km, so that we cannot rule out the influence of aliasing on the width of these structures. Similar structures are however seen in the model realization at 79°N (*C. Wekerle, pers. comm.* (2017)), as discussed in Section 5.5. High variability is also evident in a previously published synoptic velocity section along 78°50' N (*Marnela et al.*, 2013), as well as in a temperature and salinity section along 79°N presented in *Langehaug and Falck* (2012). Another indication for high eddy variability in the central Fram Strait is presented in *von Appen et al.* (2016) from moored ADCP measurements at 79°N and 5°E. Here, the mean velocity is 0 m/s and varies between ±0.4 m/s in the zonal and meridional component. It is evident from the realizations of 79°N in *Marnela et al.* (2013); *Langehaug and Falck* (2012) and this thesis that the synoptic view of 79°N differs substantially from

the longterm mean as seen in e.g. *Beszczynska-Möller et al.* (2012) (Figure 3). The velocity field at 0°EW has bands of alternating direction of about 80 km width. Even though this is double the average station spacing along 0°EW (which is 40 km), this structure of the velocity field may be affected by aliasing too. Similarly, the surface intensification of velocities at the eastern end of section WT1 (around 1°W, 100 km in Figure 10 (c)) and the decrease in velocity between 4 and 2°W (50 and 100 km) in this section, may be a result of the larger station spacing here and not an actual feature of the flow field.

5.2.3   Eddies

Eddies play a crucial role in Fram Strait recirculation as well as in numerous other processes. As seen in the previous section, the synoptic transect along 79°N was able to capture numerous features that may be identified as eddies (Figure 8). Previously published cross-sections across Fram Strait (especially long-term means from moorings, e.g. *Beszczynska-Möller et al.* (2012)) make the section appear rather smooth. In contrast, Figure 8 shows a qualitative picture of instantaneous eddy variability. We think that it is representative that the mean boundary currents (WSC and EGC) instantaneously appear weaker than the eddies present in Fram Strait. Eddies are shed by the WSC (*von Appen et al.*, 2016; *Walczowski*, 2013; *Teigen et al.*, 2010, 2011) and cross the front between AW and the cooler, fresher waters in the centre of Fram Strait and the Greenland Sea (the Arctic Front (*Walczowski*, 2013)). Thus they play an important part, not only in the westward transport and recirculation of AW, but also in transporting heat and salt into the central Greenland Sea (*Walczowski*, 2013) with implications for deep convection (*Gascard et al.*, 2002). WSC eddies are also instrumental in cooling AW in the WSC core on its way northward via air-sea interaction and mixing with colder waters from the central Fram Strait and from the Svalbard shelf (*Teigen et al.*, 2010, 2011; *Walczowski*, 2013). Thereby, they influence the amount of heat transported into the Arctic Ocean and the extent of the sea-ice cover north of Svalbard (*Piechura and Walczowski*, 2009). In addition to exchange of heat, salt and mass across the oceanic front between the WSC and the central Fram Strait, these processes are also relevant for the front between Atlantic influenced waters in central Fram Strait and waters of Polar origin in western Fram Strait (the Polar Front (*Walczowski*, 2013)). The surface expression of this front largely coincides with the ice-edge in Fram Strait (*Paquette et al.*, 1985; *Quadfasel et al.*, 1987), the position and shape of which is influenced, amongst other processes, by eddies (*Johannessen et al.*, 1987; *Gascard et al.*, 1988). Further, baroclinic instability may help

subduct AW underneath PSW and sea-ice (*Hattermann et al.*, 2016), forming additional eddies in the process. A large ice-eddy was described by *Smith et al.* (1984); *Wadhams and Squire* (1983) which appears at the same general location in multiple years. The generation and location of this eddy was associated with the Molloy Hole bathymetric feature (*Smith et al.*, 1984). A topographically generated cyclonic eddy at Molloy Hole has been described by numerous authors (e.g. *Smith et al.*, 1984; *Johannessen et al.*, 1984; *Quadfasel et al.*, 1987) and has a diameter of 60–100 km (*Johannessen et al.*, 1987; *Quadfasel et al.*, 1987). The eddy is centered around 79°30'N, 2°E (*Smith et al.*, 1984) with some variation. The 100 km wide cyclonic eddy structure seen in Figure 8 at 2°E may be the southern rim of this eddy, though it would be further south than most previous observations. This assumption is however made additionally uncertain by the large station spacing at the location of the eddy, which increases the likelihood of aliasing. The fact, that section 79°N is not completely synoptic is less likely to have influenced this particular structure. The only large time difference between neighbouring station casts is at ~2°W, so that the section to the east and west of this point may be considered synoptic (see Table 4 in the Appendix for further information on station casts).

Apart from these physical processes associated with eddies, eddies play an important role for biology in Fram Strait. Vertical motions in the ocean are important for primary production because they move both phytoplankton and nutrients into and out of the euphotic layer. Specifically, in post-bloom summer conditions, vertical upward nutrient transport from depth into the euphotic layer can sustain phytoplankton growth. In Fram Strait, especially at the rims of eddies, large vertical motions can occur that may bring Atlantic water upwards (*Smith et al.*, 1985; *Niebauer and Smith*, 1989), which has much larger nutrient concentrations than Polar water (*Smith et al.*, 1985; *Jeansson et al.*, 2008).

5.2.4 The EGC

The downward sloping of isopycnals in the vicinity of the shelfbreak is a characteristic of baroclinic boundary currents, such as the WSC and EGC. Downward sloping isopycnals likely associated with the boundary currents in Fram Strait are seen in both the east (0.64 m/km in the WSC) and west (0.75 m/km in the EGC) of section 79°N as well as the center of NT1. At WT1 the slope of the 27.8 kg/m³ isopycnal is very weak at the shelfbreak (0.25 m/km), which suggests that the EGC is not a boundary current at this point in space and time. Just 50 km further to the south, at 79.6°N there is

some sloping of isopycnals at the shelfbreak (around 4°W the 27.8 kg/m³ isopycnal has a slope of 0.5 m/km) which may be associated with a boundary current EGC. On the other hand the isopycnals may be spread apart by AW intruding below and/or above the AAW layer at depth. Indeed, the isopycnals below 27.9 kg/m³ slope upward toward the shelfbreak. The signal in the isopycnals of the intruding AW may likely not be merely synoptic but a process observed generally whenever AW meets AAW at depth with a distinct and strong gradient. In section 79°N, the downward sloping isopycnals (a slope of 0.75 m/km toward the shelfbreak for the 27.8 kg/m³ isopycnal) are located where we would expect the shelfbreak EGC based on mooring observations (e.g. *Beszczynska-Möller et al.*, 2012) and coincide with southward velocities. Here the EGC is a boundary current. Another increase in the slope of the 27.8 kg/m³ isopycnal is seen at NT1 where it reaches 1.66 m/km.

Even though this thesis gives an indication at which latitude the EGC first portrays features of a boundary current it is unable to resolve the transition from a barotropic Arctic outflow north of 80°N to the density driven, baroclinic boundary current EGC seen at and south of 79°N. No previous studies have, to our knowledge, addressed this question. Numerical model results suggest that north of 79°N the density front associated with warm recirculating AW and a band of high southward velocities is located not at the East Greenland shelfbreak but further east in the deep Fram Strait (*Wekerle et al.*, 2017). This current, located east of 0°EW north of 80°N in the model, would then be part of the Arctic boundary current loop, including the WSC and the EGC south of 79°N. A southwestward flowing current at 80–80.5°N and as far east as the lower slope of the Yermak Plateau was described by *Schlichtholz and Houssais* (1999a) from results of an inverse modelling study. This current follows the Polar Front and the ice-edge before converging with the EGC between 79°N and 80°N. A similar jet following the ice edge was observed by *Paquette et al.* (1985). Further investigations are needed to establish if the southward current we observed at the shelfbreak at WT1 is a perennial feature and if either this, the current seen at 0°EW in model results, or both are the northward continuation of the EGC as seen at 79°N. Numerical model output showing the southward flow north of 79°N and west of 0°EW is further discussed in Section 5.5. The surface intensified current seen on the shelf at 79°N, between 7.5 and 10°W (-90 and -20 km Figure 8 (c)), does not transport any or only very little AW and thus may correspond to the PSW jet described by *Håvik et al.* (2017) for sections further to the south and seen in the May 2002 hydrographic data of *Nilsson et al.* (2008) as far north as 79°N. *Håvik et al.* (2017) and *Nilsson et al.* (2008) described three branches of the EGC at and south of 79°N: an onshelf branch (the PSW jet), the shelfbreak branch and
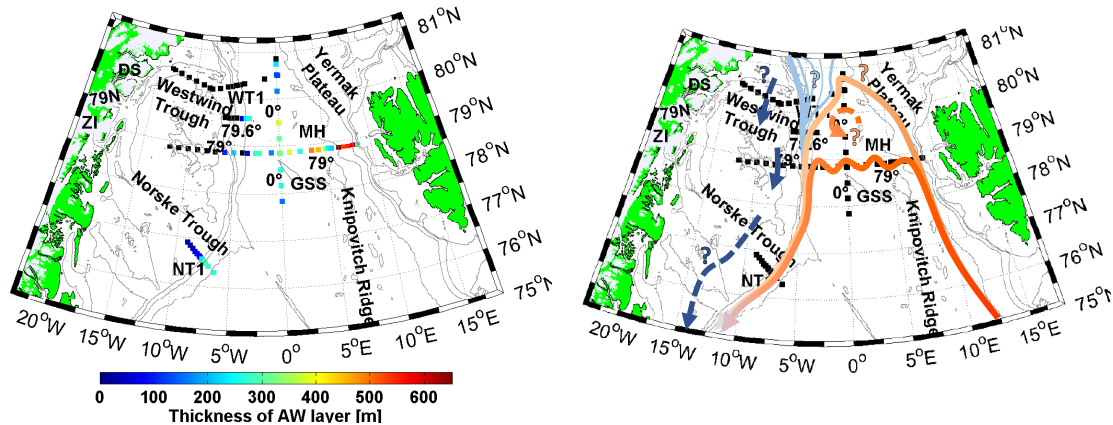
Figure 25: Map of Fram Strait. The left panel shows stations at which AW is present, colour corresponds to the thickness of the AW layer in the watercolumn, stations at which no AW was measured are shown in black. The circulation scheme updated with our findings is shown in the right panel. Features we only speculate about are shown dashed and with a question mark.

an offshore branch. We do not see an offshore branch in any of our sections. This does not rule out the presence of EGC branches, either to the south of our study area (where they were described by *Håvik et al.* (2017)), nor along our sections. In section WT1 we see a southward jet on the shelf but the velocity errors in the trough are too high to allow us to be certain that this feature is not an artefact of the analysis. In section 79°N the variation in the velocity field is too high to distinguish any time-mean structure from possible transient eddies, while sections 79.6°N and NT1 unfortunately do not extend far enough either side of the shelfbreak to capture the inner and outer EGC branches, if present. Further investigations are needed to establish the presence or absence of EGC branches in Fram Strait.

5.2.5   Circulation Scheme

The maps of Fram Strait shown in Figure 25 summarise the view of Fram Strait recirculation we have drawn from this analysis. The left panel shows the thickness of the AW layer, shown earlier as potential temperature and salinity cross sections (Section 4.1). The eagle-eye view of AW layer thickness is used to guide the circulation scheme sketched in the right panel. The WSC brings AW northward in eastern Fram Strait. Here AW is still in contact with the atmosphere. Recirculating AW subducts under PSW on its way westward and in our synoptic summer survey along 0°EW no AW was found at 80.8°N, suggesting that the northern extent of the westward recirculation of AW in

Fram Strait lies here. No AW is found within Westwind Trough or indeed within 100 km of its mouth. AW was first observed in the shelfbreak EGC at 79.6°N and was found inside of Norske Trough, at a depth that would allow it to propagate to the terminus of 79NG. The synoptic view of the hydrographic and velocity fields at section 79°N were very dynamic and differed greatly from the multi-year averages of the section gained from the mooring array at ~79°N. The westward transport of AW along 79°N is likely in the form of a meandering current or an eddy field. We have marked with question marks some aspects of the circulation that remain unclear. These are the northern extent of the recirculation, the location of the EGC between the shelfbreak at WT1 and 0°EW, the circulation structure in the central Fram Strait north of 79°N (possibly associated with Molloy Hole) and the shelf circulation, especially the PSW jet.

5.3   Transport

In this section the transport in the EGC will be examined and compared to previous studies. Net transport in the EGC as well as AW and DSOW transport will be discussed. We will further examine our transport estimates in context with long term observations from moorings.

As seen in Figure 24 the transport through section 79°N does not follow the trend of increasing transport with decreasing latitude. The transport is also low when compared with previous estimates of southward transport through 79°N. Estimates from the longterm mooring array at ~79°N range between 3.7±1.4 Sv and 13.7±1.7 Sv southward transport (*Fahrbach et al.*, 2001; *de Steur et al.*, 2009, 2014), an inverse dynamical model based on MIZEX data estimated 6.2±1.0 Sv at 78.9°N (*Schlichtholz and Houssais*, 1999a). Transport estimates similar to our estimate at 79°N were reported in *Bourke et al.* (1987) for sections between 74°N and 84°N. Here, southward transport in the EGC was 1.47 Sv and the net transport only 0.89 Sv. The estimates do however only include the baroclinic transport in the upper 500 m and are thus likely too low. Our definition of the EGC transport only includes the shelfbreak EGC as defined by *Håvik et al.* (2017). To determine whether a more inclusive definition of the EGC can yield a higher southward transport through 79°N we calculated the net transport and the sum of all southward transport components through 79°N between 6.5°W and 0°EW. These are the boundaries used in the analysis of the the mooring line at ~79°N in *de Steur et al.* (2009, 2014). Our net transport was northward and the southward transport between 6.5°W and 0°EW was only 2.4 Sv and thus below the monthly range reported for August and September from ten years of mooring data (1998–2008) (*de Steur et al.*,

2009). The difference becomes even more marked when comparing our transport estimate to the southward transport at the mooring array after it was shifted to 78.8°N (where our section casts were taken), here the minimum monthly mean volume transport is above 4 Sv between 2002 and 2009 (*de Steur et al.*, 2014). It has to be noted that our section is synoptic whereas *de Steur et al.* (2009, 2014) report monthly means. It is therefore possible that the mooring array recorded southward transports as low as 2.4 Sv sporadically within any given month and that the overall net transport may have been northward at times. It also has to be kept in mind that our station spacing is denser than the spacing of the moorings and thus interpolation between moorings may remove much of the small scale variability we see in our synoptic section of 79°N resulting in higher transport estimates.

Our low transport estimates for section 79°N, as well as the high variability of watermass properties in the EGC at this section may be due to the strong mixing between AAW and AW and the dynamic velocity field encountered here. As mentioned above, the EGC has also been suggested to produce branches (*Håvik et al.*, 2017) and our low transport estimate for the shelfbreak EGC may be caused by transport diverted into another region of the flow field such as for example eddies. Since the AW transport at 79°N is high relative to the total EGC transport, 'missing' transport would most likely be AAW and PSW. These watermasses are found on the shelf at 79°N where the surface intensified jet, tentatively called PSW jet by us following *Håvik et al.* (2017), lies. This is the surface intensified jet on the East Greenland shelf that we see 50 km inshore of the shelfbreak at 79°N (Figure 8) and we will discuss it in more detail in Section 5.4.

Just as the transport estimate for the EGC, the transport estimate for the WSC at 79°N is also very low (only 0.2 Sv northward) compared to values reported in the literature (*Schlichtholz and Houssais*, 1999a; *Osinski et al.*, 2003; *Aksenov et al.*, 2010; *Beszczynska-Möller et al.*, 2012) and may be caused by the synopticity of the section. The WSC produces branches, an offshore branch and a core branch located on the upper slope (*Beszczynska-Möller et al.*, 2012; *von Appen et al.*, 2016). The fact that the section at 79°N does not extend to the Svalbard shelfbreak and thus most likely only completely captured the offshore branch of the WSC, may be another reason for the transport value which must be seen as a lower boundary estimate. The offshore branch is very weak during summer months (*von Appen et al.*, 2016) and our low transport values may reflect this. Though our estimate does not lie within 1-standard deviation of the 1997–2010 monthly means for July to September (*Beszczynska-Möller et al.*, 2012), some outliers for individual months and years lie close to 1 Sv. Considering that the mooring array extends further eastward than our transect, thus capturing the WSC core,

and only monthly averages are reported, these values make our own estimate appear at least not implausible.

Transport of DSOW (defined as water above 800 m depth and denser than 27.8 kg/m³) increases from north to south. We use a lower boundary of 800 m even though the Denmark Strait sill depth is only 650 m, because it was demonstrated in *Harden et al.* (2016) that aspiration takes place down to ~800 m. If the deep 0°C isotherm is used as a lower boundary (as done in *Håvik et al.* (2017)) our transport estimates increase by 0.1 Sv at each section. Our transport estimates for DSOW in the EGC at NT1 of 2.5 Sv agree well with the 2.8±0.7 Sv average of the DSOW transport at the 10 sections between 78°N and 68°N reported in *Håvik et al.* (2017) and the annual mean of 2.5±0.2 Sv reported in *Harden et al.* (2016) for the EGC south of 68°30'N. As already noted for the total transport, the DSOW transport increases from north to south between WT1 and NT1, whereas *Håvik et al.* (2017) saw a decrease in both quantities from north to south starting 500 km downstream of their Section 10 at 77.5°N. The initial increase in total transport may be explained by the gradual formation of the EGC as a baroclinic boundary current from north to south and the recirculating AW joining the current. This AW is in part dense enough to fall in the range of DSOW thus contributing to the increase in DSOW transport from north to south. The deep overflow water in Denmark Strait is thought to be primarily formed by ice-ocean-atmosphere modification of the inflowing AW along the boundary current loop encircling the Arctic Mediterranean (*Mauritzen*, 1996). The decrease in EGC transport observed south of 74°N is attributed by *Håvik et al.* (2017) to the separation of the EGC into multiple branches. It is however remarkable that the average DSOW transport in the shelfbreak EGC appears to be so constant south of 78°N, with values from NT1, the synoptic sections analysed in *Håvik et al.* (2017) and the year-long mooring-array averages in *Harden et al.* (2016) agreeing within their error-bounds.

We have not attempted to calculate westward transport of recirculating AW in our study though the change in AW transport in the shelfbreak EGC between different sections may be seen as a minimum estimate. It has to be kept in mind, that the AW transport we show in Figure 24 only includes the shelfbreak EGC and thus my exclude a large portion of the AW transported southward elsewhere in western Fram Strait. AW transport in the shelfbreak EGC through section 79°N was 0.77 Sv. If we remember that the measurements in western Fram Strait were taken close to 78.9°N, we can compare our result with the sum of the multi-year average transport north of 79°N and between 79°N and 78.9°N from mooring velocities reported in *de Steur et al.* (2014) which is 0.66 Sv and thus close to our synoptic estimate (see Table 3). The different definition of

Table 3: Different recirculation estimates in Fram Strait from the literature. Location is the location of the data *and* recirculation estimate unless otherwise stated.

Method	Recirculation [Sv]	Location	Data/Model	Time	Reference
time averaged model output	1.2± 1.5	approx. ~77–79°N[1]	high-res., global ice-ocean model	1989–2004	*Aksenov et al.* (2010)
AW transport[2] time averaged model output	1.0± 1.2				
velocities from moorings	2.6± 0.1	1.8°E–1.8°W, 78°50' N – 79°N[3]	mooring array at 78°50'N	1997–1999	*Fahrbach et al.* (2001)
AW velocities from moorings[5]	0.16± 0.16	north of 79°N[4]	mooring array at 78°50'N	1997–2009	*de Steur et al.* (2014)
	0.5± 0.43	78°50'N–79°N			
velocities from moorings	2.7	79°N[6], 6.5°W–~1°W			
baroclinic transport[7]	0.69	0°EW, 78°–78.8°N	summer hydrography	1997	*Marnela et al.* (2013)
	0.97			2001	
	1.06			2003	
	0.66	0°EW, 78.8°–80°N		1997	
	-0.57			2001	
	1.23			2003	
baroclinic transport	0.4	2°E, 79°N–81°N	summer hydrography	1985	*Bourke et al.* (1988)
	0.8	south of 79°N			
inverse model with dynamic constraints	1.8± 0.8[8]	77.6°N–78.9°N	MIZEX-84 Data	1984	*Schlichtholz and Houssais* (1999a)
	0.5± 0.5[8]	78.9°N–79.9°N			
	0.5± 0.3[8]	79.9°N–80.75°N			
budget considerations from hydrography and volume transports (geostrophy)	1.7	Fram Strait[9]	summer hydrography and LADCP	2002	*Marnela et al.* (2008)

1 Knipovitch branch, location see Figure 2
2 AW S≥ 34.8, T≥ 1.0°C
3 Between moorings F8 and F9 (see *Fahrbach et al.*, 2001)
4 Between 79°N and northern limit of recirculation
5 AW defined after *Rudels et al.* (2008): T > 2 °C depth < 500 m
6 mooring array location changed from 79°N to 78°50'N between 1997 and 2009
7 Level of no motion near bottom
8 Average of model runs
9 Data from north of 80°N but estimate for entire FS

AW used here and in *de Steur et al.* (2014) ($\theta > 2$°C and depth < 500 m) is not expected to produce large differences in what is classified as AW since all our AW in the EGC at 79°N is above 500 m (Figure 8). Further transport estimates can be seen in Table 3. These employ different methods and data sources to arrive at transport estimates, all of which have caveats attached. When examining net east-west transport or the change in EGC transport between two latitudes it is assumed that all westward transport that joins the EGC is recirculating, this includes watermasses other than AW from the WSC. Examining AW transport relies on somewhat arbitrary watermass definitions from their temperature and salinity characteristics and makes it hard to compare to values from other studies using different definitions. A fixed watermass definition will also include water that is not recirculating or exclude water that is. Furthermore, this is not able to track changes in watermasses over time. Comparison of transport estimates is further complicated by the use of different data and calculation methods. Hydrography alone can only yield baroclinic geostrophic transports; direct velocity measurements are needed to calculate barotropic and absolute geostrophic transports and some studies include constraints in their calculations or use different kinds of models.

Between 1997 and 1999 the mean northward volume transport across the mooring array was 9.5 ± 1.4 Sv and the southward transport 11.1 ± 1.7 Sv (*Fahrbach et al.*, 2001). As the mooring line location switched from 79°N to 78°50'N in the middle of Fram Strait the westward transport has to be added to the measured southward transport to give total net southward transport at 78°50'N of 4.2 ± 2.3 Sv (*Fahrbach et al.*, 2001). *de Steur et al.* (2014) reported that through a shift of the western part of the mooring line from 79°N to 78°50'N the measured southward transport in the EGC increased by 2.9 Sv implying that recirculation of this magnitude joins the EGC between these two sections (this is transport including but not restricted to AW). This value is higher than the increase in transport between 79.6°N and section NT1, as seen in our summer synoptic survey (Figure 24). Again the differences between multi-year transport averages (integrated over a wider area than in our study) and our synoptic observations of a single current feature are not surprising. By comparison the merit of our study is the increased information on the horizontal distribution of the currents.

5.4 Implication for the EGC further south and the flow of waters from the EGC onto the shelf

As mentioned earlier, our study area connects to the study area of *Håvik et al.* (2017) which is to the south of our study area, with some overlap near NT1. Since our definition

of the width of the shelfbreak EGC follows *Håvik et al.* (2017), a comparison of the transport estimates is possible. *Håvik et al.* (2017) noted an increase in shelfbreak EGC transport only within 500 km downstream of Fram Strait; south of 74°N the transport began to decrease. The transport of the shelfbreak EGC of their Section 10, located just to the north of our section NT1, matches well with our estimate for NT1 though our velocities are significantly lower. This is balanced by the greater width of the shelfbreak EGC at NT1 compared to their Section 10 (Figure 24). Velocities measured at their Section 9, just to the south of NT1, were closer to our value for NT1 though transport and current width at their Section 9 was higher. Velocities and current widths measured by *Håvik et al.* (2017) were generally higher than those recorded in the present study. This is consistent if one assumes that the increase in isopycnal slope seen between WT1 and NT1 (Section 4.1) continues further to the south given that steeper isopycnals at the shelfbreak cause increased baroclinic velocities. Another explanation could be the denser station spacing in *Håvik et al.* (2017). Their station distance was typically 5-7 km whereas our densest station spacing was at least twice that value. The core velocity of the EGC was defined as the maximum mean velocity in the upper 150 m of the watercolumn in both *Håvik et al.* (2017) and this study. With a denser station spacing it is more likely to sample the location in the EGC with the highest velocity, thus making it more likely to arrive at a higher core velocity.

Only two of our sections extended far onto the East Greenland shelf, section WT1 and 79°N. At both sections we can thus observe part of the shelf circulation. We have already mentioned the southward flowing PSW jet seen at 79°N (Figure 8). The distance of the PSW jet in our section and the peak velocity agrees with the distance from the shelfbreak and peak velocity recorded in *Håvik et al.* (2017). Our transport in the PSW jet (1.1 Sv southward) is however higher than the transports reported for the PSW jet further south (0.54±0.28 to 0.83±0.27 Sv southward). The southward flowing current seen in the trough at WT1 (Figure 10) may be a northward continuation of the current seen at 79°N. However the uncertainties of our absolute geostrophic velocity inside the trough at WT1 do not allow for a robust assessment of this hypotheses. The PSW jet is an important pathway for freshwater transport in the EGC current system (*Håvik et al.*, 2017) which in turn has an important effect on deep convection and the Atlantic Meridional Overturning Circulation (e.g. *Curry and Mauritzen*, 2005). The location of the PSW jet on the East Greenland shelf, between the EGC and marine termini of glaciers makes it important for our understanding of possible exchanges between the three. The mooring array in Fram Strait at 78°50' N does however not extend far onto the shelf (*de Steur et al.*, 2014), we thus have no longterm record of freshwater and

total transport on the East Greenland shelf. The question has been asked if the PSW jet seen north of Denmark Strait is the same feature as the East Greenland Coastal Current (EGCC) observed by *Sutherland and Pickart* (2008) south of Denmark Strait (*Håvik et al.*, 2017). The transport estimates of the PSW jet reported here and in *Håvik et al.* (2017) agree with transport estimates of the EGCC (*Sutherland and Pickart*, 2008; *Bacon et al.*, 2002). The EGCC was not present north, that is upstream, of Denmark Strait and was indeed suggested to be a branch of the EGC (*Sutherland and Pickart*, 2008). Conversely, the EGCC was suggested to be primarily meltwater driven by *Bacon et al.* (2002). However, the EGCC was shown to be seasonal, with higher transport in winter than in summer (*Bacon et al.*, 2014), a result not well compatible with the former theory. A feedback between the EGCC, the EGC and Southeast Greenland glacier acceleration and thinning via meltwater discharge was proposed by *Murray et al.* (2010). This indicates the importance a better knowledge of the Greenland shelf circulation may have for our understanding of Greenland ice-ocean interactions. Further measurements on the East Greenland shelf are needed, both north and south of Denmark Strait and during winter and summer to decide on the possible connection between PSW jet and EGCC as well as the seasonality, drivers and northward extent.

Our data does not allow for a study of the transport inside Westwind and Norske Trough as both WT1 and NT1 are oriented along the trough axis and not perpendicular to it. We can thus not decide whether the deep circulation in the troughs follows the anticyclonic surface circulation described in (e.g. *Bourke et al.*, 1987; *Johnson and Niebauer*, 1995), with an inflow at Norske Trough and an outflow through Westwind trough, or if there is rather a two directional flow in each trough as suggested by *Topp and Johnson* (1997); *Budéus et al.* (1997); *Schaffer et al.* (2017). Sections, crossing Norske and Westwind Trough between the shelfbreak and the 79NG terminus, were however sampled during summer 2016 (*Kanzow*, 2017) and later analysis of these should provide insights on the deep circulation in the troughs. Such an analysis would bridge the gap in our understanding of AW transport left between this thesis and *Schaffer et al.* (2017).

5.5 Numerical Model Results

Synoptic sections, mooring arrays and numerical models can be used to enhance the interpretations drawn from each individual method. For this study we compared our section hydrography and velocity to results from the FESOM high-resolution numerical model setup (*Wekerle et al.*, 2017, in revision). FESOM is a global finite-element sea-ice ocean model. The eddy-resolving configuration of FESOM focusing on the Fram Strait

described by (*Wekerle et al.*, 2017, in revision) has a horizontal resolution of 1km there. Eight years of model output are available. Eight-year averages for temperature, salinity, density and absolute geostrophic velocity of our sections were calculated for 2002–2009 and daily averages for the year 2009. Daily model averages resolve similar time and space scales to the shipboard synoptic sections discussed in this thesis. There is no qualitative difference in the points discussed below between the eight-year mean and the eight-year summer mean of the FESOM output (*C. Wekerle, pers. comm.,* 2017).

Examining the mean temperature at 0°EW shows average temperatures above 2°C at depth at the northern end of the section. This suggests that the northern rim of the recirculation lies northward of this. Alternatively, the presence of warm water at this latitude may be related to the presence of the Yermak branch of inflow to the Arctic Ocean close to 0°EW. The northern limit of the recirculation may have been south of the northern most station of 0°EW in summer 2016 or we may have only sampled an AAW filament or eddy at our northernmost station. Such filaments of eddies of water below 2°C are seen in the daily averages of the model run for 2009. Future synoptic and long term studies may have to extend further north along 0°EW to decide if the northern recirculation is too far north in the FESOM results or if our synoptic section at 0°EW is unusual compared to a long term mean. It has been noted previously that correctly representing the latitudinal structure and especially the northern extent of the AW recirculation in Fram Strait remains a challenge for models, with model results strongly dependent on both horizontal and vertical resolution (*Fieg et al.*, 2010), which calls for observational verification.

The eight-year mean of velocities at 79°N does not show the dynamic velocity field with interchanging bands of north and southward velocities seen in the synoptic section. These are however resolved in the daily averages, showing a similar width of the alternating velocity bands as our section and similar velocity amplitudes. The daily averages from FESOM show that the very dynamic velocity structure at 79°N is not an artefact of our measurement technique which cannot achieve perfect synopticity. It rather is representative of the synoptic eddy field, a view that is typically lost in depictions of long-term averages (e.g. *Beszczynska-Möller et al.*, 2012). The same is true for the surface intensified current on the shelf that is seen in the synoptic section. This too is sometimes present in the the daily averages from FESOM.

At WT1 the deep AW core present in the eight-year model average reaches much closer to the shelfbreak than in our section, though not into the trough. This is also true for the daily averages in 2009. The isopycnals in the FESOM realizations of WT1 are very flat, supporting our finding that the EGC is not a boundary current at WT1.

The slope of isopycnals at 79.6°N, which led us to conclude that the EGC is a boundary current at this latitude, is not seen in the eight-year model average of the section. The daily averages show some sloping, suggesting that the EGC may be a boundary current at 79.6°N during some part of the year but the main southward velocities computed here are the result of eddies passing through 79.6°N. This means that we may either have sampled 79.6°N at a time when the EGC was a boundary current here, or resolved the southward flowing rim of an eddy at the section. The former is supported by the fact that the EGC at 79.6°N lies closer to the shelfbreak in summer (*Wekerle et al.*, 2017), the latter is supported by the upward sloping isopycnals seen below 200 m and the northward velocity at ~40 km.

The model is also able to capture the AW layer within Norske Trough, seen both in the eight-year average and in the daily averages for 2009.

These results make us confident that our synoptic sections are representative for the situation in Fram Strait during summer months and suggest that the FESOM setup with a 1 km horizontal resolution is able to capture the overall dynamics of the system. Further numerical model studies were conducted by *Aksenov et al.* (2010); *Fieg et al.* (2010); *Kawasaki and Hasumi* (2016); *Maslowski et al.* (2004); *Hattermann et al.* (2016) and a model inter-comparison for the Arctic Ocean was analysed by *Ilicak et al.* (2016). There are significant differences between the models and between model output and observations, often related to resolution (*Fieg et al.*, 2010; *Ilicak et al.*, 2016; *Wekerle et al.*, 2017). Common biases between models and observations are the temperature in the central Fram Strait and the velocity and transport of the WSC and EGC, even if the net transport is well captured (*Ilicak et al.*, 2016; *Maslowski et al.*, 2004; *Wekerle et al.*, 2017). A resolution high enough to resolve eddies can increase eddy activity in the models. This increases AW transport into the central Fram Strait and vertical transport of AW, that is subduction under PSW and sea-ice, and thus reduces a cold bias in the central Fram Strait. However, so far only two studies employed a high enough resolution to resolve eddies (*Hattermann et al.*, 2016; *Wekerle et al.*, 2017). Two main 'currents' transporting recirculating AW westward are seen in models: one, following the Knipovitch Ridge at about 78.5°N, possibly related to the northeastern rim of the Greenland Sea Gyre and a northern recirculating branch associated with the northern rim of a stationary cyclonic eddy at Molloy Hole (~80°N) (*Aksenov et al.*, 2010; *Hattermann et al.*, 2016; *Kawasaki and Hasumi*, 2016; *Wekerle et al.*, 2017). The northern recirculation is stronger in winter when there is more eddy activity (*Hattermann et al.*, 2016; *Wekerle et al.*, 2017). The northern extent of the recirculation varies between models, in *Aksenov et al.* (2010) recirculation reached up to 80°N (although AW warmer than 2°C

was found north of 80°N at 0°EW, this however flowed eastward into the Arctic Ocean), in *Kawasaki and Hasumi* (2016); *Hattermann et al.* (2016); *Wekerle et al.* (2017) recirculation reached 81 to 82°N. The EGC is seen in multi-year model averages as a broad flow north ~78°30'N, extending east to 0°EW, and only forms a narrow current following the East Greenland shelfbreak south of 79°N (*Hattermann et al.*, 2016; *Kawasaki and Hasumi*, 2016; *Wekerle et al.*, 2017). This may be an artefact of the averages, portraying the mean of a meandering current or may in fact indicate that the EGC is not well defined current north of 79°N. This compares well with the low isopycnal slope we see at WT1 and the broad southward current there, extending to 0°EW. Especially when keeping in mind the indications from observations and model output that the southwestward flow north of 79°N does not follow the East Greenland shelfbreak discussed in Section 5.2.4. The circulation in this area is not at all well understood at present and future observational studies are needed to decide upon the representativeness of both the synoptic observations and the FESOM output discussed here.

he comparison with the models highlights the value of synoptic sections in Fram Strait. The time mean of both model results at 79°N (*Wekerle et al.*, 2017) and mooring measurements (e.g. *Beszczynska-Möller et al.*, 2012) are not representative of the synoptic view. Only the daily averages from FESOM were able to capture the velocity structure seen in the synoptic section at 79°N shown in *Langehaug and Falck* (2012); *Marnela et al.* (2016) and this thesis. Showing the highly variable structure of the flow field is important to reconcile measurements that at first seem counter intuitive, such as northward flow in areas where the EGC is expected, with the overall circulation in Fram Strait. It is also important for understanding the manifold processes (e.g. salt and heat transport to central Fram Strait and nutrient exchange between the surface layer and deeper watermasses; see Section 5.2.3) mediated by small scale features such as eddies. The small scale and highly variable structure of the velocity field in Fram Strait makes it essential to conduct both hydrographic surveys and model runs at an appropriate resolution to prevent e.g. aliasing.

6   Summary and Conclusions

We started our investigation of the AW flow field in Fram Strait with two hypotheses. 1: there is no AW in Westwind Trough and 2: AW is found below PSW and offshore of AAW in the EGC.

From our analysis we have been able to see that there is no AW inside of Westwind Trough, or indeed within 100 km east of the trough mouth. This is the case even though

recirculating AW was found north of WT1 at 0°EW and just 50 km south of WT1 at 79.6°N. In addition, a previous survey along 81°N did not find AW closer than 100 km to the shelfbreak (*Rudels et al.*, 2005; *Nilsson et al.*, 2008). It is important to keep in mind that these results are from summer synoptic sections. Results from the FESOM model suggest that AW may be present closer to Westwind Trough than in our results, though not inside the trough itself. From our synoptic section and the model we can thus conclude that at present no directly recirculating AW propagates toward the glacier termini of the NEGIS via Westwind Trough.

The second hypothesis concerning the horizontal and vertical structure of watermasses in the EGC holds for section 79.6°N. Further to the south there is increased mixing between watermasses breaking down the AAW/AW division. It seems that although the hypothesis holds in areas where AW has recently joined the EGC, the watermass structure in the watercolumn may be different further downstream and especially in areas where the EGC splits into multiple branches. The increased mixing of AW with AAW changes the properties of the water transported in the shelfbreak EGC, as could be seen when comparing the θ-S diagrams of section 79.6°N and section NT1 (Figures 11 and 12).

The synoptic section analysed here showed a dynamic flow field at 79°N dominated by eddy-like structures. This view of the circulation structure in Fram Strait is markedly different from the time-mean realizations published previously (e.g. *Beszczynska-Möller et al.* (2012)). It is however none the less crucial for forming a realistic and complete view of important processes associated with eddy transport and mixing (e.g. primary productivity and nutrient exchange, heat, salt and mass transport into the central Fram Strait and watermass transformation).

From our data alone we cannot conclusively infer the northern limit of the recirculation. As discussed in comparison with the FESOM model output, the lack of AW at the northernmost station along 0°EW may merely be a passing AAW filament. The northern limit of the recirculation is also likely to shift position with time or display a seasonal cycle. In order to resolve this, further repeat synoptic surveys during different seasons and years, as well as a mooring array reaching far enough north, would be needed.

Further investigation of the circulation north of 79°N is needed to establish where exactly the shelfbreak EGC becomes a boundary current and where it separates into branches. Our sections revealed that at WT1 the EGC is not a boundary current. At 79.6°N the EGC is also most likely not a boundary current whereas at 79°N the EGC clearly is a boundary current as shown by the downward sloping isopycnals in the shelfbreak EGC. It is not possible to ascertain from our data where and how the Arctic Ocean outflow

(both along the Northeast Greenland shelfbreak and further eastward) coalesces into a clearly defined current with a baroclinic component. Also, sections 79.6°N and NT1 do not extend far enough, both onto the shelf and towards the deep Fram Strait, to capture offshore and onshelf branches of the EGC, such as the PSW jet (as evidenced in *Nilsson et al.* (2008); *Håvik et al.* (2017)), if present. To elucidate these points, sections north of 79°N need to extend both further eastward and further onto the East Greenland shelf, than the sections analysed here. This study encountered the PSW jet as far north as 79°N with indications that it may be present even further north (at WT1). A study focusing on the relationship between PSW jet and the EGCC south of Denmark Strait as well as their seasonality and drivers may enhance our understanding of freshwater transport on the East Greenland shelf as well as possible ice-ocean feedbacks (*Murray et al.*, 2010).

The transport estimates within the EGC (with the exception of 79°N) agree well with previous estimates. Net transport through 0°EW and 79°N as well as in the WSC are lower than previous estimates, possibly due to the synoptic nature of the transects, the large station spacing along 0°EW and only partial coverage of the WSC. Extending the section at 79°N further onto the West Spitsbergen shelf during future transects would allow a more complete picture of the WSC.

No focus was laid on distinguishing sources and pathways of deep and intermediate watermasses (AIW, uPDW, NDW, CBDW and EBDW). We could however demonstrate that the transport of DSOW in the EGC increases up to NT1 were it reaches values close to those presented in *Harden et al.* (2016) for a mooring array south of 68°30'N. This indicated that though there is variation in the DSOW transport between NT1 and 68°30'N (*Håvik et al.*, 2017) the average DSOW transport in the shelfbreak EGC stays constant after exiting Fram Stait.

We presented evidence that KW is advected from the Arctic Ocean into Fram Strait. In combination with measurements at the terminus of 79NG (*J. Schaffer, pers. comm.,* 2017), we suggest that non-knee water found on the East Greenland shelf at WT1 and 79°N is glacially modified KW, possibly transported to WT1 in an anti-cyclonic surface circulation on the shelf (*Bourke et al.*, 1987). Data which would make it possible to test this hypothesis was collected inside the troughs in summer 2016, analysis of which would close the gap between *Schaffer et al.* (2017) and the research presented in this thesis.

Acknowledgements

References

The GEBCO_08 Grid, version 20100927, http://www.gebco.net.

SBE 911plus Brochure, Sea-Bird Scientific, http://www.seabird.com/document/sbe-911plus-brochure, 2016.

Aagaard, K., and L. K. Coachman, The East Greenland Current north of Denmark Strait: Part I, *Arctic*, pp. 181–200, 1968.

Aagaard, K., J. Swift, and E. Carmack, Thermohaline circulation in the Arctic Mediterranean seas, *Journal of Geophysical Research: Oceans*, *90*(C3), 4833–4846, 1985.

Aagaard, K., A. Foldvik, and S. Hillman, The West Spitsbergen Current: disposition and water mass transformation, *Journal of Geophysical Research: Oceans*, *92*(C4), 3778–3784, 1987.

Aksenov, Y., S. Bacon, A. C. Coward, and A. G. Nurser, The North Atlantic inflow to the Arctic Ocean: High-resolution model study, *Journal of Marine Systems*, *79*(1), 1–22, 2010.

Bacon, S., G. Reverdin, I. G. Rigor, and H. M. Snaith, A freshwater jet on the east Greenland shelf, *Journal of Geophysical Research: Oceans*, *107*(C7), 2002.

Bacon, S., A. Marshall, N. P. Holliday, Y. Aksenov, and S. R. Dye, Seasonal variability of the east greenland coastal current, *Journal of Geophysical Research: Oceans*, *119*(6), 3967–3987, 2014.

Bamber, J., et al., A new bed elevation dataset for Greenland, *The Cryosphere*, *7*(2), 499–510, 2013.

Beszczynska-Möller, A., E. Fahrbach, U. Schauer, and E. Hansen, Variability in Atlantic water temperature and transport at the entrance to the Arctic Ocean, 1997–2010, *ICES Journal of Marine Science: Journal du Conseil*, *69*(5), 852–863, 2012.

Bourke, R., A. Weigel, and R. Paquette, The westward turning branch of the West Spitsbergen Current, *Journal of Geophysical Research: Oceans*, *93*(C11), 14,065–14,077, 1988.

Bourke, R. H., J. L. Newton, R. G. Paquette, and M. D. Tunnicliffe, Circulation and water masses of the East Greenland Shelf, *Journal of Geophysical Research: Oceans*, *92*(C7), 6729–6740, 1987.

Bryden, H. L., New polynomials for thermal expansion, adiabatic temperature gradient and potential temperature of sea water, in *Deep Sea Research and Oceanographic Abstracts*, vol. 20, pp. 401–408, Elsevier, 1973.

Budéus, G., and W. Schneider, On the hydrography of the Northeast Water Polynya, *Journal of Geophysical Research: Oceans*, *100*(C3), 4287–4299, 1995.

Budéus, G., W. Schneider, and G. Kattner, Distribution and exchange of water masses in the Northeast Water Polynya (Greenland Sea), *Journal of marine systems*, *10*(1-4), 123–138, 1997.

Cottier, F. R., and E. J. Venables, On the double-diffusive and cabbeling environment of the Arctic Front, West Spitsbergen, *Polar Research*, *26*(2), 152–159, 2007.

Curry, R., and C. Mauritzen, Dilution of the northern North Atlantic Ocean in recent decades, *Science*, *308*(5729), 1772–1774, 2005.

de Steur, L., E. Hansen, R. Gerdes, M. Karcher, E. Fahrbach, and J. Holfort, Freshwater fluxes in the East Greenland Current: A decade of observations, *Geophysical Research Letters*, *36*(23), 2009.

de Steur, L., E. Hansen, C. Mauritzen, A. Beszczynska-Möller, and E. Fahrbach, Impact of recirculation on the East Greenland Current in Fram Strait: Results from moored current meter measurements between 1997 and 2009, *Deep Sea Research*, *92*, 26–40, 2014.

Dickson, B., et al., The overflow flux west of Iceland: variability, origins and forcing, in *Arctic–Subarctic Ocean Fluxes*, pp. 443–474, Springer, 2008.

Dickson, R. R., and J. Brown, The production of North Atlantic Deep Water: sources, rates, and pathways, *Journal of Geophysical Research: Oceans*, *99*(C6), 12,319–12,341, 1994.

Dorschel, B., and L. Jensen, Swath sonar bathymetry during POLARSTERN cruise PS100 (ARK-XXX/2) with links to multibeam raw data files, doi: 10.1594/PANGAEA.871076, 2017.

Eveleth, R., M.-L. Timmermans, and N. Cassar, Physical and biological controls on oxygen saturation variability in the upper Arctic Ocean, *Journal of Geophysical Research: Oceans*, *119*(11), 7420–7432, 2014.

Fahrbach, E., J. Meincke, S. Østerhus, G. Rohardt, U. Schauer, V. Tverberg, and J. Verduin, Direct measurements of volume transports through Fram Strait, *Polar Research*, *20*(2), 217–224, 2001.

Falck, E., Contribution of waters of Atlantic and Pacific origin in the Northeast Water Polynya, *Polar research*, *20*(2), 193–200, 2001.

Falck, E., G. Kattner, and G. Budéus, Disappearance of Pacific water in the northwestern Fram Strait, *Geophysical research letters*, *32*(14), 2005.

Fieg, K., R. Gerdes, E. Fahrbach, A. Beszczynska-Möller, and U. Schauer, Simulation of oceanic volume transports through Fram Strait 1995–2005, *Ocean Dynamics*, *60*(3), 491–502, 2010.

Fischer, J., and M. Visbeck, Deep velocity profiling with self-contained ADCPs, *Journal of Atmospheric and Oceanic Technology*, *10*(5), 764–773, 1993.

Fofonoff, N. P., and R. Millard Jr, Algorithms for the computation of fundamental properties of seawater., *Unesco technical papers in marine science 44*, UNESCO, 1983.

Foldvik, A., K. Aagaard, and T. Tørresen, On the velocity field of the East Greenland Current, *Deep Sea Research Part A. Oceanographic Research Papers*, *35*(8), 1335–1354, 1988.

Garcia, H. E., and L. I. Gordon, Oxygen solubility in seawater: Better fitting equations, *Limnology and oceanography*, *37*(6), 1307–1312, 1992.

Gascard, J.-C., C. Kergomard, P.-F. Jeannin, and M. Fily, Diagnostic study of the Fram Strait marginal ice zone during summer from 1983 and 1984 Marginal Ice Zone Experiment Lagrangian observations, *Journal of Geophysical Research: Oceans*, *93*(C4), 3613–3641, 1988.

Gascard, J.-C., C. Richez, and C. Rouault, New insights on large-scale oceanography in Fram Strait: The West Spitsbergen Current, *Arctic Oceanography: Marginal Ice Zones and Continental Shelves*, pp. 131–182, 1995.

Gascard, J.-C., A. J. Watson, M.-J. Messias, K. A. Olsson, T. Johannessen, and K. Simonsen, Long-lived vortices as a mode of deep ventilation in the Greenland Sea, *Nature*, *416*(6880), 525–527, 2002.

Halvorsen, M., L. Smedsrud, R. Zhang, and K. Kloster, Fram Strait spring ice export and September Arctic sea ice, *Cryosphere Discuss*, *9*(4), 4205–4235, 2015.

Hanzlick, D. J., The West Spitsbergen Current: Transport, Forcing, and Variability., Ph.D. thesis, University of Washington, 1983.

Harden, B. E., F. Straneo, and D. A. Sutherland, Moored observations of synoptic and seasonal variability in the East Greenland Coastal Current, *Journal of Geophysical Research: Oceans*, *119*(12), 8838–8857, 2014.

Harden, B. E., et al., Upstream sources of the Denmark Strait Overflow: Observations from a high-resolution mooring array, *Deep Sea Research Part I: Oceanographic Research Papers*, *112*, 94–112, 2016.

Hattermann, T., P. E. Isachsen, W.-J. von Appen, J. Albretsen, and A. Sundfjord, Eddy-driven recirculation of Atlantic Water in Fram Strait, *Geophysical Research Letters*, *43*, 1–9, 2016.

Håvik, L., R. Pickart, K. Våge, D. Torres, A. Thurnherr, A. Beszczynska-Möller, W. Walczowski, and W.-J. von Appen, Evolution of the East Greenland Current from Fram Strait to Denmark Strait: Synoptic measurements from summer 2012, *Journal of Geophysical Research: Oceans*, 2017.

Helm, V., A. Humbert, and H. Miller, Elevation and elevation change of Greenland and Antarctica derived from CryoSat-2, *The Cryosphere*, *8*(4), 1539–1559, 2014.

Holland, D. M., R. H. Thomas, B. De Young, M. H. Ribergaard, and B. Lyberth, Acceleration of Jakobshavn Isbrae triggered by warm subsurface ocean waters, *Nature Geoscience*, *1*(10), 659–664, 2008.

Hopkins, T. S., The GIN Sea—a synthesis of its physical oceanography and literature review 1972–1985, *Earth-Science Reviews*, *30*(3), 175–318, 1991.

Howat, I. M., I. Joughin, and T. A. Scambos, Rapid changes in ice discharge from Greenland outlet glaciers, *Science*, *315*(5818), 1559–1561, 2007.

Howat, I. M., I. Joughin, M. Fahnestock, B. E. Smith, and T. A. Scambos, Synchronous retreat and acceleration of southeast Greenland outlet glaciers 2000–06: Ice dynamics and coupling to climate, *Journal of Glaciology*, *54*(187), 646–660, 2008.

Ilicak, M., et al., An assessment of the Arctic Ocean in a suite of interannual CORE-II simulations. Part II: Liquid freshwater, *Ocean Modelling*, *99*, 86–109, 2016.

Ivanov, V., V. Alexeev, N. V. Koldunov, I. Repina, A. B. Sandø, L. H. Smedsrud, and A. Smirnov, Arctic Ocean Heat Impact on Regional Ice Decay: A Suggested Positive Feedback, *Journal of Physical Oceanography*, *46*(5), 1437–1456, 2016.

Jakobsson, M., et al., The international bathymetric chart of the Arctic Ocean (IBCAO) version 3.0, *Geophysical Research Letters*, *39*(12), 2012.

Jeansson, E., S. Jutterström, B. Rudels, L. G. Anderson, K. A. Olsson, E. P. Jones, W. M. Smethie, and J. H. Swift, Sources to the East Greenland Current and its contribution to the Denmark Strait Overflow, *Progress in Oceanography*, *78*(1), 12–28, 2008.

Jenkins, W. J., ^{3}H and ^{3}He in the Beta Triangle: Observations of gyre ventilation and oxygen utilization rates, *Journal of Physical Oceanography*, *17*(6), 763–783, 1987.

Johannessen, J., et al., Mesoscale eddies in the Fram Strait marginal ice zone during the 1983 and 1984 Marginal Ice Zone Experiments, *Journal of Geophysical Research: Oceans*, *92*(C7), 6754–6772, 1987.

Johannessen, O., J. Johannessen, B. Farrelly, K. Kloster, and R. Shuchman, Eddy studies during MIZEX 83 by ship and remote sensing observations, in *Proceedings of the 1984 International Geo-science and Remote Sensing Symposium, Eur. Space Agency Spec. Publ., ESASP-215*, vol. 365, p. 368, 1984.

Johnson, M., and H. Niebauer, The 1992 summer circulation in the Northeast Water Polynya from acoustic Doppler current profiler measurements, *Journal of Geophysical Research: Oceans*, *100*(C3), 4301–4307, 1995.

Jónsson, S., A. Foldvik, and K. Aagaard, The structure and atmospheric forcing of the mesoscale velocity field in Fram Strait, *Journal of Geophysical Research: Oceans*, *97*(C8), 12,585–12,600, 1992.

Joughin, I., B. Smith, I. Howat, and T. Scambos, MEaSUREs Greenland Ice Velocity Map from InSAR Data, Boulder, Colorado, USA: NASA DAAC at the National Snow and Ice Data Center, doi:10.5067/MEASURES/CRYOSPHERE/nsidc-0478.001, 2010.

Kanzow, T., The Expedition PS100 of the Research Vessel POLARSTERN to the Fram Strait in 2016, *Tech. Rep. 705*, Alfred-Wegener-Institut, Helmholtz–Zentrum für Polar– und Meeresforschung, reports on Polar and Marine Research, http://hdl.handle.net/10013/epic.50192, 2017.

Kanzow, T., and H. Witte, Raw data of continuous VM-ADCP (vessel-mounted Acoustic Doppler Current Profiler) profile during POLARSTERN cruise PS100 (ARK-XXX/2), doi:10.1594/PANGAEA.867798, 2016.

Kanzow, T., W.-J. von Appen, J. Schaffer, E. Köhn, T. Tsubouchi, N. Wilson, P. F. Lodeiro, F. Evers, and A. Wisotzki, Physical oceanography measured with ultra clean CTD/Watersampler-system during POLARSTERN cruise PS100 (ARK-XXX/2), doi: 10.1594/PANGAEA.871030, 2017a.

Kanzow, T., W.-J. von Appen, J. Schaffer, E. Köhn, T. Tsubouchi, N. Wilson, and A. Wisotzki, Physical oceanography measured with CTD/Large volume Watersampler-system during POLARSTERN cruise PS100 (ARK-XXX/2), doi: 10.1594/PANGAEA.871025, 2017b.

Karcher, M. J., R. Gerdes, F. Kauker, and C. Köberle, Arctic warming: Evolution and spreading of the 1990s warm event in the Nordic seas and the Arctic Ocean, *Journal of Geophysical Research: Oceans*, *108*(C2), 2003.

Karstensen, J., and M. Tomczak, Age determination of mixed water masses using CFC and oxygen data, *Journal of Geophysical Research: Oceans*, *103*(C9), 18,599–18,609, 1998.

Kawasaki, T., and H. Hasumi, The inflow of Atlantic water at the Fram Strait and its interannual variability, *Journal of Geophysical Research: Oceans*, 2016.

Khan, S. A., et al., Sustained mass loss of the northeast Greenland ice sheet triggered by regional warming, *Nature Climate Change*, *4*(4), 292–299, 2014.

Langehaug, H. R., and E. Falck, Changes in the properties and distribution of the intermediate and deep waters in the Fram Strait, *Progress in Oceanography*, *96*(1), 57–76, 2012.

Loose, B., W. McGillis, P. Schlosser, D. Perovich, and T. Takahashi, Effects of freezing, growth, and ice cover on gas transport processes in laboratory seawater experiments, *Geophysical Research Letters*, *36*(5), 2009.

Manley, T., Branching of Atlantic Water within the Greenland-Spitsbergen Passage: An estimate of recirculation, *Journal of Geophysical Research: Oceans*, *100*(C10), 20,627–20,634, 1995.

Manley, T., R. Bourke, and K. Hunkins, Near-surface circulation over the Yermak Plateau in northern Fram Strait, *Journal of Marine Systems*, *3*(1-2), 107–125, 1992.

Marnela, M., B. Rudels, K. A. Olsson, L. G. Anderson, E. Jeansson, D. J. Torres, M.-J. Messias, J. H. Swift, and A. J. Watson, Transports of Nordic Seas water masses and excess SF 6 through Fram Strait to the Arctic Ocean, *Progress in Oceanography*, *78*(1), 1–11, 2008.

Marnela, M., B. Rudels, M.-N. Houssais, A. Beszczynska-Möller, and P. Eriksson, Recirculation in the Fram Strait and transports of water in and north of the Fram Strait derived from CTD data, *Ocean Science*, *9*, 499–519, 2013.

Marnela, M., B. Rudels, I. Goszczko, A. Beszczynska-Möller, and U. Schauer, Fram Strait and Greenland Sea transports, water masses, and water mass transformations 1999–2010 (and beyond), *Journal of Geophysical Research: Oceans*, *121*(4), 2314–2346, 2016.

Maslowski, W., D. Marble, W. Walczowski, U. Schauer, J. L. Clement, and A. J. Semtner, On climatological mass, heat, and salt transports through the Barents Sea and Fram Strait from a pan-Arctic coupled ice-ocean model simulation, *Journal of Geophysical Research: Oceans*, *109*(C3), 2004.

Mauritzen, C., Production of dense overflow waters feeding the North Atlantic across the Greenland-Scotland Ridge. Part 1: Evidence for a revised circulation scheme, *Deep Sea Research Part I: Oceanographic Research Papers*, *43*(6), 769–806, 1996.

Mayer, C., N. Reeh, F. Jung-Rothenhäusler, P. Huybrechts, and H. Oerter, The subglacial cavity and implied dynamics under Nioghalvfjerdsfjorden Glacier, NE-Greenland, *Geophysical Research Letters*, *27*(15), 2289–2292, 2000.

Meinen, C. S., D. R. Watts, and R. A. Clarke, Absolutely referenced geostrophic velocity and transport on a section across the North Atlantic Current, *Deep Sea Research Part I: Oceanographic Research Papers*, *47*(2), 309–322, 2000.

Moon, T., and I. Joughin, Changes in ice front position on Greenland's outlet glaciers from 1992 to 2007, *Journal of Geophysical Research: Earth Surface (2003–2012)*, *113*(F2), 2008.

Moore, R., and D. Wallace, A relationship between heat transfer to sea ice and temperature-salinity properties of Arctic Ocean waters, *Journal of Geophysical Research*, *93*(C1), 565–571, 1988.

Mouginot, J., E. Rignot, B. Scheuchl, I. Fenty, A. Khazendar, M. Morlighem, A. Buzzi, and J. Paden, Fast retreat of Zachariæ Isstrøm, northeast Greenland, *Science*, *350*(6266), 1357–1361, 2015.

Murray, T., et al., Ocean regulation hypothesis for glacier dynamics in southeast Greenland and implications for ice sheet mass changes, *Journal of Geophysical Research: Earth Surface (2003–2012)*, *115*(F3), 2010.

Nick, F. M., A. Vieli, I. M. Howat, and I. Joughin, Large-scale changes in Greenland outlet glacier dynamics triggered at the terminus, *Nature Geoscience*, *2*(2), 110–114, 2009.

Niebauer, H., and W. O. Smith, A numerical model of mesoscale physical-biological interactions in the Fram Strait marginal ice zone, *Journal of Geophysical Research: Oceans*, *94*(C11), 16,151–16,175, 1989.

Nilsen, F., B. Gjevik, and U. Schauer, Cooling of the West Spitsbergen Current: Isopycnal diffusion by topographic vorticity waves, *Journal of Geophysical Research: Oceans*, *111*(C8), 2006.

Nilsson, J., G. Björk, B. Rudels, P. Winsor, and D. Torres, Liquid freshwater transport and Polar Surface Water characteristics in the East Greenland Current during the AO-02 Oden expedition, *Progress in Oceanography*, *78*(1), 45–57, 2008.

Osinski, R., The misalignment angle in vessel-mounted ADCP, *Oceanologia*, *42*(3), 2000.

Osinski, R., P. Wieczorek, A. Beszczynska-Möller, and I. Goszczko, ADCP-referenced geostrophic velocity and transport in the West Spitsbergen Current, *Oceanologia*, *45*(3), 2003.

Padman, L., and S. Erofeeva, A barotropic inverse tidal model for the Arctic Ocean, *Geophysical Research Letters*, *31*(2), 2004.

Paquette, R. G., R. H. Bourke, J. F. Newton, and W. F. Perdue, The East Greenland polar front in autumn, *Journal of Geophysical Research: Oceans*, *90*(C3), 4866–4882, 1985.

Perkin, R., and E. Lewis, Mixing in the West Spitsbergen Current, *Journal of Physical Oceanography*, *14*(8), 1315–1325, 1984.

Piechura, J., and W. Walczowski, Warming of the West Spitsbergen Current and sea ice north of Svalbard, *Oceanologia*, *51*(2), 147–164, 2009.

Piechura, J., A. Beszczynska-Möller, and R. Osinski, Volume, heat and salt transport by the West Spitsbergen Current, *Polar Research*, *20*(2), 233–240, 2001.

Polyakov, I. V., et al., Arctic Ocean warming contributes to reduced polar ice cap, *Journal of Physical Oceanography*, *40*(12), 2743–2756, 2010.

Polyakov, I. V., et al., Fate of early 2000s Arctic warm water pulse, *Bulletin of the American Meteorological Society*, *92*(5), 561–566, 2011.

Quadfasel, D., J.-C. Gascard, and K.-P. Koltermann, Large-scale oceanography in Fram Strait during the 1984 Marginal Ice Zone Experiment, *Journal of Geophysical Research: Oceans*, *92*(C7), 6719–6728, 1987.

Reeh, N., H. H. Thomsen, A. K. Higgins, and A. Weidick, Sea ice and the stability of north and northeast Greenland floating glaciers, *Annals of Glaciology*, *33*(1), 474–480, 2001.

Rhein, M., et al., Observations: Ocean, in *Climate Change 2013: The Physical Science Basis. Contribution of Working Group I to the Fifth Assessment Report of the Intergovernmental Panel on Climate Change*, edited by T. Stocker, D. Qin, G.-K. Plattner, M. Tignor, S. Allen, J. Boschung, A. Nauels, Y. Xia, V. Bex, and P. Midgley, pp. 255–315, Cambridge University Press, Cambridge, United Kingdom and New York, NY, USA, 2013.

Rignot, E., and P. Kanagaratnam, Changes in the velocity structure of the Greenland Ice Sheet, *Science*, *311*(5763), 986–990, 2006.

Rignot, E., and J. Mouginot, Ice flow in Greenland for the international polar year 2008–2009, *Geophysical Research Letters*, *39*(11), 2012.

Rudels, B., *On the mass balance of the Polar Ocean, with special emphasis on the Fram Strait*, 1987.

Rudels, B., The formation of Polar Surface Water, the ice export and the exchanges through the Fram Strait, *Progress in Oceanography*, *22*(3), 205–248, 1989.

Rudels, B., and D. Quadfasel, Convection and deep water formation in the Arctic Ocean-Greenland Sea system, *Journal of Marine Systems*, *2*(3-4), 435–450, 1991.

Rudels, B., L. Anderson, and E. Jones, Formation and evolution of the surface mixed layer and halocline of the Arctic Ocean, *Journal of Geophysical Research: Oceans*, *101*(C4), 8807–8821, 1996.

Rudels, B., E. Fahrbach, J. Meincke, G. Budéus, and P. Eriksson, The East Greenland Current and its contribution to the Denmark Strait overflow, *ICES Journal of Marine Science: Journal du Conseil*, *59*(6), 1133–1154, 2002.

Rudels, B., G. Björk, J. Nilsson, P. Winsor, I. Lake, and C. Nohr, The interaction between waters from the Arctic Ocean and the Nordic Seas north of Fram Strait and along the East Greenland Current: results from the Arctic Ocean-02 Oden expedition, *Journal of Marine Systems*, *55*(1), 1–30, 2005.

Rudels, B., M. Marnela, and P. Eriksson, Constraints on Estimating Mass, Heat and Freshwater Transports in the Arctic Ocean: An Exercise, in *Arctic–Subarctic Ocean Fluxes*, pp. 315–341, Springer, 2008.

Rudels, B., M. Korhonen, G. Budéus, A. Beszczynska-Möller, U. Schauer, A. Nummelin, D. Quadfasel, and H. Valdimarsson, The East Greenland Current and its impacts on the Nordic Seas: observed trends in the past decade, *ICES Journal of Marine Science: Journal du Conseil*, *69*(5), 841–851, 2012.

Rudels, B., M. Korhonen, U. Schauer, S. Pisarev, B. Rabe, and A. Wisotzki, Circulation and transformation of Atlantic water in the Eurasian Basin and the contribution of the Fram Strait inflow branch to the Arctic Ocean heat budget, *Progress in Oceanography*, *132*, 128–152, 2015.

Ryder, C., Den Østgrønlandske expedition udført i aarene 1891–92, V, hydrografiske undersøgelser, in *Meddelelser om Grønland*, 17, pp. 191–221, Commissionen for Ledelsen af de geologiske og geographiske Undersøgelser i Grønland, 1895.

Sabine, C. L., et al., The oceanic sink for anthropogenic CO_2, *Science*, *305*(5682), 367–371, 2004.

Saloranta, T. M., and P. M. Haugan, Northward cooling and freshening of the warm core of the West Spitsbergen Current, *Polar Research*, *23*(1), 79–88, 2004.

Schaffer, J., R. Timmermann, J. E. Arndt, S. S. Kristensen, C. Mayer, M. Morlighem, and D. Steinhage, A global, high-resolution data set of ice sheet topography, cavity geometry, and ocean bathymetry, *Earth System Science Data*, *8*(2), 543–557, doi: 10.5194/essd-8-543-2016, 2016.

Schaffer, J., W.-J. von Appen, P. A. Dodd, C. Hofstede, C. Mayer, L. de Steur, and T. Kanzow, Warm water pathways toward Nioghalvfjerdsfjorden Glacier, Northeast Greenland, *Journal of Geophysical Research: Oceans*, 2017.

Schauer, U., R. D. Muench, B. Rudels, and L. Timokhov, Impact of eastern Arctic shelf waters on the Nansen Basin intermediate layers, *Journal of Geophysical Research, 102,* 3371–3382, 1997.

Schauer, U., E. Fahrbach, S. Osterhus, and G. Rohardt, Arctic warming through the Fram Strait: Oceanic heat transport from 3 years of measurements, *Journal of Geophysical Research: Oceans, 109*(C6), 2004.

Schauer, U., A. Beszczynska-Möller, W. Walczowski, E. Fahrbach, J. Piechura, and E. Hansen, Variation of measured heat flow through the Fram Strait between 1997 and 2006, in *Arctic–Subarctic Ocean Fluxes,* pp. 65–85, Springer, 2008.

Schlichtholz, P., and M.-N. Houssais, An inverse modeling study in Fram Strait. Part I: dynamics and circulation, *Deep Sea Research Part II: Topical Studies in Oceanography, 46*(6), 1083–1135, 1999a.

Schlichtholz, P., and M.-N. Houssais, An inverse modeling study in Fram Strait. Part II: water mass distribution and transports, *Deep Sea Research Part II: Topical Studies in Oceanography, 46*(6), 1137–1168, 1999b.

Schlichtholz, P., and M.-N. Houssais, An overview of the teta-S correlations in Fram Strait based on the MIZEX 84 data, *Oceanologia, 44*(2), 2002.

Schneider, W., and G. Budéus, On the generation of the Northeast Water Polynya, *Journal of Geophysical Research: Oceans, 100*(C3), 4269–4286, 1995.

Smith, D. C., J. Morison, J. Johannessen, and N. Untersteiner, Topographic generation of an eddy at the edge of the East Greenland Current, *Journal of Geophysical Research: Oceans, 89*(C5), 8205–8208, 1984.

Smith, S. L., W. O. Smith, L. A. Codispoti, and D. L. Wilson, Biological observations in the marginal ice zone of the East Greenland Sea, *Journal of marine research, 43*(3), 693–717, 1985.

Smith, W., and P. Wessel, Gridding with continuous curvature splines in tension, *Geophysics, 55*(3), 293–305, 1990.

Spitzer, W. S., and W. J. Jenkins, Rates of vertical mixing, gas exchange and new production: Estimates from seasonal gas cycles in the upper ocean near Bermuda, *Journal of Marine Research, 47*(1), 169–196, 1989.

Straneo, F., and P. Heimbach, North Atlantic warming and the retreat of Greenland's outlet glaciers, *Nature*, *504*(7478), 36–43, 2013.

Sutherland, D. A., and R. S. Pickart, The East Greenland coastal current: Structure, variability, and forcing, *Progress in Oceanography*, *78*(1), 58–77, 2008.

Swift, J. H., and K. Aagaard, Seasonal transitions and water mass formation in the Iceland and Greenland seas, *Deep Sea Research Part A. Oceanographic Research Papers*, *28*(10), 1107–1129, 1981.

Teigen, S. H., F. Nilsen, R. Skogseth, and B. Gjevik, Barotropic instability in the West Spitsbergen Current, *Journal of Geophysical Research*, *115*, 35–52, 2010.

Teigen, S. H., F. Nilsen, R. Skogseth, B. Gjevik, and A. Beszczynska-Möller, Baroclinic instability in the West Spitsbergen Current, *Journal of Geophysical Research: Oceans*, *116*(C7), 2011.

Thomas, R., E. Frederick, W. Krabill, S. Manizade, and C. Martin, Recent changes on Greenland outlet glaciers, *Journal of Glaciology*, *55*(189), 147–162, 2009.

Thurnherr, A., A practical assessment of the errors associated with full-depth LADCP profiles obtained using Teledyne RDI Workhorse acoustic Doppler current profilers, *Journal of Atmospheric and Oceanic Technology*, *27*(7), 1215–1227, 2010.

Topp, R., and M. Johnson, Winter intensification and water mass evolution from year-long current meters in the Northeast Water Polynya, *Journal of marine systems*, *10*(1-4), 157–173, 1997.

Torres-Valdés, S., et al., Export of nutrients from the Arctic Ocean, *Journal of Geophysical Research: Oceans*, *118*(4), 1625–1644, 2013.

Våge, K., R. S. Pickart, M. A. Spall, G. Moore, H. Valdimarsson, D. J. Torres, S. Y. Erofeeva, and J. E. Ø. Nilsen, Revised circulation scheme north of the Denmark Strait, *Deep Sea Research Part I: Oceanographic Research Papers*, *79*, 20–39, 2013.

Visbeck, M., Deep velocity profiling using lowered acoustic Doppler current profilers: Bottom track and inverse solutions, *Journal of Atmospheric and Oceanic Technology*, *19*(5), 794–807, 2002.

von Appen, W.-J., U. Schauer, R. Somavilla, E. Bauerfeind, and A. Beszczynska-Möller, Exchange of warming deep waters across Fram Strait, *Deep Sea Research*, *103*, 86–100, 2015.

von Appen, W.-J., U. Schauer, T. Hattermann, and A. Beszczynska-Möller, Seasonal cycle of mesoscale instability of the West Spitsbergen Current, *Journal of Physical Oceanography*, *46*(4), 1231–1254, 2016.

von Appen, W.-J., T. Kanzow, and J. Schaffer, Lowered Acoustic Doppler Current Profiler (LADCP) raw data collected during POLARSTERN cruise PS100, doi: 10.1594/PANGAEA.870995, 2017.

von Appen, W.-J., et al., The East Greenland Spill Jet as an important component of the Atlantic meridional overturning circulation, *Deep Sea Research Part I: Oceanographic Research Papers*, *92*, 75–84, 2014.

Wadhams, P., and V. Squire, An ice-water vortex at the edge of the East Greenland Current, *Journal of Geophysical Research: Oceans*, *88*(C5), 2770–2780, 1983.

Walczowski, W., Frontal structures in the West Spitsbergen Current margins, *Ocean Science*, *9*(6), 957, 2013.

Walczowski, W., A. Beszczynska-Möller, P. Wieczorek, M. Merchel, and A. Grynczel, Oceanographic observations in the Nordic Sea and Fram Strait in 2016 under the IOPAN long-term monitoring program AREX, *Oceanologia*, 2017.

Wekerle, C., Q. Wang, W.-J. von Appen, S. Danilov, V. Schourup-Kristensen, and T. Jung, Eddy-resolving simulation of the Atlantic Water circulation in the Fram Strait with focus on the seasonal cycle, *Journal of Geophysical Research, Oceans*, submitted, 2017.

Wilson, N. J., and F. Straneo, Water exchange between the continental shelf and the cavity beneath Nioghalvfjerdsbræ (79 North Glacier), *Geophysical Research Letters*, *42*(18), 7648–7654, 2015.

Woodgate, R. A., E. Fahrbach, and G. Rohardt, Structure and transports of the East Greenland Current at 75 N from moored current meters, *Journal of Geophysical Research: Oceans*, *104*(C8), 18,059–18,072, 1999.

Yang, Q., T. H. Dixon, P. G. Myers, J. Bonin, D. Chambers, and M. Van Den Broeke, Recent increases in Arctic freshwater flux affects Labrador Sea convection and Atlantic overturning circulation, *Nature Communications*, *7*, 2016.

Table 4: Information on stations during PS100 from *Kanzow* (2017). Locations can be seen in Figure 2. CTD/L stands for large volume CTD, CTD/UC stands for ultra-clean CTD. An x in the column 'grid' marks the casts used for the gridded sections.

Section	Station-Cast	Date Time	Lat	Lon	Depth [m]	CTD/L	CTD/UC	Grid
0°EW	PS100/290-2	02-Sep-2016 12:35:00	77.833°N	0.0003°W	3053	1		x
0°EW	PS100/106-2	09-Aug-2016 14:44:00	78.1613°N	0.039°W	1001	1		x
0°EW	PS100/105-1	09-Aug-2016 08:39:00	78.501°N	0.0018°W	1001	1		x
0°EW	PS100/039-1	27-Jul-2016 08:47:00	78.8343°N	0.0002°W	2578	1		x
0°EW	PS100/043-1	28-Jul-2016 02:31:00	79.1668°N	0.0312°E	1200	1		x
0°EW	PS100/046-1	29-Jul-2016 02:26:00	79.4997°N	0.0813°E	2762	1		x
0°EW	PS100/048-1	29-Jul-2016 19:58:00	80.1563°N	0.2875°E	2990	1		x
0°EW	PS100/049-1	30-Jul-2016 06:03:00	80.5018°N	0.1767°E	1201	1		x
0°EW	PS100/052-4	31-Jul-2016 07:10:00	80.7113°N	0.1522°E	300	1		
0°EW	PS100/050-1	30-Jul-2016 13:47:00	80.7138°N	0.128°W	101		1	
0°EW	PS100/052-2	30-Jul-2016 23:02:00	80.7505°N	0.0865°E	3153	1		x
0°EW	PS100/053-2	31-Jul-2016 14:28:00	80.8532°N	0.2058°W	3121		1	x
~79°N	PS100/090-2	05-Aug-2016 22:05:00	78.831°N	11.9998°W	194	1		x
~79°N	PS100/091-1	06-Aug-2016 00:59:00	78.8347°N	11.0017°W	319	1		x
~79°N	PS100/092-1	06-Aug-2016 04:59:00	78.8397°N	9.9832°W	253	1		x
~79°N	PS100/093-1	06-Aug-2016 07:40:00	78.8033°N	8.9392°W	201	1		x
~79°N	PS100/094-2	06-Aug-2016 10:35:00	78.678°N	7.9433°W	166	1		x
~79°N	PS100/095-1	06-Aug-2016 13:42:00	78.6798°N	7.0052°W	213	1		x
~79°N	PS100/096-1	06-Aug-2016 18:13:00	78.765°N	5.9892°W	313	1		x
~79°N	PS100/097-1	06-Aug-2016 21:41:00	78.8128°N	5.0068°W	951	1		x
~79°N	PS100/285-1	31-Aug-2016 20:02:00	78.8015°N	4.9693°W	976	1		

Table 4: Information on stations during PS100 from *Kanzow* (2017). Locations can be seen in Figure 2. CTD/L stands for large volume CTD, CTD/UC stands for ultra-clean CTD. An x in the column 'grid' marks the casts used for the gridded sections.

~79°N	PS100/285-3	01-Sep-2016 02:22:00	78.7227°N 4.9005°W	151	1	
~79°N	PS100/288-2	01-Sep-2016 19:08:00	78.806°N 4.1932°W	1688	1	
~79°N	PS100/098-1	07-Aug-2016 03:56:00	78.8445°N 4.0215°W	1865	1	x
~79°N	PS100/101-4	08-Aug-2016 00:34:00	78.6775°N 3.668°W	301	1	
~79°N	PS100/101-2	07-Aug-2016 17:37:00	78.7767°N 3.5502°W	2150	1	x
~79°N	PS100/102-2	08-Aug-2016 06:16:00	78.8557°N 2.5993°W	2548	1	x
~79°N	PS100/103-5	09-Aug-2016 03:16:00	78.7965°N 2.5225°W	301	1	
~79°N	PS100/103-3	08-Aug-2016 19:39:00	78.8027°N 2.2197°W	2634	1	x
~79°N	PS100/042-2	27-Jul-2016 21:21:00	78.8352°N 0.8893°W	2590	1	x
~79°N	PS100/039-1	27-Jul-2016 08:47:00	78.8343°N 0.0002°W	2578	1	x
~79°N	PS100/044-4	28-Jul-2016 16:32:00	78.8272°N 1.0887°E	301	1	
~79°N	PS100/044-2	28-Jul-2016 09:04:00	78.8298°N 1.0978°E	2459	1	x
~79°N	PS100/038-1	27-Jul-2016 04:05:00	78.8402°N 2.2472°E	2470	1	x
~79°N	PS100/037-4	27-Jul-2016 00:55:00	78.8338°N 3.5003°E	310	1	
~79°N	PS100/037-2	26-Jul-2016 17:54:00	78.8335°N 3.5063°E	2280	1	x
~79°N	PS100/035-1	26-Jul-2016 03:12:00	78.8285°N 4.251°E	2366	1	x
~79°N	PS100/033-2	25-Jul-2016 20:29:00	78.8183°N 5.0°E	2630	1	x
~79°N	PS100/034-1	25-Jul-2016 23:43:00	78.9192°N 5.3382°E	2527	1	x
~79°N	PS100/019-2	23-Jul-2016 19:00:00	78.9905°N 5.6677°E	2123	1	x
~79°N	PS100/020-1	23-Jul-2016 21:39:00	79.0002°N 6.5002°E	1384	1	x
~79°N	PS100/028-4	25-Jul-2016 02:51:00	78.987°N 6.993°E	200	1	
~79°N	PS100/028-2	24-Jul-2016 20:38:00	78.986°N 6.9943°E	1185	1	x
~79°N	PS100/021-2	24-Jul-2016 02:06:00	79.0007°N 7.502°E	1213	1	x

Table 4: Information on stations during PS100 from *Kanzow* (2017). Locations can be seen in Figure 2. CTD/L stands for large volume CTD, CTD/UC stands for ultra-clean CTD. An x in the column 'grid' marks the casts used for the gridded sections.

~79°N	PS100/022-1	24-Jul-2016 04:28:00	79.0005°N	7.9972°E	1069	1		x
~79°N	PS100/015-2	22-Jul-2016 20:17:00	78.9993°N	8.328°E	770	1		x
~79°N	PS100/015-5	23-Jul-2016 03:22:00	79.0043°N	8.3282°E	100	1		
~79°N	PS100/027-1	24-Jul-2016 16:08:00	78.9937°N	8.5467°E	297	1		x
79.6°N	PS100/277-1	30-Aug-2016 08:43:00	79.5992°N	6.1723°W	288	1		x
79.6°N	PS100/278-1	30-Aug-2016 10:50:00	79.604°N	5.6363°W	344	1		x
79.6°N	PS100/279-1	30-Aug-2016 12:52:00	79.5923°N	5.1852°W	899	1		x
79.6°N	PS100/280-2	30-Aug-2016 16:24:00	79.5775°N	4.793°W	1300	1		x
79.6°N	PS100/281-1	30-Aug-2016 19:32:00	79.5865°N	4.155°W	1001	1		x
79.6°N	PS100/282-1	30-Aug-2016 21:46:00	79.6023°N	3.7252°W	2061	1		x
79.6°N	PS100/283-1	31-Aug-2016 00:49:00	79.609°N	3.3305°W	1000	1		x
WT1	PS100/082-2	04-Aug-2016 23:20:00	80.4485°N	13.1885°W	285	1		x
WT1	PS100/079-1	04-Aug-2016 15:50:00	80.4477°N	12.8462°W	266	1		x
WT1	PS100/078-1	04-Aug-2016 05:46:00	80.4302°N	12.007°W	259	1		x
WT1	PS100/077-1	04-Aug-2016 03:22:00	80.4318°N	10.9883°W	284	1		x
WT1	PS100/076-1	04-Aug-2016 00:20:00	80.3413°N	10.0032°W	309	1		x
WT1	PS100/075-1	03-Aug-2016 21:54:00	80.2508°N	9.0068°W	288	1		x
WT1	PS100/065-1	02-Aug-2016 21:14:00	80.143°N	8.2517°W	316	1		x
WT1	PS100/062-1	02-Aug-2016 16:15:00	80.1475°N	7.9533°W	302	1		x
WT1	PS100/061-1	02-Aug-2016 13:14:00	80.2045°N	6.9945°W	268	1		x
WT1	PS100/060-1	02-Aug-2016 09:36:00	80.2468°N	6.0183°W	342	1		x
WT1	PS100/059-1	02-Aug-2016 07:12:00	80.2682°N	5.4905°W	889	1		x
WT1	PS100/058-1	02-Aug-2016 02:20:00	80.2698°N	4.99°W	1453	1		x

Table 4: Information on stations during PS100 from *Kanzow* (2017). Locations can be seen in Figure 2. CTD/L stands for large volume CTD, CTD/UC stands for ultra-clean CTD. An x in the column 'grid' marks the casts used for the gridded sections.

WT1	PS100/057-1	01-Aug-2016 23:17:00	80.3037°N 4.5145°W	2032	1		x
WT1	PS100/056-2	01-Aug-2016 15:49:00	80.3308°N 4.0245°W	2505	1		x
WT1	PS100/056-5	01-Aug-2016 20:45:00	80.3203°N 3.8733°W	252	1		
WT1	PS100/055-1	01-Aug-2016 06:40:00	80.3735°N 2.899°W	1506	1		x
WT1	PS100/054-1	31-Jul-2016 22:11:00	80.3862°N 1.4778°W	2008	1		x
WT1	PS100/049-1	30-Jul-2016 06:03:00	80.5018°N 0.1767°E	1201	1		x
NT1	PS100/109-1	10-Aug-2016 20:30:00	76.8918°N 8.9298°W	362	1		x
NT1	PS100/110-1	10-Aug-2016 22:15:00	76.8332°N 8.6653°W	355	1		x
NT1	PS100/111-1	10-Aug-2016 23:27:00	76.7765°N 8.4057°W	346	1		x
NT1	PS100/112-1	11-Aug-2016 00:41:00	76.7185°N 8.1512°W	331	1		x
NT1	PS100/124-1	12-Aug-2016 04:11:00	76.6753°N 7.9568°W	325	1		x
NT1	PS100/113-1	11-Aug-2016 02:21:00	76.6315°N 7.7535°W	324	1		x
NT1	PS100/114-1	11-Aug-2016 03:29:00	76.6042°N 7.6315°W	325	1		x
NT1	PS100/115-1	11-Aug-2016 04:29:00	76.574°N 7.494°W	524	1		x
NT1	PS100/116-1	11-Aug-2016 05:55:00	76.5465°N 7.3753°W	756	1		x
NT1	PS100/117-1	11-Aug-2016 07:11:00	76.5142°N 7.2372°W	985	1		x
NT1	PS100/118-1	11-Aug-2016 09:07:00	76.4875°N 7.1167°W	1033	1		x
NT1	PS100/119-1	11-Aug-2016 10:51:00	76.4285°N 6.8572°W	1001	1		x
NT1	PS100/120-1	11-Aug-2016 13:39:00	76.3023°N 6.3118°W	2295	1		x

Further Remarks on AW definitions

When examining watermass definitions in the literature it is important to keep in mind the study area for which a definition was chosen. For example, the definition found in *Sutherland and Pickart* (2008), seen as the box between 4.5 and 6.5°C in Figure 6, concerns the EGC outflow region south of Denmark Strait, to the south of our study area. South of Denmark Strait, not all recirculating AW in the EGC was subject to as strong cooling by sea-ice and atmosphere as the AW recirculating farther north in Fram Strait. On the other hand, studies with AW definitions which include water colder than 2°C (e.g. *Rudels and Quadfasel* (1991); *Rudels et al.* (2015)) include both the Nordic Seas and the Arctic Ocean where waters of Atlantic origin have experienced significant cooling. Some definitions of AW are only interpretable in conjunction with other watermasses distinguished in a particular study. Some studies may not distinguish between AAW and AW, as done here, but rather include both in a single watermass dubbed AW (e.g. *Rudels and Quadfasel* (1991)). Other authors may have a watermass close to our definition of AW, but call it by a different name, such as 'North Atlantic Water' (*Aksenov et al.*, 2010), 'Recirculating Atlantic Water' (*Budéus et al.*, 1997; *de Steur et al.*, 2014), 'Return Atlantic Water' (*Harden et al.*, 2016) or 'warm Atlantic Water' (*Schlichtholz and Houssais*, 1999b). A list of watermass definitions in the Arctic Mediterranean can be found in Table 5. This list does not aspire to completeness but rather gives an indication of common ranges and illustrates the vast amount of definitions used.

Table 5: Table of watermass definitions in the literature. Please note that this table does not assume to be complete! Watermasses are sorted by name, if the reference gives an acronym this is also given. Note that some definitions can only be interpreted in context with other watermass boundaries given in the reference. Fp stands for freezing point. The upper and lower bounds for temperature, salinity, density and depth are given, if applicable. Further notes and boundaries can be found in the footnotes at the bottom of this table.

watermass (acronym)	T lower (°C)	T upper (°C)	S lower	S upper	σ lower	σ upper	depth lower (m)	depth upper (m)	reference	notes	origin
Arctic Atlantic Water (AAW)	0	2					500		*de Steur et al.* (2014)	adapted from *Rudels et al.* (2008)	
Arctic Atlantic Water (AAW)		0			27.7	27.97			*Marnela et al.* (2013); *Rudels et al.* (2005)	after *Rudels et al.* (2008), includes Arctic Ocean thermocline	Arctic Ocean
Arctic Atlantic Water (AAW)	0.2	0.6	34.8	34.9					*Mauritzen* (1996)		
Arctic Atlantic Water (AAW)	0	2			27.7	29.97			*Rudels et al.* (2002, 2005)		Arctic Ocean
Arctic Atlantic Water (AAW)	0				27.97	30.444 ($\sigma_{0.5}$)			*Rudels et al.* (2002, 2005)	S increasing, θ decreasing with depth	Arctic Ocean
Arctic Atlantic Water (AAW)		0		*					*Rudels et al.* (2002)		
Arctic Atlantic Water (AAW)	0.232	0.232		34.676					*Rudels et al.* (2005)	includes Arctic Ocean thermocline	Arctic Ocean
Arctic Intermediate Water (AIW)	0	3							*Foldvik et al.* (1988)		
Arctic Intermediate Water (AIW)		≈0		≈34.92					*Mauritzen* (1996)		
Arctic Intermediate Water (AIW)		0			27.97	30.444 ($\sigma_{0.5}$)			*Rudels et al.* (2002)		
Arctic Intermediate Water (AIW)		0			27.97				*Rudels et al.* (2005)	includes a salinity minimum, in the Greenland Sea also a temperature minimum	Greenland Sea
Arctic Intermediate Water (AIW)		0			30.444 ($\sigma_{0.5}$)				*Rudels et al.* (2005)	includes a salinity minimum, in the Greenland Sea also a temperature minimum	Greenland Sea

Table 5: Table of watermass definitions in the literature. Please note that this table does not assume to be complete! Watermasses are sorted by name, if the reference gives an acronym this is also given. Note that some definitions can only be interpreted in context with other watermass boundaries given in the reference. Fp stands for freezing point. The upper and lower bounds for temperature, salinity, density and depth are given, if applicable. Further notes and boundaries can be found in the footnotes at the bottom of this table.

Name	T low	T high	S low	S high	density	depth	Reference	Notes
Arctic Intermediate Water (AIW)	-0.8	0	34.9	34.92			*Schlichtholz and Houssais* (1999b, 2002)	if a salinity minimum is found in the range -1.1°C $<\theta<$ -0.5°C 34.7 $<$S$<$ 34.9
Arctic Intermediate Water (AIW)	-1.1	-0.5	34.7	34.9			*Schlichtholz and Houssais* (1999b)	
Arctic Intermediate Water (AIW)	-1.1	-0.5	34.7	34.9	∥a	550± 200	*Schlichtholz and Houssais* (2002)	
Arctic Ocean Deep Water	-0.95	0	34.93	34.95			*Rudels* (1989)	
Arctic or Atlantic Intermediate Water (AIW)	0	3	34.5	34.9			*Topp and Johnson* (1997)	
Arctic Origin Water (AOW)		0		28			*Harden et al.* (2016)	not clear if called Arctic Origin Water or Arctic Overflow Water — occupies deep basin of Nordic Seas
Arctic Surface Water (ASW)	2			34.9			*Gascard et al.* (1995)	following *Swift and Aagaard* (1981) and *Aagaard et al.* (1987) nomenclature
Arctic Surface Water (ASW)		2		34.7			*Gascard et al.* (1995)	following *Swift and Aagaard* (1981) and *Aagaard et al.* (1987) nomenclature
Arctic Surface Water (ASW)		0	34.4	34.9			*Manley et al.* (1992)	
Arctic Surface Water (ASW)	0		34.4	34.7			*Swift and Aagaard* (1981)	
Arctic Surface Water (ASW)	2		34.7	34.9			*Swift and Aagaard* (1981)	
Arctic Surface Water, Upper and Lower Arctic Intermediate Water, Atlantic Water	0						*Woodgate et al.* (1999)	

Table 5: Table of watermass definitions in the literature. Please note that this table does not assume to be complete! Watermasses are sorted by name, if the reference gives an acronym this is also given. Note that some definitions can only be interpreted in context with other watermass boundaries given in the reference. Fp stands for freezing point. The upper and lower bounds for temperature, salinity, density and depth are given, if applicable. Further notes and boundaries can be found in the footnotes at the bottom of this table.

Watermass	Temp. upper	Temp. lower	Sal. upper	Sal. lower	Dens. upper	Dens. lower	Depth	Reference	Notes	
arctic-type shelf water		4		34.9				*Cottier and Venables (2007)*	at the Arctic Front west of Spitsbergen	East Spitsbergen Current
Atlantic Intermediate Water (AIW)	0	3	34.5	34.9				*Bourke et al. (1987); Aagaard and Coachman (1968)*		
Atlantic Intermediate Water (AIW)	0	3	34.4	34.9				*Manley et al. (1992)*		
Atlantic Intermediate Water (AIW)	0		34.3					*Wilson and Straneo (2015)*		
Atlantic Layer	0						#	*Rudels (1989)*		
Atlantic Water (AW)	2							*Beszczynska-Möller et al. (2012)*		
Atlantic Water (AW)	3		34.9					*Bourke et al. (1987); Aagaard and Coachman (1968); Gascard et al. (1995); Manley et al. (1992); Manley (1995); Swift and Aagaard (1981); Topp and Johnson (1997)*	following *Aagaard et al. (1987)* nomenclature	subtropics
Atlantic Water (AW)	4		34.9					*Cottier and Venables (2007)*	at the Arctic Front west of Spitsbergen	
Atlantic Water (AW)	2						500	*de Steur et al. (2014)*	adapted from *Rudels et al. (2008)*	
Atlantic Water (AW)	3							*Foldvik et al. (1988)*		
Atlantic Water (AW)	0		34.9					*Hanzlick (1983)*		
Atlantic Water (AW)	4.1	4.1	35.15	35.15				*Håvik et al. (2017)*	endmembers in mixing triangle	
Atlantic Water (AW)	0				27.7	27.97		*Marnela et al. (2013)*	adapted from *Rudels et al. (2008)*	
Atlantic Water (AW)	3		35		27.4	27.8		*Mauritzen (1996)*		
Atlantic Water (AW)	3		35					*Quadfasel et al. (1987)*		
Atlantic Water (AW)	1		34.4					*Rudels and Quadfasel (1991)*		

Table 5: Table of watermass definitions in the literature. Please note that this table does not assume to be complete! Watermasses are sorted by name, if the reference gives an acronym this is also given. Note that some definitions can only be interpreted in context with other watermass boundaries given in the reference. Fp stands for freezing point. The upper and lower bounds for temperature, salinity, density and depth are given, if applicable. Further notes and boundaries can be found in the footnotes at the bottom of this table.

Watermass	T	T	S	S	σ	σ	Reference	Notes	
Atlantic Water (AW)	0	1	34.91				*Rudels and Quadfasel* (1991)		
Atlantic Water (AW)					27.7	27.97	*Rudels et al.* (2008)	in *Marnela et al.* (2016, 2008) equivalent Nordic Seas: AW; Arctic Ocean: AAW	
Atlantic Water (AW)	1						*Schauer et al.* (2004)		
Atlantic Water (AW)	4.5	6.5	34.8	35.1			*Sutherland and Pickart* (2008)		
Atlantic Water (AW)	2		34.9				*Topp and Johnson* (1997); *Walczowski* (2013)	after *Aagaard et al.* (1985)	
Atlantic Water (AW)	0		34.92				*Walczowski* (2013); *Walczowski et al.* (2017)		
Atlantic Water and Recirculating AW (AW/RAW)	2				27.7	27.97	*Rudels et al.* (2005)		WSC
Atlantic Water and Recirculating AW (AW/RAW)	0				27.97	30.444 $(\sigma_{0.5})$	*Rudels et al.* (2005)	S and θ decrease with depth in the WSC	WSC
Atlantic Water I	0					†	*Rudels et al.* (2015)	study area in Arctic Ocean	
Atlantic water II	0					‡	*Rudels et al.* (2015)	study area in Arctic Ocean	
Atlantic Water Masses (AW)			34				*Harden et al.* (2014)		
Canadian Basin Arctic Atlantic Water (CBAAW)	0.7	0.7	34.832	34.832			*Jeansson et al.* (2008)	§	
Canadian Basin Deep Water (CBDW)	-0.67	-0.67	34.926	34.926			*Jeansson et al.* (2008)	§	
Canadian Basin Deep Water (CBDW)			34.915		30.444 $(\sigma_{0.5})$	35.142 $(\sigma_{1.5})$	*Rudels et al.* (2002, 2005)	includes water from the Eurasian Basin	Canadian Basin

Table 5: Table of watermass definitions in the literature. Please note that this table does not assume to be complete! Watermasses are sorted by name, if the reference gives an acronym this is also given. Note that some definitions can only be interpreted in context with other watermass boundaries given in the reference. Fp stands for freezing point. The upper and lower bounds for temperature, salinity, density and depth are given, if applicable. Further notes and boundaries can be found in the footnotes at the bottom of this table.

Watermass	T low	T high	S low	S high		density	depth	Reference	Notes
Canadian Basin Deep Water (CBDW)	-0.8	-0.5	34.92					*Schlichtholz and Houssais* (1999b)	
Canadian Basin Deep Water (CBDW)	-0.8	-0.5	34.92		‖b		1500± 138	*Schlichtholz and Houssais* (2002)	
Canadian Basin Intermediate Water (CBIW)	0.17	0.17	34.878	34.878				*Jeansson et al.* (2008)	§
Canadian upper Polar Deep Water (CuPDW)	-0.34	-0.34	34.908	34.908				*Jeansson et al.* (2008)	§
cold Atlantic Water (AWc)	0	2	34.91					*Schlichtholz and Houssais* (1999b)	
cold Atlantic Water (cAW)	0	2	34.91		‖c		462± 115	*Schlichtholz and Houssais* (2002)	
Cold Deep Water (CDW)		-0.5	34.8					*Rudels and Quadfasel* (1991)	
cold Norwegian Sea Deep Water (NSDWc)	-1.1	-0.8	34.9	34.92				*Schlichtholz and Houssais* (1999b)	
cold Norwegian Sea Deep Water (NSDWc)	-1.1	-0.8	34.9	34.92	‖d		1610± 334	*Schlichtholz and Houssais* (2002)	
Deep Water (DW)		0	34.88	34.9				*Bourke et al.* (1987); *Aagaard and Coachman* (1968)	
Deep Water (DW)		0					1400	*de Steur et al.* (2014)	adapted from *Rudels et al.* (2008)
Deep Water		0					1000	*Foldvik et al.* (1988)	
Deep Water (DW)		0	34.85	34.95				*Hanzlick* (1983)	
Deep Water	-0.4	-0.4	34.915	34.015				*Håvik et al.* (2017)	endmembers in mixing triangle
Deep Water (DW)							700	*Schauer et al.* (2004)	
Deep Water 1 (DWI)					30.444 ($\sigma_{0.5}$)	35.142 ($\sigma_{1.5}$)		*Marnela et al.* (2013)	adapted from *Rudels et al.* (2008)
Deep Water 2 (DWII)					35.142 ($\sigma_{1.5}$)			*Marnela et al.* (2013)	adapted from *Rudels et al.* (2008)

Table 5: Table of watermass definitions in the literature. Please note that this table does not assume to be complete! Watermasses are sorted by name, if the reference gives an acronym this is also given. Note that some definitions can only be interpreted in context with other watermass boundaries given in the reference. Fp stands for freezing point. The upper and lower bounds for temperature, salinity, density and depth are given, if applicable. Further notes and boundaries can be found in the footnotes at the bottom of this table.

Name	T low	T high	S low	S high	ρ low	ρ high	depth	Reference	Notes
Deep Water I (DWI)					30.444 ($\sigma_{0.5}$)	35.142 ($\sigma_{1.5}$)		*Rudels et al.* (2008)	in *Marnela et al.* (2016, 2008) equivalent Nordic Seas: Nordic Seas Deep Water I (NSDWI) S < 34.915, Arctic Ocean: CBDW
Deep Water II (DWII)					35.142 ($\sigma_{1.5}$)			*Rudels et al.* (2008)	in *Marnela et al.* (2016, 2008) equivalent Nordic Seas: NSDWII, S<34.915, Arctic Ocean: EBDW
Denmark Strait Overflow Water (DSOW)	0		34.8	34.9	27.8			*Sutherland and Pickart* (2008)	
Dense Atlantic Water (dAW)	0	2					500	*de Steur et al.* (2014)	adapted from *Rudels et al.* (2008)
Dense Atlantic Water (dAW)	0				27.97	30.444 ($\sigma_{0.5}$)		*Rudels et al.* (2008); *Marnela et al.* (2013)	in *Marnela et al.* (2016, 2008) equivalent Nordic Seas: dense Atlantic water (dAW) S and θ decrease with depth; Arctic Ocean: dense Arctic Atlantic Water (dAAW) S increasing, θ decreasing with depth
Dense Overflow Water					27.8			*Håvik et al.* (2017)	rho theta
Eurasian Basin Arctic Atlantic Water (EBAAW)	1.35	1.35	34.874	34.874				*Jeansson et al.* (2008)	§
Eurasian Basin Deep Water (EBAAW)	-0.87	-0.87	34.923	34.923				*Jeansson et al.* (2008)	§
Eurasian Basin Deep Water (EBAAW)			34.915		35.142 ($\sigma_{1.5}$)	39.738 ($\sigma_{2.5}$)		*Rudels et al.* (2002)	
Eurasian Basin Deep Water (EBAAW)			34.915		35.142 ($\sigma_{1.5}$)			*Rudels et al.* (2005)	Eurasian Basin

Table 5: Table of watermass definitions in the literature. Please note that this table does not assume to be complete! Watermasses are sorted by name, if the reference gives an acronym this is also given. Note that some definitions can only be interpreted in context with other watermass boundaries given in the reference. Fp stands for freezing point. The upper and lower bounds for temperature, salinity, density and depth are given, if applicable. Further notes and boundaries can be found in the footnotes at the bottom of this table.

Watermass							Reference	
Eurasian Basin Deep Water (EBAAW)	-1.1	-0.8	34.92				*Schlichtholz and Houssais* (1999b)	
Eurasian Basin Deep Water (EBAAW)	-1.1	-0.8	34.92		‖e	2333±303	*Schlichtholz and Houssais* (2002)	
Eurasian upper Polar Deep Water (EuPDW)	-0.38	-0.38	34.904	34.904			*Jeansson et al.* (2008)	§
Eurasian Basin Bottom Water (EBBW)	-0.93	-0.93	34.937	34.937			*Jeansson et al.* (2008)	§
fresh Atlantic Water (AWf)	1		34.4	34.91			*Schlichtholz and Houssais* (1999b)	
fresh Atlantic Water (fAW)	1		34.4	34.91	‖f	71± 19	*Schlichtholz and Houssais* (2002)	
Greenland Sea Arctic Intermediate Water (GSAIW)	-0.9	-0.9	34.884	34.884			*Jeansson et al.* (2008)	§
Greenland Sea Bottom Water (GSBW)	-1.11	-1.11	34.903	34.903			*Jeansson et al.* (2008)	§
Greenland Sea Deep Water (GSDW)		-1.1	34.7	34.92			*Schlichtholz and Houssais* (1999b)	
Greenland Sea Deep Water (GSDW)		-1.1	34.7	34.92	‖g	2482± 300	*Schlichtholz and Houssais* (2002)	
Greenland Sea Deep Water (GSDW)		0	34.88	34.9			*Swift and Aagaard* (1981)	found only in central gyre of Greenland Sea
Greenland See Upper Water (GSUW)	-0.89	-0.89	34.873	34.873			*Jeansson et al.* (2008)	§
Halocline	at fp down to 100m		33	S of AW below		200 50	*Rudels* (1989)	
Halocline Water (HW)	-2	0.5	33.5	35			*Topp and Johnson* (1997)	Arctic Ocean Halocline Water

Table 5: Table of watermass definitions in the literature. Please note that this table does not assume to be complete! Watermasses are sorted by name, if the reference gives an acronym this is also given. Note that some definitions can only be interpreted in context with other watermass boundaries given in the reference. Fp stands for freezing point. The upper and lower bounds for temperature, salinity, density and depth are given, if applicable. Further notes and boundaries can be found in the footnotes at the bottom of this table.

Name	θ	θ	S	S	σ	σ	z	z	Reference	Notes	Region
Iceland Sea Arctic Intermediate Water (ISAIW)	-1.06	-1.06	34.779	34.779					*Jeansson et al.* (2008)	§	
Iceland Sea Arctic Intermediate Water (IAIW)		1		34.676	27.7	30.444 $(\sigma_{0.5})$			*Rudels et al.* (2002, 2005)	include temperature minimum and temperature maximum	Iceland Sea
Iceland Sea Arctic Intermediate Water (IAIW)		0	*		27.7				*Rudels et al.* (2002)		formed locally
Iceland Sea Arctic Intermediate Water (IAIW)		0			27.97	30.444 $(\sigma_{0.5})$			*Rudels et al.* (2002)	slope in T-S diagram negative and increasing	advected from Greenland Sea and Arctic ocean
Iceland Sea Arctic Intermediate Water (IAIW)		0			27.7				*Rudels et al.* (2005)	include temperature minimum and temperature maximum	Iceland Sea
Iceland Sea Arctic Intermediate Water (IAIW)	0.232	0.232		34.676					*Rudels et al.* (2005)	include temperature minimum and temperature maximum	Iceland Sea
Iceland Sea Arctic Intermediate Water (IAIW)		0			27.97	30.444 $(\sigma_{0.5})$			*Rudels et al.* (2005)	advected from the EGC and the Norwegian Sea	
Intermediate Water (IW)		0					1400	500	*de Steur et al.* (2014)	adapted from *Rudels et al.* (2008)	
Intermediate Water (IW)				34.9	≈28.0				*Mauritzen* (1996)	oxygen maximum	
Intermediate Water (IW)		0			27.97	30.444 $(\sigma_{0.5})$			*Rudels et al.* (2008); *Marnela et al.* (2013)	in *Marnela et al.* (2016, 2008) equivalent Nordic Seas: Arctic Intermediate Water (AIW, upper AIW S and θ decrease with depth, lower AIW S and θ decrease with depth; Arctic Ocean: upper Polar Deep Water (uPDW), S increasing, θ decreasing with depth	

Table 5: Table of watermass definitions in the literature. Please note that this table does not assume to be complete! Watermasses are sorted by name, if the reference gives an acronym this is also given. Note that some definitions can only be interpreted in context with other watermass boundaries given in the reference. Fp stands for freezing point. The upper and lower bounds for temperature, salinity, density and depth are given, if applicable. Further notes and boundaries can be found in the footnotes at the bottom of this table.

Name	T low	T high	S low	S high	Reference	Note	Note
Irminger Sea Water (ISW)	6.66	6.66	35.099	35.099	*Jeansson et al.* (2008)	§	
Irminger Sea Water (ISW)	4	5	35	35	*Sutherland and Pickart* (2008)	offshore of EGC/IC system	product of mixing between EGC and IC
Irminger Water (IW)	2.5		34.78		*Harden et al.* (2016)		subtropical origin
Knee Water (KW)		fp	33		*Budéus and Schneider* (1995)	KW around 34 PSU and at freezing point	
Knee Water (KW)	fp			≈34	*Budéus et al.* (1997); *Topp and Johnson* (1997)		
low salinity Water				34	*Cottier and Venables* (2007)	at the Arctic Front west of Spitsbergen	West Spitsbergen glacial melt and precipitation
Lower Arctic Intermediate Water (LAIW)		3	34.9		*Gascard et al.* (1995)	following *Swift and Aagaard* (1981) and *Aagaard et al.* (1987) nomenclature	
lower Arctic Intermediate Water (lAIW)	0	2	34.9	35	*Mauritzen* (1996)		
lower Arctic Intermediate Water (lAIW)	0	3	34.9		*Swift and Aagaard* (1981)		cooling and sinking of AW in the northern Greenland sea
Lower Halocline		0		34	*Rudels et al.* (2015)	study area in Arctic Ocean	
lower West Spitsbergen Water (lWSW)	-0.04	-0.04	34.922	34.922	*Jeansson et al.* (2008)	§	

Table 5: Table of watermass definitions in the literature. Please note that this table does not assume to be complete! Watermasses are sorted by name, if the reference gives an acronym this is also given. Note that some definitions can only be interpreted in context with other watermass boundaries given in the reference. Fp stands for freezing point. The upper and lower bounds for temperature, salinity, density and depth are given, if applicable. Further notes and boundaries can be found in the footnotes at the bottom of this table.

Watermass	T low	T high	S low	S high	density		depth	Reference	Notes
Modified Atlantic Water (MAW)	0	1	34.4	34.91				*Rudels and Quadfasel (1991); Schlichtholz and Houssais (1999b)*	
Modified Atlantic Water (MAW)	0							*Schauer et al. (2004)*	west of 3°E
Modified Atlantic Water (MAW)	0	1	34.4	34.91	‖h		293± 117	*Schlichtholz and Houssais (2002)*	
Modified Knee Water (MKW)	-1.5	0	33	34.5				*Topp and Johnson (1997)*	
Nordic Seas Deep Water (NDW)	-0.92	-0.92	34.912	34.912				*Jeansson et al. (2008)*	§
Nordic Seas Deep Water (NDW)				34.915	30.444 ($\sigma_{0.5}$)			*Rudels et al. (2002, 2005)*	includes Greenland, Nordic Seas Iceland and Norwegian Sea deep water GSDW, ISDW, NSDW
North Atlantic Water (NAW)	1			34.8				*Aksenov et al. (2010)*	is AW in other papers
North Atlantic Water (NAW)	1		34.8					*Aksenov et al. (2010)*	uses varying definitions for different locations
North Icelandic Winter Water (NIWW)		≈2.5		≈34.88				*Mauritzen (1996)*	
Northeast Atlantic Water	7		35					*Sutherland and Pickart (2008)*	Gulfstream
Northern Arctic Intermediate Water (NAIW)	-0.73	-0.73	34.897	34.897				*Jeansson et al. (2008)*	§
Norwegian Sea Deep Water (NSDW)		0		≈34.92				*Mauritzen (1996)*	
Norwegian Sea Deep Water (NSDW)		-0.4	34.9	34.94				*Swift and Aagaard (1981)*	in Norwegian and Iceland Sea
Pacific Water (PW)	-1.72	-1.72	31.953	31.953				*Jeansson et al. (2008)*	§
Polar Intermediate Water (PIW)	-1.8	-1			34.3	34.7		*Aksenov et al. (2010)*	Arctic Ocean and Barents Sea

Table 5: Table of watermass definitions in the literature. Please note that this table does not assume to be complete! Watermasses are sorted by name, if the reference gives an acronym this is also given. Note that some definitions can only be interpreted in context with other watermass boundaries given in the reference. Fp stands for freezing point. The upper and lower bounds for temperature, salinity, density and depth are given, if applicable. Further notes and boundaries can be found in the footnotes at the bottom of this table.

Watermass								Reference	Notes
Polar Intermediate Water (PIW)	-0.71	-0.71	34.531[1]	34.531[1]				*Jeansson et al. (2008)*	§
Polar Intermediate Water (PIW)		0		*	27.7			*Rudels et al. (2002)*	
Polar Intermediate Water (PIW)		0			27.7			*Rudels et al. (2005); Sutherland and Pickart (2008)*	loose definition, derives possibly from the Arctic Ocean thermocline
Polar Intermediate Water (PIW)		0.232	0.232	34.676				*Rudels et al. (2005)*	loose definition, derives possibly from the Arctic Ocean thermocline
Polar Intermediate Water (PIW)		0		34.4		27.7		*Rudels et al. (2005)*	loose definition, derives possibly from the Arctic Ocean thermocline
Polar Intermediate Water (PIW)		0	34.4	34.7				*Swift and Aagaard (1981)*	distinguished from AIW by geography, no sharp interface between the two watermasses
Polar Mixed Layer (PML)							50	*Rudels (1989)*	
Polar Mixed Layer							†	*Rudels et al. (2015)*	study area in Arctic Ocean
Polar Surface Water (PSW)	-1	3			32	34		*Aksenov et al. (2010)*	Arctic Ocean and Barents Sea
Polar Surface Water (PSW)	-1.7	-1.7	33.9	33.9				*Håvik et al. (2017)*	endmembers in mixing triangle
Polar Surface Water (PSW)	-1.74	-1.74	34.345	34.345				*Jeansson et al. (2008)*	§
Polar Surface Water (PSW)		0				27.7		*Rudels et al. (2002, 2005); Sutherland and Pickart (2008)*	includes the Polar Mixed Layer and the halocline Arctic Ocean
Polar Water (PW)		0		34.5				*Bourke et al. (1987); Aagaard and Coachman (1968)*	

Table 5: Table of watermass definitions in the literature. Please note that this table does not assume to be complete! Watermasses are sorted by name, if the reference gives an acronym this is also given. Note that some definitions can only be interpreted in context with other watermass boundaries given in the reference. Fp stands for freezing point. The upper and lower bounds for temperature, salinity, density and depth are given, if applicable. Further notes and boundaries can be found in the footnotes at the bottom of this table.

Name	T	T	Salinity	Density	Depth	Reference	Note	Region
Polar Water (PW)		0	33			Budéus and Schneider (1995)		
Polar Water (PW)			33			Budéus et al. (1997)		
Polar Water (PW)		0			500	de Steur et al. (2014)	adapted from Rudels et al. (2008)	
Polar Water (PW)		0			400	Foldvik et al. (1988)	after Swift and Aagaard (1981)	
Polar Water (PW)			34.6			Hanzlick (1983)		
Polar Water (PW)			34			Harden et al. (2014)		
Polar Water (PW)			34.5	27.8		Mauritzen (1996)	high oxygen levels	
Polar Water (PW)			34.4			Rudels and Quadfasel (1991); Manley (1995)		
Polar Water (PW)		0				Schauer et al. (2004)	west of 3°E	
Polar Water (PW)		0	34.7			Schlichtholz and Houssais (1999b)		
Polar Water (PW)	0		34.4			Schlichtholz and Houssais (1999b)		
Polar Water (PW)		0	34.7 [‖i]		65± 42	Schlichtholz and Houssais (2002)		
Polar Water (PW)	0		34.7			Schlichtholz and Houssais (2002)		
Polar Water (PW)		0	34.4			Swift and Aagaard (1981); Gascard et al. (1995); Topp and Johnson (1997); Harden et al. (2016); Manley et al. (1992)	following Aagaard et al. (1987) nomenclature, in Swift and Aagaard (1981) can have higher surface temperatures (3-5°C) due to thin and strongly stratified layer	Arctic Ocean
Polar Water (PW)		0	33.9			Topp and Johnson (1997)	after Schneider and Budéus (1995) to allow for KW	

Table 5: Table of watermass definitions in the literature. Please note that this table does not assume to be complete! Watermasses are sorted by name, if the reference gives an acronym this is also given. Note that some definitions can only be interpreted in context with other watermass boundaries given in the reference. Fp stands for freezing point. The upper and lower bounds for temperature, salinity, density and depth are given, if applicable. Further notes and boundaries can be found in the footnotes at the bottom of this table.

Watermass	T up	T low	S up	S low	σ up	σ low	Depth	Reference	Notes
Polar Water, Polar Intermediate Water, Greenland and Norwegian Sea Deep Water		0						*Woodgate et al.* (1999)	
Recirculating Atlantic Water (RAW)	1		34.9					*Budéus et al.* (1997)	
Recirculating Atlantic Water (RAW)	2						500	*de Steur et al.* (2014)	adapted from *Rudels et al.* (2008)
Recirculating Atlantic Water (RAW)	2				27.7	27.97		*Rudels et al.* (2002)	
Recirculating Atlantic Water (RAW)	0				27.97	30.444 ($\sigma_{0.5}$)		*Rudels et al.* (2002)	slope in T-S diagram positive
Re-circulating Atlantic Water (RAW)	3.02	3.02	35.053	35.053				*Jeansson et al.* (2008)	§
Return Atlantic Water (RAW)	0		34.9					*Budéus and Schneider* (1995)	after *Hopkins* (1991)
Return Atlantic Water (RAW)	0		34.9		27.8			*Harden et al.* (2016)	recirculated Norwegian Atlantic Current Water
Return Atlantic Water (RAW)			34.9					*Mauritzen* (1996)	
Return Atlantic Water (RAAW)	0				27.7	30.444 ($\sigma_{0.5}$)		*Rudels et al.* (2005)	warm core of the EGC comprising RAW and AAW
Surface Water (SW)						27.7		*Rudels et al.* (2008); *Marnela et al.* (2013)	in *Marnela et al.* (2016, 2008) equivalent Nordic Seas: Warm Surface Water (wSW); Arctic Ocean: Polar Surface Water (PSW)
Upper Arctic Intermediate Water (uAIW)	0	2	34.7	34.9				*Mauritzen* (1996)	

Table 5: Table of watermass definitions in the literature. Please note that this table does not assume to be complete! Watermasses are sorted by name, if the reference gives an acronym this is also given. Note that some definitions can only be interpreted in context with other watermass boundaries given in the reference. Fp stands for freezing point. The upper and lower bounds for temperature, salinity, density and depth are given, if applicable. Further notes and boundaries can be found in the footnotes at the bottom of this table.

Watermass	θ min	θ max	S min	S max	σ min	σ max	depth lower	depth upper	Reference	Note	Area
Upper Arctic Intermediate Water (UAIW)		2	34.7	34.9					*Swift and Aagaard* (1981); *Gascard et al.* (1995)	following *Aagaard et al.* (1987) nomenclature	
Upper Halocline				34			below the upper temperature minimum		*Rudels et al.* (2015)	study area in Arctic Ocean	
upper Polar Deep Water (uPDW)	-0.35	-0.35	34.907	34.907					*Jeansson et al.* (2008)	§	
upper Polar Deep Water (uPDW)		0			27.97	30.444 ($\sigma_{0.5}$)			*Rudels et al.* (2002, 2005)	S increasing and θ decreasing with depth	Arctic Ocean
upper Polar Deep Water		0					1000 db	below AW II	*Rudels et al.* (2015)	study area in Arctic Ocean	
upper Polar Deep Water (UPDW)	-0.5	0	34.7	34.9					*Schlichtholz and Houssais* (1999b)	only if the mean θ − S regression slope is negative	
upper Polar Deep Water (UPDW)	-0.5	0	34.7	34.9	‖j		1008± 172		*Schlichtholz and Houssais* (2002)	only if the mean θ–S regression slope is negative	
warm Atlantic Water (AWw)	2		34.91						*Schlichtholz and Houssais* (1999b)		
warm Atlantic Water (wAW)	2		34.91		‖k		169± 87		*Schlichtholz and Houssais* (2002)		
Warm Deep Water (WDW)	-0.5	0	34.8						*Rudels and Quadfasel* (1991)		
warm Norwegian Sea Deep Water (NSDWw)	-0.5	0	34.9	34.92					*Schlichtholz and Houssais* (1999b, 2002)	if not AIW or UPDW	
warm Norwegian Sea Deep Water (NSDWw)	-0.8	-0.5	34.9	34.92					*Schlichtholz and Houssais* (1999b)	if not AIW	
warm Norwegian Sea Deep Water (NSDWw)	-0.8	-0.5	34.9	34.92	‖l		947± 161		*Schlichtholz and Houssais* (2002)	if not AIW	

Table 5: Table of watermass definitions in the literature. Please note that this table does not assume to be complete! Watermasses are sorted by name, if the reference gives an acronym this is also given. Note that some definitions can only be interpreted in context with other watermass boundaries given in the reference. Fp stands for freezing point. The upper and lower bounds for temperature, salinity, density and depth are given, if applicable. Further notes and boundaries can be found in the footnotes at the bottom of this table.

Watermass	T	T	S	S	density	Reference	Reference	Notes
warm Polar Surface Water (PSWw)	0				27.7	*Rudels et al. (2002, 2005); Sutherland and Pickart (2008)*		warmed and freshened PSW, air-sea interactions, ice-melt, sea-ice melting on warmer AW
Water Mass I		0		34.7		*Rudels (1987)*	*Swift and Aagaard (1981)*	
Water Mass II	0			34.5		*Rudels (1987)*	*Swift and Aagaard (1981)*	
Water Mass IIa	0	1	34.5	34.7		*Rudels (1987)*	*Swift and Aagaard (1981)*	
Water Mass IIa	1		34.5	34.9		*Rudels (1987)*	*Swift and Aagaard (1981)*	
Water Mass III		0	34.7			*Rudels (1987)*	*Swift and Aagaard (1981)*	
Water Mass IV	0	1	34.7			*Rudels (1987)*	*Swift and Aagaard (1981)*	
Water Mass V	1	3	34.9			*Rudels (1987)*	*Swift and Aagaard (1981)*	
Water Mass VI	3		34.9			*Rudels (1987)*	*Swift and Aagaard (1981)*	

* $34.676+0.232*\theta$

† above the (upper) temperature maximum

‡ below the temperature maximum

§ also uses O_2, PO_4, NO_3, SiO_2, CFC-11, CFC-12, SF6, A_T, C_T and pH

‖a mean density: $\sigma=28.06$, $\sigma_1=32.79$, $\sigma_3=41.95$

‖b mean density: $\sigma=28.08$, $\sigma_1=32.81$, $\sigma_3=41.97$

‖c mean density: $\sigma=28.02$, $\sigma_1=32.70$, $\sigma_3=41.77$

‖d mean density: $\sigma=28.08$, $\sigma_1=32.82$, $\sigma_3=42.00$

‖e mean density: $\sigma=28.09$, $\sigma_1=32.83$, $\sigma_3=42.01$

‖f mean density: $\sigma=27.22$, $\sigma_1=32.42$, $\sigma_3=41.43$

‖g mean density: $\sigma=28.08$, $\sigma_1=32.83$, $\sigma_3=42.02$

‖h mean density: $\sigma=27.94$, $\sigma_1=32.64$, $\sigma_3=41.74$

‖i mean density: $\sigma=26.81$, $\sigma_1=31.55$, $\sigma_3=40.74$

‖j mean density: $\sigma=28.05$, $\sigma_1=32.77$, $\sigma_3=41.91$

‖k mean density: $\sigma=27.91$, $\sigma_1=32.55$, $\sigma_3=41.53$

‖l mean density: $\sigma=28.06$, $\sigma_1=32.79$, $\sigma_3=41.94$

\# 500 m thick

Maren Richter
Name

Declaration acc. to § 10 Paragraph 11 Common Part of the Master Examination Regulations

I hereby declare that I wrote my Master Thesis independently and that I did not use other sources and auxiliary means than the ones indicated.

This Master Thesis is not submitted in another examining procedure.

I further declare that the Master thesis **might be** / ~~might not be~~* made available to the public in this version.

*Please mark where applicable

Place/Date: *Bremen, 14.08.2017*

Signature: *M. Richter*